APPLICATION OF PETROPHYSICAL AND GEOPHYSICAL ANALYSIS IN IMPROVEMENT OF COMPLETIONS DESIGN IN ORGANIC-RICH MUDROCKS

A Dissertation

by

ADERONKE ABIODUN ADERIBIGBE

Submitted to the Office of Graduate and Professional Studies of
Texas A&M University
in partial fulfillment of the requirements for the degree of

DOCTOR OF PHILOSOPHY

Chair of Committee,	Zoya Heidari
Committee Members,	John Killough
	Robert H. Lane
	Yuefeng Sun
Head of Department,	A. Daniel Hill

May 2016

Major Subject: Petroleum Engineering

ABSTRACT

In hydraulic fracturing stimulation treatments for organic-rich mudrocks, some issues that pose challenges in pre-completions design include selection of intervals for stimulation treatment, and selection of proppants for stimulation design. After the stimulation treatment, a key post-completions issue is the detection of the fracture and evaluation of the fracture performance. The application of petrophysical and geophysical analysis can offer potential solutions to these issues, thereby lead to improvements of both pre-completions and post-completions design of the hydraulic fracturing treatment.

The objectives of this dissertation are (a) to introduce a rock classification workflow, which integrates geologic, petrophysical and geomechanical analysis, for the determination of zones for fracture stimulation treatments, (b) to develop a new technique for characterization of mechanical damage in proppant packs to improve the selection of proppants for stimulation treatment, and (c) to investigate the use of nanoparticles as contrast agents that enhances magnetic susceptibility measurements for the detection of hydraulic fractures after stimulation treatments.

I first demonstrated that the integrated rock classification workflow, which includes geologic attributes of the formation, in-situ stress assessment capturing the effects of anisotropy in organic-rich mudrocks, and also takes into account anisotropic poroelastic coefficients, can improve the selection strategy for completion zones. Next, I introduced the application of the Hertz-Mindlin granular contact model to approximate the effective elastic properties of proppant packs. I used the calibration parameters of the Hertz-Mindlin

model to develop correlations for the prediction of weight percentage of crushed proppants. Finally, from laboratory investigations, I demonstrated that superparamagnetic nanoparticles when mixed with proppants enhance the reliability of detecting fractures using magnetic susceptibility measurements. I also presented the sensitivity of the magnetic susceptibility measurements to the composition of proppants, concentration of nanoparticles, and the width of the induced fractures.

The outcomes of this dissertation demonstrate significant contribution of petrophysical and geophysical analysis in achieving better fracture performance from completions design. Better fracture performance can be achieved by improving the strategies for identifying prolific zones for fracture initiation and propagation, achieving good fracture conductivity from the selection of proppants, and analyzing post-fracture performance of hydraulic fracturing treatments. These improvements could in turn result in improved rates and recoveries from organic-rich mudrock formations.

DEDICATION

This work is dedicated to our little one- Jesulayomi. The excitement of feeling your kicks while preparing this dissertation filled my heart with love and warmth. The joy of preparing for your arrival was a great motivation to finish well and strong. Now you are here, your coos and smiles simply light up our world!

ACKNOWLEDGEMENTS

My sincere gratitude goes to my supervisor and chair of my dissertation committee, Dr. Zoya Heidari, and to members of my dissertation committee- Dr. Killough, Dr. Lane, and Dr. Sun, for their valuable and insightful contributions to my research. My special appreciation to Dr. Heidari for her outstanding support and belief in my capabilities to achieve each milestone throughout my PhD program. Through her admirable passion and excellent mentorship, I have developed knowledge and skills in the field of formation evaluation, and also accrued life-lessons in the areas of discipline and leadership. My special thanks to Dr. Lane, who had previously served as the chair of my master's thesis committee. His unflinching support through my navigation at Texas A&M, through making professional decisions, and sharing personal joys will always be cherished. I also thank Dr. Hiroko Kitajima, for her kindness and willingness to provide guidance and help at different times during my coursework with her, as well as my research.

I am grateful for colleagues in the Multi-Scale Formation Evaluation research group. Our team of diverse cultural backgrounds are very knowledgeable, yet create a fun and stress-free atmosphere for work. I particularly appreciate Clotilde Chen Valdes and Kai Cheng, for their collaboration in our research work. I thank Alexander Gia, our technical editorial assistant for her patience and contributions. I also thank the associate editors and the anonymous reviewers of the Interpretation journal, Journal of Petroleum Science and Engineering, and SPE Production and Operations journal, for their technical and editorial feedback on my papers.

I appreciate staff of the petroleum engineering department- John Maldonado for his valuable role in my experimental work, John Winkler and Eleanor Schuler, for their availability to answer questions and provide guidance throughout the course of my program. I acknowledge the Texas A&M University Integrated Ocean Drilling Program (IODP) laboratory, David Houpt and his group, for technical support and use of their facility for the magnetic susceptibility measurements. My gratitude also goes to the Microstructural Engineering of Structural and Active Materials laboratory at the materials and science engineering department, the X-ray Diffraction laboratory at the chemistry department, and the Microscopy and Imaging center at Texas A&M University for providing the facilities and for their technical contribution for the characterization of nanoparticles.

My summer internship at BP America, Inc. with the L48 North America Gas (NAG) group was my debut in the field of geomechanics and completion petrophysics. I appreciate my supervisor Chris Morton for challenging me with the task of my project. I appreciate the team members, and particularly my buddy– Yashwanth Chitrala, for the times spent researching and trouble-shooting to ensure the successful completion of my summer project.

The work reported in this dissertation was supported by Saint-Gobain Proppants, Texas A&M University's Joint Industry Research Program on Multi-Scale Formation Evaluation of Unconventional and Carbonate Reservoirs, and the Crisman Institute of Petroleum Research at the Harold Vance Department of Petroleum Engineering. My special gratitude goes to Saint-Gobain Proppants for providing proppant samples, and for

the open channels for communication, discussions and collaboration. I am also grateful to the Society of Petrophysicists and Well Log Analysts (SPWLA) foundation, for awarding me the Vikings memorial scholarship, which was helpful for my living and studying expenses at Texas A&M.

I appreciate my friends for their prayers and for cheering me on. My inspiration for the successful completion of PhD program has been the love and support from my parents and parents-in-law– Sunday and Victoria Aderibigbe, and Olatunji and Margaret Olutola, my minister– Oladapo Orelaja, my siblings– the Olaniyans, Aderibigbes, Ayoolas, and my siblings-in-law– the Olopades, Oresusis, Olutolas, Braithwaites and the Dadas. Finally, I thank my husband, friend and greatest fan- Olayiwola, for his kindness, understanding and affection.

To the Lord Jesus Christ, the fountain of all wisdom, author and finisher of my faith, be all the glory and honor forevermore. Amen.

NOMENCLATURE

a_1, a_2, a_3, a_4	Correlation fitting parameters
a_n	Radius of contact area
b_1, b_2, b_3, b_4	Correlation fitting parameters
C	Coordination number
C_{IJ}^{dry}	Dry stiffness coefficients of compliance tensor
C_{IJ}^{sat}	Saturated stiffness coefficients of compliance tensor
C_{IJ}^{VTI}	Stiffness tensor in a VTI medium
C_{ijkl}	Stiffness tensor
C_n	Concentration of nanoparticle solution
d	core diameter, cm
Di	loop sensor diameter, cm
f_i	Volume fraction of the *ith* mineral component
f_t	Fraction of grain contacts having no slip
F_n	Normal contact force
F_t	Tangential contact force
G_s	Specific gravity of proppant grains
h_{prop}	Height of proppant pack
k_1,k_2,k_3	Core-calibrated correction parameters
k_d	Dynamic bulk modulus

K	Bulk modulus of proppant grain material
K_{fl}	Bulk modulus of the fluid mixture
K_{HM}	Effective bulk modulus of identical-sphere packing
K^{HS+}	Upper HSW bounds on the bulk modulus
K^{HS-}	Lower HSW bounds on the bulk modulus
K_{iso}^{sat}	Apparent isotropic bulk modulus of the saturated rock
K_{fi}	Bulk modulus of the *i*th component of the fluid phase
K_m	Grain bulk modulus of the rock
K_{max}	Maximum shear modulus of the constituent components
K_{min}	Minimum shear modulus of the constituent components
M_i	Elastic modulus of the *i-th* mineral component
M_p	Mass of proppants
M_V	Voigt upper bound of the effective elastic modulus
M_{VRH}	Arithmetic average of the Voigt upper bound and Reuss lower bound
M_R	Reuss lower bound of the effective elastic modulus
n	Total number of available measured/estimated points
n_f	Number of fluid phase components
N	Total number of rock/mineral components
P	Effective pressure applied to the spheres
P_p	Pore pressure
R	Sphere radius

S_i	Fluid saturation of the *i*th component of the fluid phase
S_n	Normal stiffness
S_t	Tangential stiffness
x_i	Volumetric concentration of rock component
x_{core}	Core measurements
x_{est}	Well-log-based estimates
V_f	Drilling fluid velocity
V_{ij}	Wave velocity wave with propagation in the *i* direction, and polarization in the *j* direction
V_p	Compressional wave velocity
$V_p(0^o)$	Compressional -wave velocity parallel to the bedding
$V_p(45^o)$	Compressional -wave velocity at 45^o with respect to the bedding
$V_p(90^o)$	Compressional -wave velocity normal to the bedding
V_s	Shear wave velocity
$V_s(0^o)$	Shear-wave velocity parallel to the bedding
$V_s(90^o)$	Shear-wave velocity normal to the bedding
V_T	Stoneley-wave velocity
W_c	Weight percentage of crushed proppant
w_f	Width of hydraulic fracture
α_h	Biot's coefficient of effective stress in the horizontal direction
α_v	Biot's coefficient of effective stress in the vertical direction

γ	Thomsen shear anisotropy parameter
δ	Thomsen anisotropy parameter
δ_n	Normal displacement
$\Delta\kappa$	Change in volume magnetic susceptibility
Δt_p	Travel time of the compressional wave
Δt_s	Travel time of the shear wave
ε	Thomsen compressional anisotropy parameter
ε_h	Minimum horizontal strain
ε_{ij}	Strain tensor
ε_v	Maximum horizontal strain
κ	Volume specific magnetic susceptibilities
κ_{rel}	Relative response
κ_{uncor}	Uncorrected volume specific magnetic susceptibilities, dimensionless
μ	Shear modulus of proppant grain material
μ_d	Dynamic shear modulus
μ_i	Shear modulus of rock component
μ_{HM}	Effective shear modulus of identical-sphere packing
μ^{HS+}	Upper HSW bounds on the shear modulus
μ^{HS-}	Lower HSW bounds on the shear modulus
μ_{max}	Maximum shear modulus of the constituent components

μ_{min}	Minimum shear modulus of the constituent components
ν	Poisson's ratio of grain material
ν_{hor}	Horizontal Poisson's ratio
ν_{ver}	Vertical Poisson's ratio
ρ	Bulk density
ρ_f	Drilling fluid density
σ_h	Minimum horizontal stress
σ_{ij}	Stress tensor
σ_v	Overburden stress
τ_n	Tangential displacement
ϕ	Porosity of spheres pack
χ	Mass normalized susceptibility

ACRONYMS

AEC	Advanced Energy Consortium
ANN	Artificial Neural Network
API	American Petroleum Institute
CNT	Compensated Neutron Tool
CQ	Completion Quality
CSEM	Controlled Source Electromagnetic
ECS	Elemental Capture Spectroscopy
GPB	Great Permian Basin
HC	Hierarchical Clustering
HM	Hertz-Mindlin
HSW	Hashin-Shtrikman-Walpole
HTNCC	High Thermal Neutron Capture Compound
ISO	International Organization for Standardization
IP	Intermediate Density Proppants
LVDT	Linear Variable Displacement Transformer
MRI	Magnetic Resonance Imaging

MS	Magnetic Susceptibility
NMR	Nuclear Magnetic Resonance
PEF	Photoelectric Factor
RMSE	Root Mean Square Error
RQ	Reservoir Quality
SP	Stress Profile
SQUID	Superconducting Quantum Interference Device
TEM	Transmission Electron Microscope
TOC	Total Organic Content
XRD	X-Ray Diffraction
VTI	Vertical Transverse Isotropy
VRH	Voigt-Reuss-Hill
VSP	Vertical Seismic Profiling

TABLE OF CONTENTS

LIST OF FIGURES

Page

LIST OF TABLES

Page

CHAPTER I

INTRODUCTION

This dissertation introduces new methods that apply petrophysical and geophysical analysis for the improvement of completions design for hydraulic fracturing stimulation treatments in organic-rich mudrocks. First, this dissertation introduces an integrated rock classification and workflow which incorporates anisotropic stress gradient, petrophysical and geological evaluation, for the selection of completions zones in organic-rich mudrocks. Second, this dissertation investigates and develops a new technique using geophysical analysis of acoustic measurements for the characterization of mechanical damage in proppants selected for completions design for organic-rich mudrocks. Finally this dissertation investigates a new technique in which geophysical analysis of magnetic susceptibility measurements is applied for the enhanced detection and location of hydraulic fractures in organic-rich mudrocks.

1.1 Background

Organic-rich mudrocks are characterized by complex mineralogy, heterogeneity and low permeability. Hence, safe and economic recovery from these formations depend on effective completions design. Completions generally play a vital role in field development because they represent the interface between the subsurface i.e., reservoir, and the surface production. Completions design cuts across many fields such as engineering, geology, petrophysics, hydraulics, chemistry and material science. The

decisions required in completions design vary depending on the type of completion. Examples of the types of completions for a well include well tubing design, perforation technique, stimulation treatment (i.e., acidizing and hydraulic fracturing), artificial lift system, and sand control system (Bellarby, 2009). This dissertation focuses on new techniques that apply petrophysical and geophysical analysis for the improvement of completions design for hydraulic fracturing stimulation treatments.

A successful hydraulic fracturing stimulation treatment requires strategic planning for both the pre-completions and post-completions stages. One major challenge in pre-completions design stage is the determination of zones for fracture placement. It is very pertinent to identify zones that would support fracture initiation and growth, as well as zones that could serve as fracture barriers. Another challenge in pre-completions design stage is the selection of proppants. A poor proppant selection procedure leads to inefficiencies in the creation of the conductive pathways for production from the reservoir. In the post-completions stage, the evaluation of the hydraulic fracture location and geometry is also challenging. Having a good understanding of the location and geometry of the fractures generated by the treatment, can assist in the assessment of fracture performance and recovery from the fractured wells.

1.2 Literature Review

1.2.1 Hydraulic fracturing

Hydraulic fracturing is a well stimulation treatment in which a proppant-loaded fluid is pumped at a sufficiently high pressure to create fractures in a formation. This

treatment stimulates the flow of oil or gas within the formation into the well. The use of the hydraulic fracturing technology, alongside with horizontal drilling, has accelerated the economically viable development of low permeability formations such as organic-rich mudrocks.

The main component materials for hydraulic fracturing treatments are fracturing fluids and proppants. Since the inception of the hydraulic fracturing technology in the 1940s where gelled gasoline mixed with sand was used for the stimulation treatment, different types of fracturing fluids have evolved over the years (Rae and Di Lullo, 1996). The choice of fracturing fluid depends on factors such as reservoir properties and conditions, costs of treatment and environmental regulations. Some examples of fracturing fluids include cross-linked gel, hybrid, micellar, foam, and slickwater. Proppants, the other main component in fracturing treatments, also exist in different forms, shapes and sizes. The choice of proppants depends on factors such as reservoir temperature and pressure, as well as the type of reservoir fluids- gas, oil and water (fresh and salt). Advancements in the hydraulic fracturing technology can be achieved through petrophysical and geophysical analysis for determination of optimal locations for the fracture treatment, selection of proppant-fluid combinations, and also determination of location of hydraulic fractures.

1.2.2 Petrophysical and geophysical analysis

Petrophysical analysis is an integral part of reservoir characterization which integrates well log data with core data, to determine petrophysical properties of the rock

and their interaction with fluids. Some key petrophysical properties of the rock include lithology, net pay, porosity, fluid saturations and pressures, density and permeability. Recent interest in the development of organic-rich mudrocks have also led to the development of petrophysical and geomechanical analysis techniques for the determination of organic richness, and rock mechanical properties of such formations.

Petrophysical and rock physics properties of the formation can be obtained from joint interpretation of well log data from borehole measurements such as natural gamma, neutron, density, resistivity, compressional- and shear-wave velocities, and elemental capture spectroscopy (ECS). In this dissertation, I focus on the application of petrophysical and geomechanical analysis in the pre-completions design of hydraulic fracture treatments. The aspects of pre-completions design considered in this work are the determination of target locations for the fracture treatment, and the selection of proppants for hydraulic fracture treatments.

Geophysical analysis is also an important part of the study of the subsurface. The three main methods used in geophysical analysis are magnetic, gravity and seismic methods. Magnetic methods are used in the measurements of properties such as magnetic susceptibility and remanence. Other magnetic methods such as electromagnetic measurements can also be used in obtaining properties such as electrical resistivity and inductance. Gravity methods are used in the measurement of density, while seismic methods are used in the measurement of seismic velocity, as well as density (Hallenburg, 1998). In this dissertation, I focus on the application of the magnetic susceptibility

measurements in the post-completion assessment stage of detection of location and geometry of hydraulic fractures.

1.2.3 Pre-completions design: Selection of completion zones for hydraulic fracturing treatment

There are several variables that can be considered in selection of candidate zones for hydraulic fracturing treatments. Some of these variables include hydrocarbon-in-place, petrophysical properties of the formation such as the porosity and permeability, mineralogy, maturity of kerogen sources, presence of natural fractures, geologic features, in-situ stresses and anisotropy (King, 2010). Some of these variables can be combined using methods such as rock classifications, in order to define the completions selection criteria. The selected criteria might not have a fit-for-all purpose because of the high variability of organic-rich mudrock formations, however, the concepts of selection criteria can be adapted for each formation.

Rock classifications are carried out for reservoir characterization, and selection of intervals for hydraulic fracturing treatment. Previous studies on rock classifications in organic-rich mudrock formations focused primarily on petrophysical and formation properties such as porosity, Total Organic Content (TOC) and mineralogy (Kale et al., 2010; Gupta et al., 2012). The geometry of hydraulic fractures generated in organic-rich mudrocks is largely affected by geomechanical properties- elastic moduli and in-situ stresses. The elastic properties of rocks are influenced by factors such as rock composition, pore and overburden pressures (Montaut et al., 2013). Hence, the inclusion of the elastic

properties can improve rock classification for selection of candidate zones for hydraulic fracturing (Gupta et al., 2012; Saneifar et al. 2014).

Asides elastic properties, in-situ stresses are the most significant factors controlling hydraulic fracturing (Warpinski and Smith, 1989). Several studies have shown that organic-rich mudrocks exhibit anisotropy due to partial alignment of plate-like clay minerals, as well as the presence of laminations of organic material (Sayers 2005, 2013). The application of isotropy models in the assessment of in-situ stresses in organic-rich mudrocks therefore results in inaccurate stress gradients (Higgins et al., 2008). Hence, anisotropic models such as the vertical transverse isotropy (VTI) are applied for reliable assessment of anisotropic elastic properties and stress gradient, which affect fracture performance. The incorporation of in-situ stress gradients, that uses appropriate anisotropy models, can further improve rock classification for identification of zones for fracture initiation and containment in organic-rich mudrocks (Malik et al., 2013; Saneifar et al., 2014).

1.2.4 Pre-completions design: Selection of proppants for hydraulic fracturing design

Proppants are injected along with fracturing fluids during hydraulic fracturing treatments to create conductivity for the initiated fractures. These proppants make up a significant component of the cost of fracture stimulation treatment, hence, strategic selection of proppants is a critical element in completions design. There are different types of proppant available in the oil and gas industry. These proppants include uncoated sands, resin-coated sands, ceramics, and lightweight proppants such as walnut shells, pits, and

husks (Liang et al., 2015). The performance of proppants can be affected by proppant failure or fines migration, which can be caused by mechanical damage or diagenesis under downhole conditions. Crush tests are used in evaluating the mechanical properties and crush resistance of proppants used in hydraulic fracturing operations. The original guidelines for procedures and equipment used in these tests were provided by the American Petroleum Institute (API) standardized crush-testing procedure (API RP-56, 1983). The guidelines have been revised to the API RP-19C procedure, with specific testing procedures for evaluating proppants used in hydraulic fracturing and gravel-packing operations (API RP-19C, 2008). Several authors have addressed some deficiencies and shortcomings of the crush test procedures (Palisch et al., 2010; Getty and Bulau, 2014; Liang et al., 2015). The deficiencies and shortcomings highlighted by these studies point to the need for development of improved techniques to investigate mechanical damage in proppants.

Several studies on mechanical damage that leads to compaction and crushing in sands have been carried out using ultrasonic measurements during uniaxial compaction tests (Fortin et al., 2007; Fawad et al., 2011). Some additional studies for unconsolidated sands, have combined the analysis of ultrasonic measurements with the application of effective medium theory. Effective medium theory for granular media such as the Hertz-Mindlin model (Mindlin, 1949), can be used to investigate mechanical damage in unconsolidated sands (Avseth and Bachrach, 2005; Dutta et al., 2010; Zimmer, 2003). The concepts from studies on unconsolidated sands can be adapted to proppant, by application of the Hertz-Mindlin model in characterization of mechanical damage in proppant packs.

1.2.5 Post-completions design: Detection of location and geometry of fractures

In the hydraulic fracturing stimulation process, the success of a fracture treatment is measured by the creation of fracture geometries that are as close as possible to the model design geometry in the target zone. It is therefore necessary to have a good understanding of the location and geometry of the fractures generated by the treatment.

Methods for evaluating fracture treatment using borehole measurements are well documented. Agnew (1966) introduced the use of temperature surveys as a diagnostic tool for evaluating fracture treatment. This technique involves running temperature transverse by using conductor line resistance wire-type temperature logging systems in the wellbore after completing the fracture treatment to get the temperature profile. The temperature decay rate can be calculated and the differences in decay rates used to identify fractured zones (Agnew, 1966). Since this method measures fluid properties, it does not provide insight on the propped fracture, which is more relevant for determining effective fracture geometry. Wright et al. (1998) introduced downhole tiltmeter fracture mapping to measure hydraulic fracture growth. The wireline-conveyed tiltmeter measures fracture-induced rock deformation in nearby offset wells in relation to time and depth, and inverts the data to determine the hydraulic fracture geometry. The challenge with using this method is that its resolution depends on the location of the offset well, which makes it difficult to make continuous measurements of the fracture-induced tilt at different times and depths (Wright et al., 1998).

There are other existing methods for detection of the location and geometry of hydraulic fractures which involve the use of nuclear methods. Gamma ray spectroscopy

measurements can be used to detect fracturing fluid and proppants tagged with radioactive tracers to give an indication of the propped fracture height (Gadekea et al., 1991). McDaniel et al. (2009) introduced the use of resin-coated proppant incorporated with a taggant that becomes radioactive when irradiated by a natural gamma ray detectors. More recently, proppants tagged with high thermal neutron capture compound (HTNCC) have also been employed to detect fracture height using compensated neutron tool (CNT) or pulsed neutron capture (PNC) tool (Saldungaray et al., 2012).

There are, however, environmental and regulatory concerns about existing techniques which use radioactive tracers for the detection of fracture location or geometry. Recent research studies in the petroleum industry have been investigating the development of nanoparticles as contrast agents for reservoir characterization and advanced reservoir surveillance. The concept of this application is adapted from biomedical applications, where nanoparticles are used for targeted drug delivery, and enhanced biomedical imaging (Yu et al., 2010; Golestanian et al., 2007). Nanoparticles can be synthesized to exhibit unique electric, magnetic, chemical and optical properties (Yu, J. et al., 2010). In particular, nanoparticles with superparamagnetic properties can be synthesized and applied as contrast agents mixed with proppants that can enhance borehole geophysical measurements, such as magnetic susceptibility.

Magnetic susceptibility is the degree of magnetization of materials in relation to an applied magnetic field (Dearing, 1994). Hence, it is defined as the ratio of induced magnetization to the inducing magnetization field. Superparamagnetic nanoparticles become magnetized up to their saturation magnetization when a magnetic field is applied.

The superparamagnetic nanoparticles exhibit a strong magnetic response, and hence a high magnetic susceptibility (Wahajuddin and Arora, 2012). Rocks also possess magnetic susceptibility properties depending on the mineralogy and geochemical components of the rock. However, superparamagnetic nanoparticles possess a relatively higher magnetic susceptibility than the natural environment of the rock formation. In hydraulic fracture stimulation treatments, superparamagnetic nanoparticles pumped along with proppants can act as contrast agents that can improve proppant detection, and highlight the fracture location.

1.3 Statement of Problem

A reliable petrophysical evaluation of reservoir can significantly contribute to the challenges identified in the pre-completions and post completions stages. Petrophysical and geomechanical analysis is important in the identification of target zones for hydraulic fracturing stimulation treatment. Petrophysical techniques can also be applied for the characterization of proppant properties necessary for selection of proppants for hydraulic fracturing treatments. The effectiveness of the fracture stimulation treatment for continuous improvement of the reservoir development can also be evaluated from petrophysical and geophysical analysis. In this dissertation, I introduce methods for the application of petrophysical and geophysical analysis in the improvement of pre-completions and post-completions design for hydraulic fracturing stimulation treatments.

In pre-completions design, to address the concern of zone selection for completion purposes, I introduce the application of an integrated rock classification workflow. The

workflow takes into account the analysis of geologic attributes, petrophysical and compositional properties as well as elastic and geomechanical properties to improve the selection of zones for fracture placement. A contribution of the integrated rock classification workflow, compared to the conventional rock classification techniques, is the integration of geological analysis and geomechanical analysis. The geomechanical analysis estimates in-situ stress that captures the anisotropy in organic-rich mudrocks.

Next, I develop a new technique for the characterization of mechanical damage in proppant packs by geophysical analysis of acoustic measurements. In pre-completions design, this technique seeks to address the challenge in selection of proppants that can withstand closure stress in the formation while ensuring the fracturing conductivity. The characterization of mechanical damage in proppant packs can improve design of the propping agents and quantification of proppant performance.

Finally, to address the post-completions challenge of detecting the location of hydraulic fractures after the stimulation treatment, I investigate a new technique in which nanoparticles, when injected with proppants into the fractures, are used as contrast agents to enhance magnetic susceptibility measurements. The enhanced magnetic susceptibility measurements can be used to detect the location of proppant-filled hydraulic fractures after the stimulation treatment. This detection technique can be applied in the field by using borehole geophysical tools such as the magnetic susceptibility tool, for near wellbore detection of the location of fractures.

1.4 Research Objectives

The motivation of this dissertation is to demonstrate the application of petrophysical and geophysical analysis at pre-completions and post-completions stages, for improvement of the design and performance of hydraulic fracturing treatments in organic-rich mudrock formations. In light of the motivation, I define three main objectives for this study. The first and second objectives addresses challenges at the pre-completions stages of hydraulic fracturing treatments such as the selection of zones for completion and selection of the proppants for the hydraulic fracturing treatments. The third objective addresses the challenge of detecting the location of fractures for evaluation of the fracture performance.

The three objectives are defined as follows:

1. Introduce an integrated rock classification workflow for improving completions design in organic-rich mudrock formations. To fulfill this objective, the short term goals are as follows:
    a. To incorporate formation geologic attributes, reservoir quality, and in-situ stress gradient based on anisotropic models.
    b. To make recommendations on zones for fracture propagation and fracture containment for completions designs.
2. Develop a technique for the characterization of mechanical damage in proppant packs. To fulfill this objective, the short term goals are as follows:

a. To conduct experiments to investigate the variation in porosity and the sensitivity of acoustic measurements to both compaction and crushing in proppant packs.
b. To reliably estimate the effective elastic properties of proppant packs, effective medium models.
c. To develop an analytical model for quantifying mechanical damage in proppant packs.

3. Investigate the use of nanoparticles as contrast agents that enhances magnetic susceptibility measurements for the detection of hydraulic fractures after hydraulic fracturing stimulation treatments. To fulfill this objective, the short term goals are as follows:
    a. To design magnetic susceptibility experiments to investigate the sensitivity of magnetic susceptibility measurements to the formation or matrix type, proppant type and composition, nanoparticle concentration, and fracture width.
    b. To quantify detectable change in magnetic susceptibility.
    c. To investigate the possibility of using nanoparticles as contrast agents for enhanced fracture detection.

1.5 Method Overview

This section shows the workflows and description of methods applied to achieve the three objectives of this dissertation.

1.5.1 Workflow for integrated rock classification based on geological evaluation, reservoir quality, and anisotropic stress profile estimated from well logs (Objective No. 1)

Fig. 1.1 summarizes the workflow for the study on integrated rock classification based on anisotropic stress model for improving completions design. In this study, I first carried out well-log-based geologic facies analysis using core-based geologic facies classification and an input of well logs. Next, I conducted interpretation of well logs and core geochemical measurements for petrophysical and compositional analysis to estimate the reservoir quality of the formation. I also analyzed core geomechanical measurements and borehole acoustic data obtained from dipole sonic tools to estimate the five independent elastic constants. These elastic constants are required to define the stiffness matrix for vertical transverse isotropy of the formation. I applied anisotropic stress models to estimate the stress gradient of the formation from the anisotropy elastic properties. Finally, I conducted integrated rock classification by taking into account the geologic facies analysis, reservoir quality based on the well-log-based estimates of petrophysical properties, and the estimated anisotropic stress gradient.

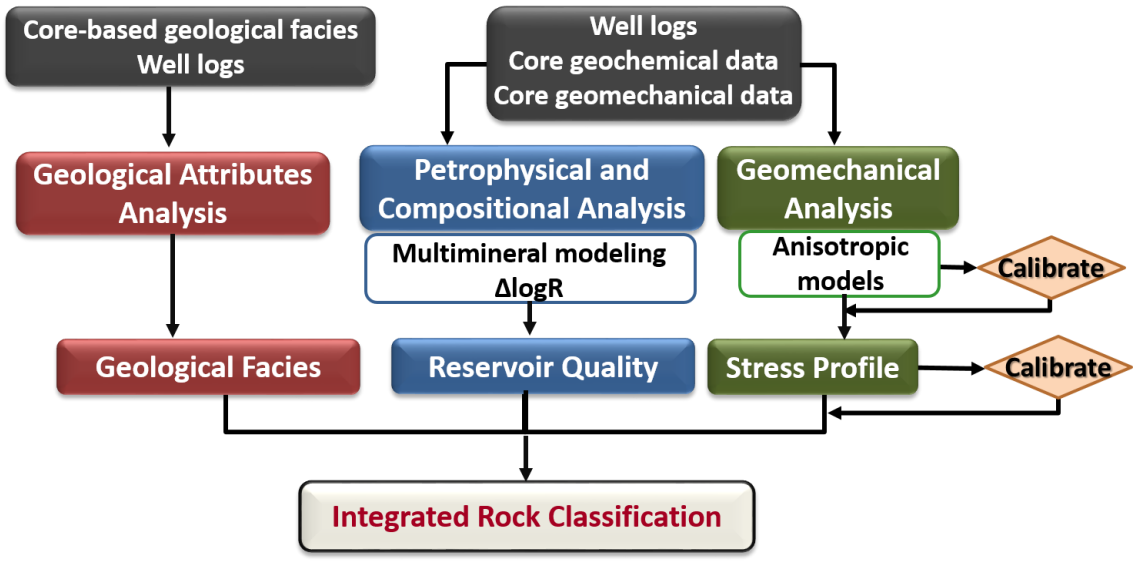

Fig. 1.1—Workflow summary for the study on integrated rock classification based on geological evaluation, reservoir quality, and anisotropic stress profile estimated from well logs.

1.5.2 Workflow for mechanical damage characterization in proppant packs using acoustic measurements (Objective No. 2)

Fig. 1.2 shows the workflow for the study on mechanical damage characterization in proppant packs using acoustic measurements. The workflow includes both experimental and analytical approach. For the experimental approach, I designed and carried out uniaxial compression tests for proppant packs. After unloading the samples from the compression tests, I carried out sieve analysis to measure the crush percentage in the proppant pack. In the analytical method, I applied the Hertz Mindlin model to estimate the effective elastic properties of the proppant pack.

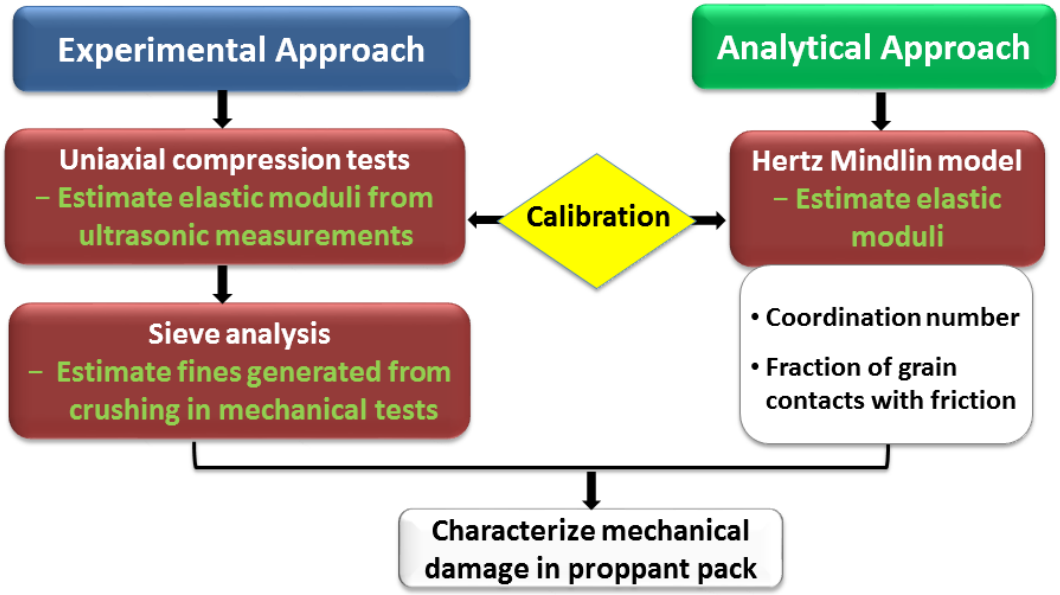

Fig. 1.2—Workflow for the study on mechanical damage characterization in proppant packs using acoustic measurements.

1.5.3 Workflow for application of magnetic nanoparticles mixed with propping agents in enhancing near-wellbore fracture detection (Objective No. 3)

Fig. 1.3 shows the workflow for the study on the detection of propping agents in fractures using magnetic susceptibility measurements enhanced by magnetic nanoparticles. In the laboratory experiments, superparamagnetic nanoparticles were synthesized, and then characterization tests were carried out to determine the size, chemical composition, and magnetic properties of the nanoparticles. The nanoparticle solution was then used for magnetic susceptibility laboratory experiments.

I conducted laboratory experiments using a multisensor core logging instrument which has a core loop sensor for magnetic susceptibility measurements. I designed tests for outcrop samples from the Austin chalk formation and organic-shale rock samples from

the Haynesville formation. I created artificial fractures in the rock samples and filled the fractures with proppants and fluids (i.e., water or different concentrations of nanoparticle solution) being tested. Two types of bauxite-based ceramic intermediate proppants were used in the experiments. I investigated the sensitivity of magnetic susceptibility measurements to (a) type of proppants, (b) the concentration of nanoparticles, (c) width of the induced fracture that is controlled by volume of proppants and nanoparticle solution, for both cores from the Austin chalk formation and organic-shale rock samples from the Haynesville formation.

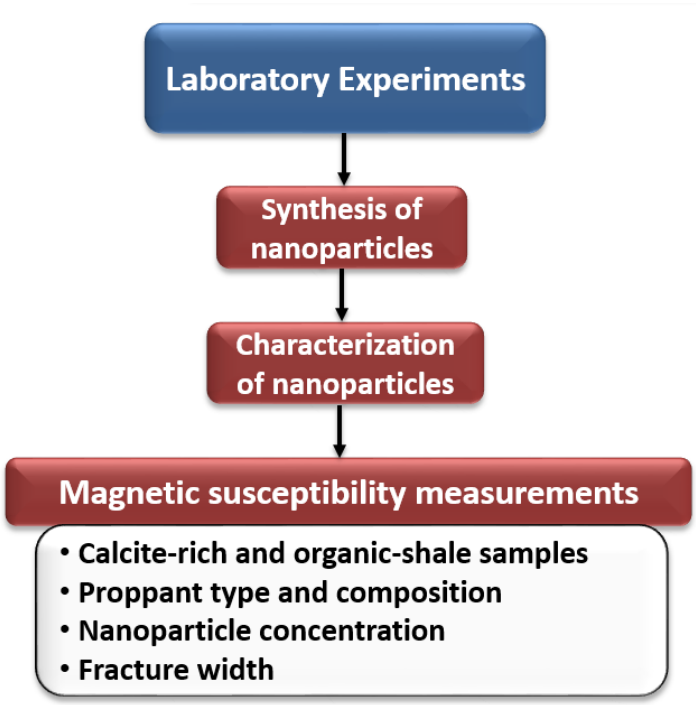

Fig. 1.3—Workflow for the study on the application of magnetic nanoparticles mixed with propping agents in enhancing near-wellbore fracture detection.

1.6 Outline of Dissertation

This dissertation consists of five chapters, with Chapter I covering the background of the research, review of literature and overview of methods used in achieving the stated research objectives.

Chapter II introduces a new rock classification technique that integrates four rock classification schemes based on (a) geologic facies, (b) reservoir quality, (c) stress profile, and (d) completion quality. The techniques applied in these classification schemes include core description and thin section analysis, depth-by-depth formation characterization, geomechanical analysis, and artificial neural network analysis. The technique is applied to a well located at the Wolfcamp shale in the Delaware basin. The resulting classifications are used to identify target zones for hydraulic fracturing stimulation treatment in the Wolfcamp shale.

Chapter III focuses on a new technique based on interpretation of acoustic measurements using a granular effective media model, to quantify mechanical damage in propping agents used in hydraulic fracture completion designs.

Chapter IV, demonstrates a new technique for using nanoparticles as contrast agents mixed with proppants that can enhance borehole geophysical measurements, such as magnetic susceptibility, thereby improving the near-wellbore detection of proppants in hydraulic fractures.

Chapter V summarizes the conclusions of the research, and recommendations for future work.

CHAPTER II

INTEGRATED ROCK CLASSIFICATION IN THE WOLFCAMP SHALE FORMATION BASED ON GEOLOGICAL EVALUATION, RESERVOIR QUALITY, AND ANISOTROPIC STRESS PROFILE ESTIMATED FROM WELL LOGS*

A reliable rock classification is the key to identify target zones for successful hydraulic fracturing stimulation treatment in unconventional reservoirs such as organic-rich mudrocks. Such rock classification scheme should take into account geologic attributes, petrophysical and geomechanical properties (i.e., in-situ stress gradients and elastic properties) to improve the likelihood of successful fracture treatment. However, the conventional rock classification methods do not take into account stress gradients in the formation. I introduced a new rock classification technique that integrates four rock classification schemes based on (a) geologic facies, (b) reservoir quality, (c) stress profile, and (d) completion quality. The techniques applied in these classification schemes include core description and thin section analysis, well-log-based depth-by-depth petrophysical and compositional characterization, and analysis of geomechanical measurements. Geomechanical analysis of core measurements and well logs provided a depth-by-depth assessment of minimum horizontal stress assuming vertical transverse isotropy in the formation. I performed geologic facies and reservoir quality classification using an

*Reprinted with permission from "Integrated Rock Classification in the Wolfcamp Shale Formation Based on Reservoir Quality and Anisotropic Stress Profile Estimated from Well Logs" by Aderonke Aderibigbe, Clotilde Chen Valdes, and Zoya Heidari, 2016. *Interpretation*, **4** (2), Copyright 2016 by the Society of Exploration Geophysicists and American Association of Petroleum Geologists.

artificial neural network analysis, where well logs and well-log-based estimates of the petrophysical and compositional properties were inputs to the network.

The introduced technique was applied to a well located at the Wolfcamp shale in the Delaware basin. Based on the integrated rock classification results, I recommended the middle of the upper Wolfcamp and the bottom of the lower Wolfcamp depth intervals as the best candidates for fracture initiation and fracture containment zones, respectively. The selection of these zones were based on the reservoir quality and average minimum horizontal stress gradient calculated in these intervals. The proposed integrated rock classification technique can improve the planning and execution of completions design for hydraulic fracture treatments.

2.1 Introduction

The economical production of hydrocarbons from tight reservoirs depends on the design, execution and success of hydraulic fracturing treatments for the completion of these formations. The informed selection of fracturing fluids, additives, and proppants plays an important role in the design of hydraulic fracture stimulation treatments. However, even with the selection of the optimal treatment parameters, the effective execution of the hydraulic fracture is largely influenced by the selection of the target zones, as well as the fracture barrier zones. Tight reservoirs such as organic-rich mudrocks are characterized by inherent low permeability, variable mineralogy, and heterogeneity. Hence, a detailed evaluation that includes (1) petrophysical analysis for determining reservoir quality, (2) geologic attributes of the formation, and (3) geomechanical analysis

for determining the in-situ stress gradient, is required to identify the target and barrier zones for hydraulic fracturing. Previous publications have incorporated reservoir and geomechanical properties in optimizing reservoir and completion quality, in order to improve economical production in organic shale formations (Cadwallader et al., 2015; Jochen et al., 2011; Sebastian et al., 2015; Slocombe et al., 2013; Sun et al. 2015; Wigger et al., 2014). These publications have incorporated modelling studies (i.e. hydraulic fractures and reservoir fluid flow) with surveillance technologies (i.e. tracers, production logs, microseismic and fiber optics) applied to completed horizontal wells in the Eagle Ford formation. Well-log based rock classifications can provide the criteria for zone determination by integrating detailed petrophysical and geomechanical analysis with the geologic attributes of the formation, when data from completed wells is not available.

The rock classification approaches can be driven by geologic, petrophysical, or production goals (Rebelle and Lalanne, 2014). Previous publications introduced different methods for rock classification in organic-rich mudrocks. A core-based rock classification method was applied in the Barnett shale, where measurements of porosity, mineralogy, total organic content (TOC), and capillary pressure were used to identify petrofacies (Kale et al., 2010). Another core-based method applied in the Woodford shale, using additional measurements of acoustic velocities, bulk and grain densities, showed good conformity between identified different petro-types and production data (Gupta et al., 2012). Popielski et al. (2012) applied a rock classification technique using well logs and core data analysis. Their application of the developed technique in the Barnett and Haynesville shale gas formations showed that rock types can be associated with depositional environments and

rock-type facies distribution for integrated reservoir modeling. A direct application of well logs that incorporates the estimates of petrophysical, compositional, and elastic properties was developed and applied to the Haynesville shale (Aranibar et al., 2013; Saneifar et al., 2014). Rock classes were verified using thin section images and previously identified lithofacies. The inclusion of organic richness and brittleness in the techniques was proposed to improve the detection of fracture-initiating zones (Saneifar et al., 2014). These existing core-based and well-log-based rock classification techniques do not assimilate state of stresses in rock, which is important for identifying initiation and containment zones in hydraulic fracture treatments.

In a review of rock mechanics and fracture geometry, Warpinski and Smith (1989) showed that in-situ stresses are the most significant factors controlling hydraulic fracturing. The models used in estimating in-situ stress gradient assume either isotropic or anisotropic conditions in the formation. Organic shale formations exhibit anisotropy due to partial alignment of plate-like clay minerals, as well as the presence of laminations of organic material (Sayers, 2005; Sayers, 2013). Hence, it is essential to use appropriate models that account for anisotropy. Anisotropy in shales can be described by assuming vertical transverse isotropy (VTI) (Sayers, 1994; Tsvankin, 2005). In a VTI medium, the symmetry axis is such that the rock material property is the same along the directions transverse to the axis, but different in the direction perpendicular to the axis. Hence, VTI is the most common anisotropy model applied to account for anisotropy in organic shale formations (Tsvankin, 2005). Recent developments in acoustic logging measurements using the diploe sonic tool are now available to obtain anisotropic measurements. These

measurements can be used in estimating the anisotropic elastic properties and the minimum horizontal stress gradient using the VTI model (Higgins et al., 2008; Pistre et al., 2005; Walsh et al., 2006).

The objective in this chapter is to introduce a rock classification technique that takes into account the effects of stress anisotropy in addition to geologic attributes, and petrophysical and compositional properties of organic-rich mud rocks. I applied the classification technique for identification of best candidate zones for hydraulic fracture treatments in the Wolfcamp shale formation of the Delaware basin.

2.2 Method

The proposed integrated rock classification for the identification of completion zones for hydraulic fracture treatments includes four rock classification schemes. The first classification scheme is the geologic facies classification. I conducted geologic facies classification using a supervised artificial neural network (ANN) method with an input of well logs and pre-identified core-based geologic facies as the training dataset. The second classification scheme is the reservoir quality (RQ) classification. I conducted RQ classification using an unsupervised artificial neural network method with input of well-log-based estimates of petrophysical and compositional properties. The third classification scheme is the stress profile (SP) classification. Well-log-based estimates of the anisotropic stress gradient are inputs to the SP classification scheme. The fourth classification scheme is the completion quality (CQ) classification, which integrates the results of RQ and SP classifications for identification of candidate zones for completions design. **Fig. 2.1** shows

a summary of the workflow used in the integrated rock classification. The following sections describe the four classification schemes, and the methods used to obtain the required inputs to the different rock classification approaches.

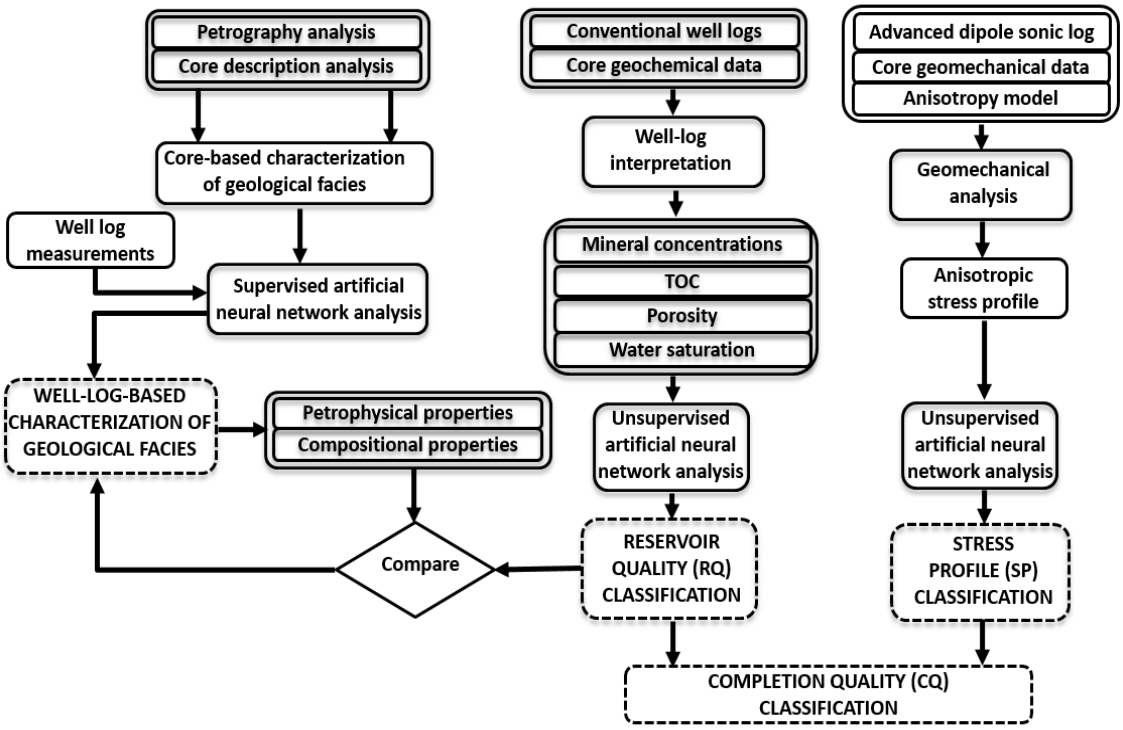

Fig. 2.1—A workflow illustrating the methods for the four classification schemes including geologic facies characterization, reservoir quality (RQ), stress profile (SP), and completion quality (CQ) classifications.

2.2.1 Geologic facies characterization

I applied a supervised artificial neural network (ANN) method using an input of well logs to characterize the depth-by-depth geologic facies of the formation. In the supervised learning method, a training dataset which consists of inputs and corresponding

desired outputs is provided to the network. The network learns the relationship between the components of the training dataset, and compares the resulting outputs against the desired output. A back-propagation algorithm was used to minimize the error between the resulting outputs and the desired outputs by continuously adjusting the weights controlling the network (Anderson and McNeil, 1992). The training dataset for the geologic facies characterization include input of well logs, and the desired output was core-based characterization of geologic facies at certain depth intervals. The input well logs include gamma ray, uranium concentration, photoelectric factor, compressional slowness, neutron porosity, bulk density and elemental capture spectroscopy (ECS) logs. I obtained the core-based characterization of geologic facies from analysis of thin section petrography and core description data which include information on lithology, sedimentary structures, fossils, and diagenetic features of the rock. The model created based on the pattern recognition between the input logs and the corresponding core-based geologic facies, was used for well-log-based characterization of the geologic facies for the remaining depth intervals of the formation.

2.2.2 Analysis of reservoir quality (RQ)

I applied an unsupervised artificial neural network method to determine rock classes based on RQ. The applied artificial neural network adopts a hierarchical clustering (HC) technique for classification. Unlike the supervised learning method adopted for geologic facies characterization, in the unsupervised learning method, the training data consists of only inputs, and there is no a priori output. Clustering algorithms such as

hierarchical and *k*-means clustering were used to organize the input data into clusters based on the measure of similarity, correlation, or distribution of density. The inputs to the method include well-log-based estimates of compositional (i.e., TOC and weight concentrations of calcite, illite, and quartz) and petrophysical (i.e., total porosity and water saturation) properties. The HC algorithm was applied to organize the input data into clusters that represent RQ classifications of the formation based on the petrophysical and compositional data in each cluster. The HC algorithm uses an agglomerative approach which minimizes the total within-group error sum of squares at each stage of clustering. This approach is referred to as the Ward's minimum variance method (Ward, 1963). The number of clusters was set to four to represent four RQ classifications (i.e., RQ1, RQ2, RQ3, and RQ4) in the field example of this chapter. The RQ decreases from RQ1 through RQ4, with RQ1 representing the rock class with best petrophysical and compositional properties. The rocks with best petrophysical properties are those with highest porosity, hydrocarbon saturation, and TOC. The best compositional properties refer to lowest concentration of clay minerals.

2.2.2.1 Assessment of TOC and volumetric concentration of kerogen

I applied the ΔlogR technique to estimate TOC, and then used the TOC estimates to quantify volumetric concentration of kerogen (Passey et al., 1990; Quirein et al., 2010). In this technique, I overlaid scaled porosity logs such as sonic, bulk density, and neutron porosity, on the deep resistivity curve. I then identified the baseline condition, where the curves (i.e., sonic/deep resistivity, and neutron porosity/deep resistivity) overlay each

other in an organic lean (i.e., non-source rock) interval over a significant depth range. The ΔlogR separation was calculated using the mathematical expression given by Equation 2.1

$$\Delta \log R = \log 10\left(R / R_{baseline} \right) + x\left(\Delta t - \Delta t_{baseline} \right), \tag{2.1}$$

where

$$x = \frac{Number\ of\ \log\ cycles}{\Delta t_{\max imum\ scale} - \Delta t_{\min imum\ scale}}, \tag{2.2}$$

Δt is the measured transit time, $\Delta t_{baseline}$ is the measured transit time of the identified baseline, *Rd* is the deep resistivity measurement, and $R_{baseline}$ is the deep resistivity measurement corresponding to the $\Delta t_{baseline}$ value. The Δt and $\Delta t_{baseline}$ parameters in Equation 2.1 were replaced with ϕ_N and $\phi_{N-baseline}$ parameters, when the neutron porosity, ϕ_N, curves were used.

I calculated the TOC as a function of maturity using the empirical correlation given by

$$TOC = \left(\Delta \log R \right) \times 10^{\left(2.297 - (0.1688 \times LOM) \right)}, \tag{2.3}$$

where LOM is the level of organic metamorphism. LOM was determined from available laboratory vitrinite reflectance, R_o, measurements. **Fig. 2.2** shows maturity in LOM units and their corresponding R_o according to the data reported by Hood et al., 1975. I compared the estimated TOC with core measurements of TOC obtained from pyrolysis experiments.

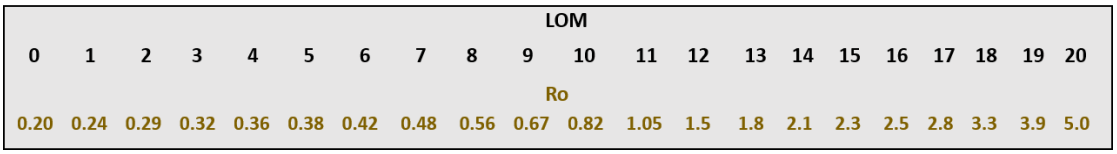

Fig. 2.2—Level of organic metamorphism (LOM) and their corresponding vitrinite reflectance, R_o (Data reported by Hood et al., 1975; Modified from Passey et al., 2010).

I estimated the volumetric concentration of kerogen using two approaches. In the first approach, I applied an empirical correlation between available core measurements of TOC and the volumetric concentration of kerogen from a nearby well. The volumetric concentration of kerogen was obtained from X-ray diffraction (XRD) measurements. In the second approach, I estimated the volumetric concentration of kerogen by converting the weight concentration of TOC using the expression given by Tissot and Welte (1978)

$$V_{\ker o} = \frac{W_{TOC}}{\kappa_{TOC}} \frac{\rho_b}{\rho_{\ker o}}, \tag{2.4}$$

where κ_{TOC} is the kerogen conversion factor, ρ_b is the bulk density, and ρ_{kero} is the density of kerogen. Published kerogen density data is approximately within the range of 1.2 to 1.4 g/cm^3, and I assumed ρ_{kero} as 1.4 g/cm^3 in my analysis. κ_{TOC} is the weight fraction of carbon in a typical kerogen. The published value of κ_{TOC} ranges from 0.68 to 0.95. In my analysis, I assumed a medium value of 0.8 for κ_{TOC} (Tissot and Welte, 1978).

2.2.2.2 Assessment of petrophysical and compositional properties

I applied joint inversion of available well logs including bulk density, photoelectric factor, neutron porosity, compressional slowness, resistivity and ECS, to estimate total porosity, TOC, water saturation, and volumetric concentrations of minerals. The ECS logs include aluminum, calcium, gadolinium, iron, silicon, sulfur, and titanium weight concentrations. The mineral components assumed in multi-mineral model for three Wolfcamp shale interval include illite, quartz, potassium and calcium feldspars, calcite, dolomite, pyrite and kerogen. These mineral components were identified from core X-ray diffraction (XRD) measurements. I then added the volumetric concentration of kerogen, and regional correlation observed between the minerals concentrations, as constraints in the multimineral model, to reduce the non-uniqueness of the results. I used ΔlogR technique to estimate TOC, and then used the TOC estimates to quantify volumetric concentration of kerogen (Passey et al., 1990; Quirein et al., 2010). I used the dual water model (Clavier et al., 1977) to estimate the depth-by-depth water saturation. **Table 2.1** summarizes the assumed parameters for dual water model and fluid properties. The estimates of petrophysical and formation properties were cross validated using core measurements.

Table 2.1—The assumed parameters for dual water model and fluid properties.

Parameter	Units	Upper Wolfcamp	Middle and Lower Wolfcamp
Archie's porosity exponent , *m*	( )	2	1.8
Archie's saturation exponent, *n*	( )	2	2
Formation water resistivity	ohm.m	0.061	0.057
Formation Temperature (deep)	^{o}C	67	83
Mud filtrate resistivity @ 20^{o}C	ohm.m	0.15	5
Formation Temperature (shallow)	^{o}C	20	20

2.2.3 Analysis of stress profile (SP)

I applied *k*-means clustering technique to classify rocks based on variation in minimum horizontal stress gradient along the depth intervals of interest. *k*-means clustering technique is an unsupervised learning method in which the algorithm partitions the input data into *k* clusters with each data belonging to the cluster with the nearest sample mean (MacQueen, 1967). The number of clusters is set to four to represent four SP classifications (i.e., SP1, SP2, SP3, and SP4). The minimum horizontal stress gradient for the SP classification increases from SP1 through SP4, with SP1 representing the rock class with the lowest minimum horizontal stress gradient. The VTI model was applied to estimate the elastic stiffness tensor using core geomechanical measurements and borehole acoustic measurements from dipole sonic tool. The elastic stiffness tensor was used to estimate the minimum horizontal stress, which was used to assess the anisotropic stress gradient in the formation. The following section describes the methods used for assessment of geomechanical properties in detail.

2.2.3.1 Assessment of geomechanical properties

Using the general form of Hooke's Law for a purely linear elastic medium, strain is linearly related to stress and is expressed as

$$\sigma_{ij} = C_{ijkl}\varepsilon_{ij}, \tag{2.5}$$

where σ_{ij} is the stress tensor, ε_{ij} is the strain tensor, and C_{ijkl} is the stiffness tensor. In a vertical transverse isotropy medium, the elastic stiffness tensor in the Voigt notation has the form of

$$C_{ijkl} = C_{IJ}^{VTI} = \begin{pmatrix} C_{11} & C_{12} & C_{13} & 0 & 0 & 0 \\ C_{21} & C_{22} & C_{23} & 0 & 0 & 0 \\ C_{31} & C_{32} & C_{33} & 0 & 0 & 0 \\ 0 & 0 & 0 & C_{44} & 0 & 0 \\ 0 & 0 & 0 & 0 & C_{55} & 0 \\ 0 & 0 & 0 & 0 & 0 & C_{66} \end{pmatrix}, \tag{2.6}$$

where C_{IJ}^{VTI} is the stiffness tensor in a VTI medium, with $C_{11} = C_{22}$, $C_{13} = C_{31} = C_{23} = C_{32}$, C_{33}, $C_{44} = C_{55}$ and C_{66}, as the five independent elastic stiffness coefficients (Nye, 1985). In addition, by symmetry, C_{66} can be estimated via

$$C_{66} = \frac{C_{11} - C_{12}}{2}. \tag{2.7}$$

C_{33} and C_{11} represent the vertically and horizontally propagating compressional waves, respectively, while C_{55} and C_{66} represent the vertically and horizontally propagating shear waves, respectively (Higgins et al., 2008; Walsh et al., 2006). C_{33}, C_{44} and C_{55} can be obtained using the compressional, fast-shear, and slow-shear slowness measurements from the acoustic tools and bulk density measurements. C_{33} and C_{44} can be estimated via

$$C_{33} = \rho V_p^{\,2}\left(0^0\right) \tag{2.8}$$

and

$$C_{44} = \rho V_s^{\,2}\left(0^0\right). \tag{2.9}$$

C_{66} can be estimated using the borehole Stoneley-wave slowness measurements (Frydman, 2010) via

$$C_{66} = \rho_f \frac{V_T^{\,2}\left(90^o\right)V_f^{\,2}}{V_f^{\,2} - V_T^{\,2}\left(90^o\right)}, \tag{2.10}$$

where V_p, V_s, and V_T are the compressional–, fast-shear–, and Stoneley–wave velocities, V_f is the drilling fluid velocity, ρ is the bulk density, and ρ_f is the drilling fluid density.

There are uncertainties associated with the estimation of C_{66} from borehole Stoneley-wave slowness. Stoneley waves are sensitive to factors such as the borehole fluid velocity, tool diameter, borehole radius and other formation properties. The borehole fluid properties such as V_f and ρ_f can be measured or estimated using drilling information such as the type of the drilling fluid (Tang et al. 1995). However, the uncertainty associated with measurements of drilling fluid velocity can be significant, which in turn introduces uncertainty in the estimates of C_{66}. I assumed an initial value for V_f in Equation 2.10, based on the reports provided by drilling and logging engineers, to estimate C_{66}. I then calibrated the estimated C_{66} through comparison of the well-log-based estimates against available core measurements of C_{66}.

Only three of the five independent elastic stiffness coefficients can be obtained from the available well logs. The remaining two elastic stiffness coefficients (C_{11} and C_{13}) can be estimated by applying anisotropic models such as ANNIE, modified ANNIE, and the further modified ANNIE models. In the ANNIE model (Schoenberg, 1996), the C_{11} and C_{13} coefficients are obtained by applying two constraints. The first constraint assumes that the Thomsen anisotropy parameter, δ, is set to zero, which enables the assessment of C_{13}. Thomsen (1986) defined three anisotropy parameters, ε, δ, and γ, when weak anisotropy is assumed in a VTI medium. The parameters ε, δ, and γ are given by

$$\varepsilon = \frac{\left(C_{11} - C_{33}\right)}{2C_{33}}, \tag{2.11}$$

$$\gamma = \frac{\left(C_{66} - C_{44}\right)}{2C_{44}}, \tag{2.12}$$

and

$$\delta = \frac{\left(C_{13} + C_{44}\right)^2 - \left(C_{33} - C_{44}\right)^2}{2C_{33}\left(C_{33} - C_{44}\right)}. \tag{2.13}$$

According to the first constraint, when δ, is zero, Equation 2.13 is reduced to

$$C_{13} + 2C_{44} - C_{33} = 0. \tag{2.14}$$

The second constraint of the ANNIE model assumes that in the case of shale formations,

$$C_{13} \equiv C_{12} = C_{11} - 2C_{66}. \tag{2.15}$$

Suarez-Rivera and Bratton (2009) introduced a modified version of the ANNIE model, referred to as the modified ANNIE (MANNIE), to improve the estimation of the stiffness coefficients. Quirein et al. (2014) reported that the ANNIE model predicts that the vertical Poisson's ratio, ν_{ver}, is always greater than or equal to the horizontal Poisson's ratio, ν_{hor}. Since this assumption is not always correct in anisotropic shale formations, they proposed a modification of the ANNIE model, which can be applied to cases where $\nu_{ver} \geq \nu_{hor}$ or $\nu_{ver} \leq \nu_{hor}$. In the modified ANNIE model, the stiffness coefficients C_{11} and C_{13} were estimated using the sequence of equations given in Equations 2.16 through 2.18 (Quirein et al., 2014)

$$C_{11\_Modified\ ANNIE} = k_1 C_{11\_ANNIE} = k_1\left(2\left(C_{66} - C_{44}\right) + C_{33}\right), \tag{2.16}$$

$$C_{12} = C_{11} - 2C_{66}, \tag{2.17}$$

and

$$C_{13} = k_2 C_{12}. \tag{2.18}$$

where k_1 and k_2 are the core-calibrated correction parameters.

In both the ANNIE and modified ANNIE models, C_{66} is required to estimate the remaining two stiffness coefficients. Murphy et al. (2015) proposed two other workflows to eliminate the uncertainty associated with the estimation of C_{66}. In the first workflow,

they proposed a further modified ANNIE model by introducing an additional core-calibrated parameter, k_3. They obtained k_3 from linear correlation between Thomsen parameters- ε and γ via

$$\gamma = k_3 \varepsilon. \tag{2.19}$$

C_{66} was then obtained by substituting Equations 2.19, 2.11 and 2.12, into Equation 2.16. via Murphy et al. (2015)

$$C_{66} = \frac{\left(1 + 2k_1 \frac{C_{44}}{C_{33}} - k_3 - k_1\right)}{2k_1 \frac{1}{C_{33}} - k_3 \frac{1}{C_{44}}}. \tag{2.20}$$

The second workflow given by Murphy et al. (2015) is a velocity regression method in which they reconstructed the sonic wave velocities at 45^o and 90^o. They derived linear correlations from core measurements of sonic wave velocities at 0^o, and sonic wave velocities at 45^o and 90^o. C_{11}, C_{66} and C_{33} are then estimated using Equations 2.21, 2.22, and 2.23 via

$$C_{11} = \rho V_p^{\,2}\left(90^0\right), \tag{2.21}$$

$$C_{66} = \rho V_s^{\,2}\left(90^0\right), \tag{2.22}$$

and

$$C_{13} = -C_{44} + \sqrt{\left[\left(C_{11} + C_{44} - 2\rho V_p^2(45^o)\right)\left(C_{33} + C_{44} - 2\rho V_p^2(45^o)\right)\right]}, \quad (2.23)$$

respectively.

Other methods for obtaining the VTI stiffness coefficients, particularly in deviated wells, include the linear inversion of shear wave anisotropic parameters (Chi et al., 2006) and the application of walkaway vertical seismic profiling (VSP) data (Horne et al., 2010). In this chapter, I applied three anisotropic model approximations including, ANNIE, modified ANNIE, and further modified ANNIE models in estimating the dynamic stiffness coefficients. I also applied empirical correlations derived from core measurements from experimental dynamic and static triaxial tests to convert the dynamic stiffness coefficients to the static stiffness coefficients.

The anisotropic stress gradient assessment was carried out under the assumptions of VTI using the poroelasticity model, modified after the Eaton's equation (Eaton, 1969), given by

$$\sigma_h = \alpha_h P_p + \frac{E_h}{E_v}\frac{\upsilon_v}{1-\upsilon_h}\left(\sigma_v - \alpha_v P_p\right) + \left(\frac{E_h}{1-\upsilon_h^2}\right)\varepsilon_h + \left(\frac{E_h \upsilon_h}{1-\upsilon_h^2}\right)\varepsilon_H, \quad (2.24)$$

where σ_h is the minimum horizontal stress, σ_v is the overburden stress, P_p is the pore pressure, α_h and α_v are the horizontal and vertical Biot's poroelastic parameters, respectively, E_h and E_v are the horizontal and vertical Young's modulus, respectively, υ_h and υ_v are the horizontal and vertical Poisson's ratio, respectively, and ε_h and ε_H are the

minimum and maximum horizontal strains respectively. The horizontal and vertical Young's modulus and Poisson's ratio can be expressed in terms of elastic stiffness coefficients via (Podio et al., 1968)

$$E_v = C_{33} - \frac{2C_{13}^{\ 2}}{C_{11} + C_{12}}, \tag{2.25}$$

$$E_h = C_{11} + \frac{C_{13}^{\ 2}\left(C_{12} - C_{11}\right) + C_{12}\left(C_{13}^{\ 2} - C_{12}C_{33}\right)}{C_{33}C_{11} - C_{13}^{\ 2}}, \tag{2.26}$$

$$\upsilon_v = \frac{C_{13}}{C_{11} + C_{12}}, \tag{2.27}$$

and

$$\upsilon_h = \frac{C_{33}C_{12} - C_{13}^{\ 2}}{C_{33}C_{11} - C_{13}^{\ 2}}. \tag{2.28}$$

After substituting Equations 2.25 through 2.28 in Equation 2.24, the anisotropic stress gradient can be estimated via (Thiercelin and Plumb, 1994; Savage et al., 1992)

$$\sigma_h = \alpha_h P_p + \frac{C_{13}}{C_{33}}\left(\sigma_v - \alpha_v P_p\right) + \left(C_{11} - \frac{C_{13}^{\ 2}}{C_{33}}\right)\varepsilon_h + \left(C_{12} - \frac{C_{13}^{\ 2}}{C_{33}}\right)\varepsilon_H, \tag{2.29}$$

The inputs for estimating the poroelastic coefficients α_h and α_v are the bulk modulus of the mineral phase, K_m, as well as the dry elastic stiffness coefficients, C_{IJ}^{dry}. α_h and α_v can be estimated via (Cheng, 1997)

$$\alpha_h = 1 - \frac{\left(C_{11}{}^d + C_{12}{}^d + C_{13}{}^d\right)}{3K_m}, \tag{2.30}$$

and

$$\alpha_v = 1 - \frac{\left(2C_{13}{}^d + C_{33}{}^d\right)}{3K_m}. \tag{2.31}$$

I obtained K_m by applying the Voigt-Reuss-Hill effective medium model (Hill, 1952) given by

$$M_{VRH} = \frac{M_V + M_R}{2}, \tag{2.32}$$

where

$$M_V = \sum_{i=1}^{N} f_i M_i \tag{2.33}$$

and

$$\frac{1}{M_R} = \sum_{i=1}^{N} \frac{f_i}{M_i}, \tag{2.34}$$

where M_{VRH} is the VRH average of the bulk or shear moduli, M_V and M_V are the Voigt upper bound and Reuss lower bound of the effective elastic modulus respectively, N is the number of phases, and f_i and M_i are the volume fraction and elastic modulus of the ith mineral component, respectively. **Table 2.2** lists the assumed bulk moduli for the mineral components used in estimating the bulk modulus of the mineral phase, K_m.

An approximate form of the Gassmann fluid substitution equation (Gassmann, 1951) for vertically propagating compressional waves in a VTI media, proposed by Mavko and Bandyopadhyay (2008), was applied to estimate the dry stiffness coefficient C_{33}^{dry} using the saturated stiffness coefficient C_{33}^{sat}.

$$C_{33}^{dry} \approx C_{33}^{sat} - \left[\frac{\left(\frac{K_{fl}}{K_m}\right)\left(K_m - K_{iso}^{sat}\right)^2}{\phi\left(K_m - K_{fl}\right) - \left(\frac{K_{fl}}{K_m}\right)\left(K_m - K_{iso}^{sat}\right)^2} \right] \times \left[1 - \delta \frac{\left(\frac{4}{3}\right) C_{33}^{sat}}{\left(K_m - K_{iso}^{sat}\right)} \right], \tag{2.35}$$

where K_{fl} is bulk modulus of the fluid mixture and is calculated using Wood's equation (Wood, 1955) given by

$$K_{fl} = \left(\sum_{i=1}^{n_f} S_i K_{fi}^{-1} \right)^{-1}, \tag{2.36}$$

where n_f is the number of fluid phase components, S_i and K_{fi} are the fluid saturation and bulk modulus of the ith component of the fluid phase, respectively. K_{iso}^{sat} is the apparent isotropic bulk modulus of the saturated rock, calculated from the vertical compressional- and shear-wave velocities via

$$K_{iso}^{sat} = \rho\left(V_p^2 - \frac{4}{3} V_s^2 \right). \tag{2.37}$$

Similar to the assumptions behind the fluid substitution models, the anisotropic form of approximation given by Equation 2.35 is best suited for low frequency data and rocks

that do not have very low porosity (Mavko and Bandyopadhyay, 2008; Mavko et al., 2009). Furthermore, similar to the isotropic Gassmann formulations, the effective shear moduli does not change due to a change in the pore fluid in the anisotropic rock. Hence, in this chapter, I assumed that the elastic stiffness coefficients C_{44} and C_{66} remain constant at dry and saturated conditions.

Table 2.2—The assumed bulk moduli, K_i, for the mineral components existing in the Wolfcamp shale formation.

Mineral component	K_i (GPa)
Calcite	73.3
Dolomite	94.9
K-feldspar	37.5
Plagioclase	76.0
Quartz	37.8
Illite	60.0
Kerogen	2.9
Pyrite	142.7

2.2.4 Analysis of completion quality (CQ)

I defined the CQ as a composite classification that integrates the RQ classification with the SP classification. The CQ represents an integrated rock classification that can be used to make decisions on the selection of candidate zones for fracture initiation and containment in completions design. I applied a conjunction operator which combines the four RQ and the four SP classes via

$$CQ = RQ \wedge SP. \tag{2.38}$$

The output of the conjunction operator is a knowledge-based system with four CQ classes (i.e., CQ1, CQ2, CQ3, and CQ4). **Figure 2.3** illustrates how this conjunction operator works. CQ1 represent rocks with high RQ and low stress gradient. CQ2 include depth intervals with low RQ and low stress gradient. CQ3 and CQ4 represent the rocks types with high stress gradient, with high and low reservoir qualities, respectively.

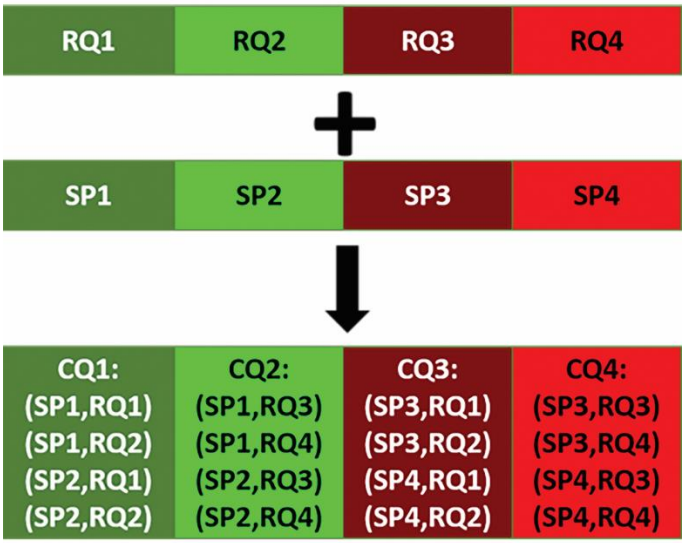

Fig. 2.3—The workflow used for completion quality classification through combining the RQ and SP classification results.

2.3 Field Example: The Wolfcamp Formation

I applied the proposed integrated rock classification technique to a well located in the Wolfcamp formation of the Delaware basin. The Wolfcamp formation has an average thickness of 609 m (2000 ft.), and consists of interbedded siliclastic mudrocks and carbonates. The porosity ranges from 4% to 10%, and the total organic content in the

organic rich facies is between 2 wt.% to 4 wt.% (Azike et al., 2014; Rafatian and Caspan, 2015). The Wolfcamp formation can be subdivided into three major intervals designated as upper, middle, and lower Wolfcamp. These Wolfcamp intervals are characterized by heterogeneous rock properties and geologic complexity. Hence, a good understanding of their variability is essential for an optimized completion and stimulation design. The knowledge of the geologic attributes and geomechanical properties such as the minimum in-situ stress would improve the identification of target intervals for fracture stimulation, and fracture barriers (Malik et al., 2013). The following sections include geologic description of the Wolfcamp formation, and the results and discussions on the assessment of the TOC, petrophysical, compositional and geomechanical properties. The results of the four classification schemes based on geologic facies, RQ, SP, and CQ in the Wolfcamp formation are also presented.

2.3.1 Geologic description

The Delaware basin originated in the Proterozoic era and persisted throughout the Paleozoic era, initially as part of the Tobosa basin, and then as a component sub-basin of the Greater Permian basin (GPB) in west Texas and the southeastern New Mexico (Hill, 1984). Other component sub-basins in the GPB include the Midland basin and the central basin platform. The Delaware basin has a deposition of shales with high organic contents because of the slight restriction of marine circulation in the basin through much of the Paleozoic era (Hill, 1984). The geologic formations of the Permian in the Delaware basin, from youngest to the oldest in geologic age includes the Leonardian, Wolfcampian and

Pennsylvanian formations. The Leonardian formation consists of the Avalon, first, second, and third Bone Spring formations, while the Wolfcampian formation consists mainly of the Wolfcamp shale formation. **Fig. 2.4** shows the stratigraphic chart of the Delaware basin formations.

Era	System	Period	Series	Formations
Paleozoic	Permian	Guadalupian	Delaware Mountain Group	Lamar Bell Canyon Cherry Canyon Brushy Canyon
		Leonardian	Bone Spring	Upper Avalon Shale Lower Avalon Shale 1st Bone Spring 2nd Bone Spring 3rd Bone Spring
		Wolfcampian	Wolfcamp	Wolfcamp
	Pennsylvanian	Pennsylvanian		Cisco Canyon Strawn Atoka Morrow

Fig. 2.4—Chronostratigraphic chart of the Delaware basin.

2.3.2 Results and discussion

Fig. 2.5 shows the results of the TOC assessment using the ΔlogR technique for the upper Wolfcamp interval, and **Fig. 2.6** shows the results of the TOC assessment for both the middle and lower Wolfcamp intervals.

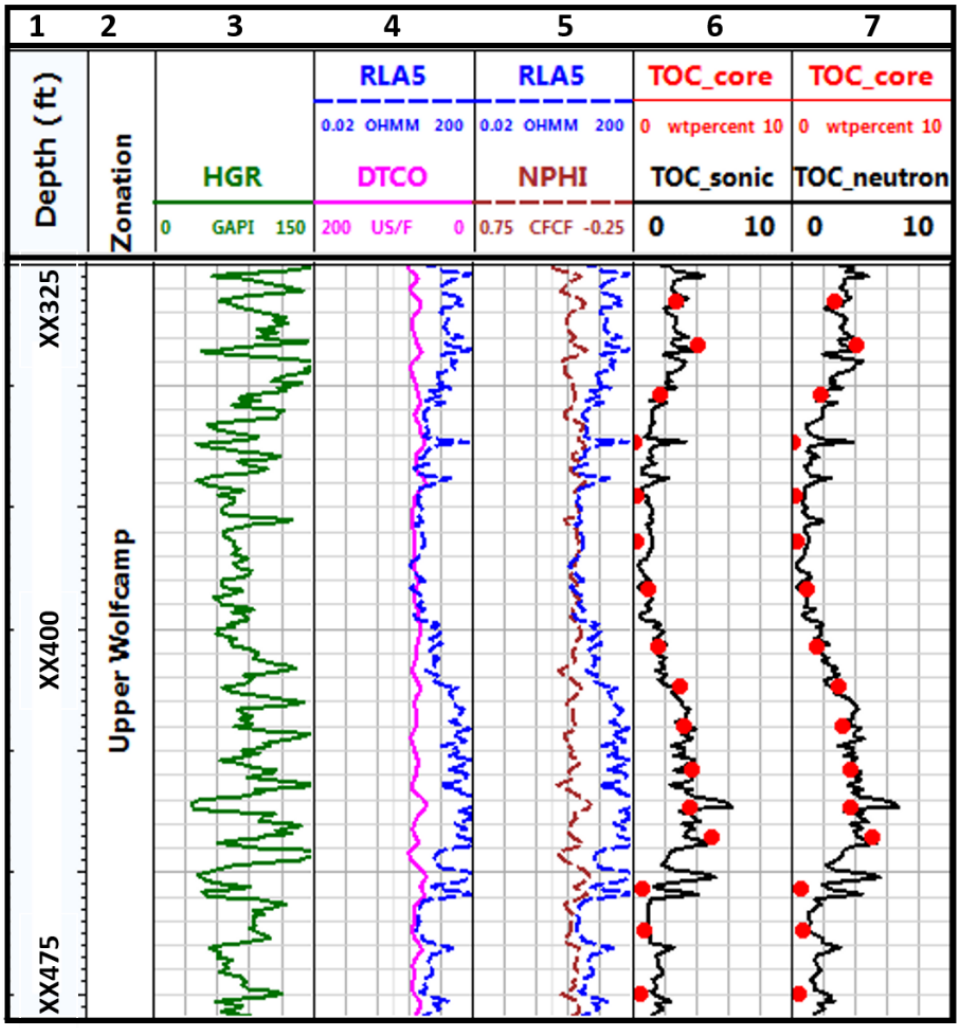

Fig. 2.5—Upper Wolfcamp: Assessment of TOC using ΔlogR technique. Tracks from left to right include, Track 1: depth; Track 2: zonation; Track 3: gamma ray; Track 4: compressional slowness/ deep resistivity overlay; Track 5: neutron porosity/ deep resistivity overlay; Tracks 6-7: estimates of TOC and core TOC measurements.

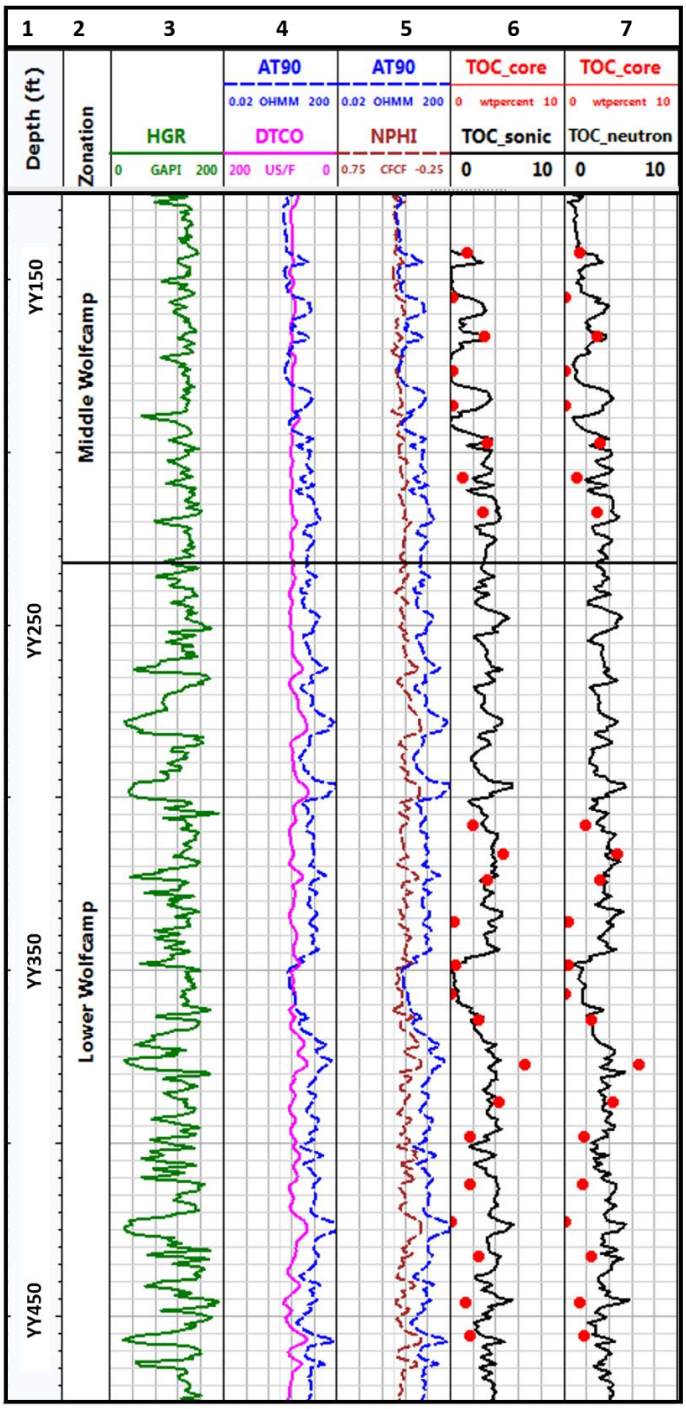

Fig. 2.6—Middle and Lower Wolfcamp: Assessment of TOC using ΔlogR technique. Tracks from left to right include, Track 1: depth; Track 2: zonation; Track 3: gamma ray; Track 4: compressional slowness/ deep resistivity overlay; Track 5: neutron porosity/ deep resistivity overlay; Tracks 6-7: estimates of TOC and core TOC measurements.

Track 6 (in both Figs. 2.5 and 2.6) show results of the depth-by-depth estimates of the TOC and the comparison with the core TOC measurements when assessment was carried by overlaying sonic and deep resistivity curves. Track 7 (in both Figs. 2.5 and 2.6) shows similar results for the assessment carried out by overlaying neutron porosity and deep resistivity curves. Both TOC estimates in Tracks 6 and 7 (in both Figs. 2.5 and 2.6) show a good match with the core TOC measurements. The TOC estimates in the upper Wolfcamp interval show a better match to the core measurements compared to the middle and lower Wolfcamp intervals. These TOC estimates were used in calculating the volumetric concentration of kerogen using the two approaches mentioned earlier.

Fig. 2.7 shows the core-derived correlation between the weight concentration of TOC, W_{TOC}, and core volumetric concentration of kerogen, $V_{kerogen}$. This correlation was used in the first approach for estimating the depth-by-depth volumetric concentration of kerogen. In the second approach, I estimated the volumetric concentration of kerogen using Equation 2.4. **Fig. 2.8** shows the comparison between the estimates of the volumetric concentrations of kerogen. The results suggests that the volumetric concentration of kerogen obtained from the two approaches were in good agreement. I observed a good match between the estimated $V_{kerogen}$, which demonstrates that the assumed κ_{TOC} of 0.8 was a good approximation for the Wolfcamp shale formation. $V_{kerogen}$ estimates were used in the multimineral solver as a constraint.

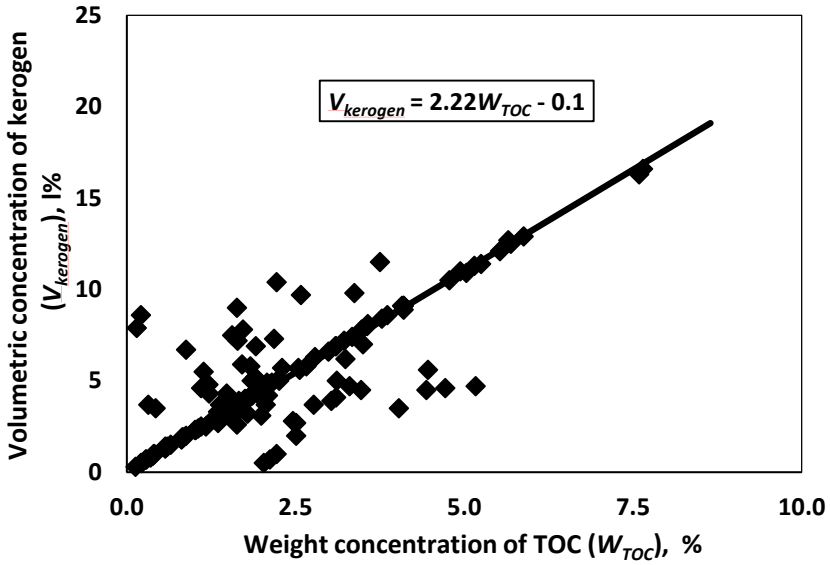

Fig. 2.7—Correlation between weight concentration of TOC from core pyrolysis experiments, and volumetric concentration of kerogen from core XRD analysis.

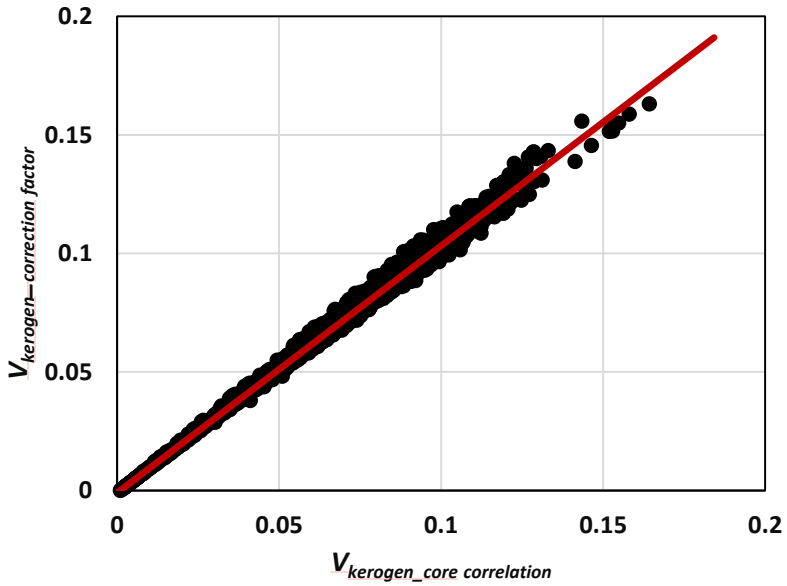

Fig. 2.8—Comparison of depth-depth estimation of the volumetric concentration of kerogen using the two approaches including core data correlation and conversion of the weight concentration of TOC.

The regional mineral correlations for the three Wolfcamp intervals were also used as constraints to the multimineral solver. **Figs. 2.9a** and **2.9b** show the Upper Wolfcamp regional mineral correlations between calcium feldspar and potassium feldspar, and between calcite and calcium feldspar, respectively. For the middle Wolfcamp, I used empirical correlations between illite and potassium feldspar, as well as correlations between dolomite and calcium feldspar, as constraints. For the lower Wolfcamp, I used empirical correlations between calcium feldspar and quartz, as a constraint. **Fig. 2.10** shows the estimated TOC, mineral concentrations, porosity, and water saturation for the three depth intervals in the Wolfcamp formation. **Table 2.3** summarizes the absolute errors in well-log-based estimates of compositional and petrophysical properties compared to core measurements. The absolute error (i.e., Root Mean Square Error (RMSE)) was calculated via

$$error = \sqrt{\frac{1}{n}\sum_{i=1}^{n}\left|x_{est_i} - x_{core_i}\right|^2}, \tag{2.39}$$

where n is the total number of available measured/estimated points, x is the parameter of interest (i.e., petrophysical and compositional properties), x_{est} is the well-log-based estimate, and x_{core} is the core measurement. The error in estimates of volumetric concentration of dolomite was due to the absence of magnesium weight concentration in ECS logs and the associated non-uniqueness of the results. I quantified the impact of including dolomite and the uncertainty related to the presence of dolomite on the well-log-based estimates of petrophysical and compositional properties. The last column on

Table 2.3 shows the comparison of the errors in the well-log-based estimates of mineral composition for an additional case where dolomite was not included as a mineral component in the multi-mineral model. The removal of dolomite leads to approximately 0.6% decrease of absolute errors in estimates of quartz, clay, and potassium feldspar volumetric concentrations, and approximately 2.5% increase of absolute errors in estimates of calcite and calcium feldspar volumetric concentrations. The results confirmed that the impact of uncertainty estimates of dolomite on the results of multi-mineral analysis was not significant.

Table 2.3—Absolute errors in well-log-based estimates of compositional and petrophysical properties compared to core measurements.

Mineral / Petrophysical properties	Absolute errors with Dolomite, %	Absolute errors without Dolomite, %
Quartz	17.8	16.5
Clay	14.7	13.4
Calcite	17.7	19.2
Dolomite	17.6	--
Plagioclase	9.7	12.7
K-Feldspar	2.9	2.3
Pyrite	2.7	3.2
TOC	1.5	1.5
Total porosity	4.4	4.4
Water saturation	27.8	27.8

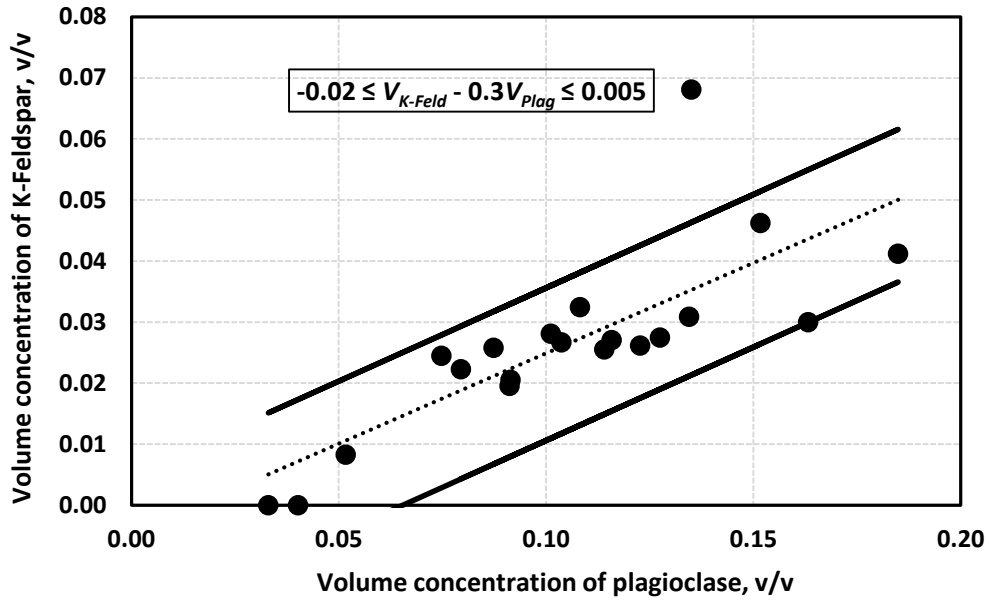

(a)

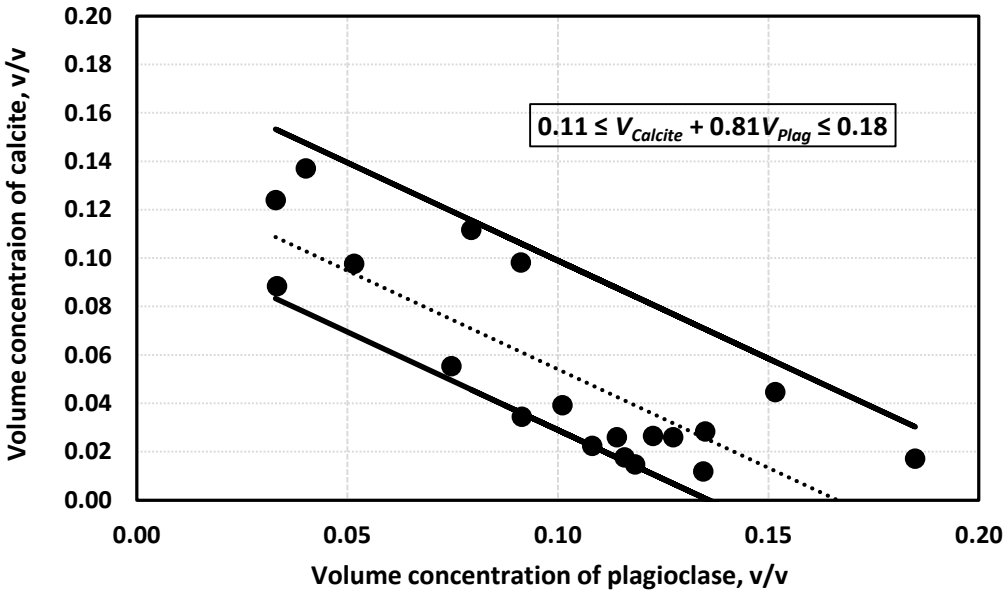

(b)

Fig. 2.9—Upper Wolfcamp: Correlation between volume concentrations obtained from XRD measurements for (a) plagioclase and potassium feldspar, and (b) plagioclase and calcite. These mineral correlations are applied as constraints in the multi-mineral model, to reduce the non-uniqueness of estimated properties.

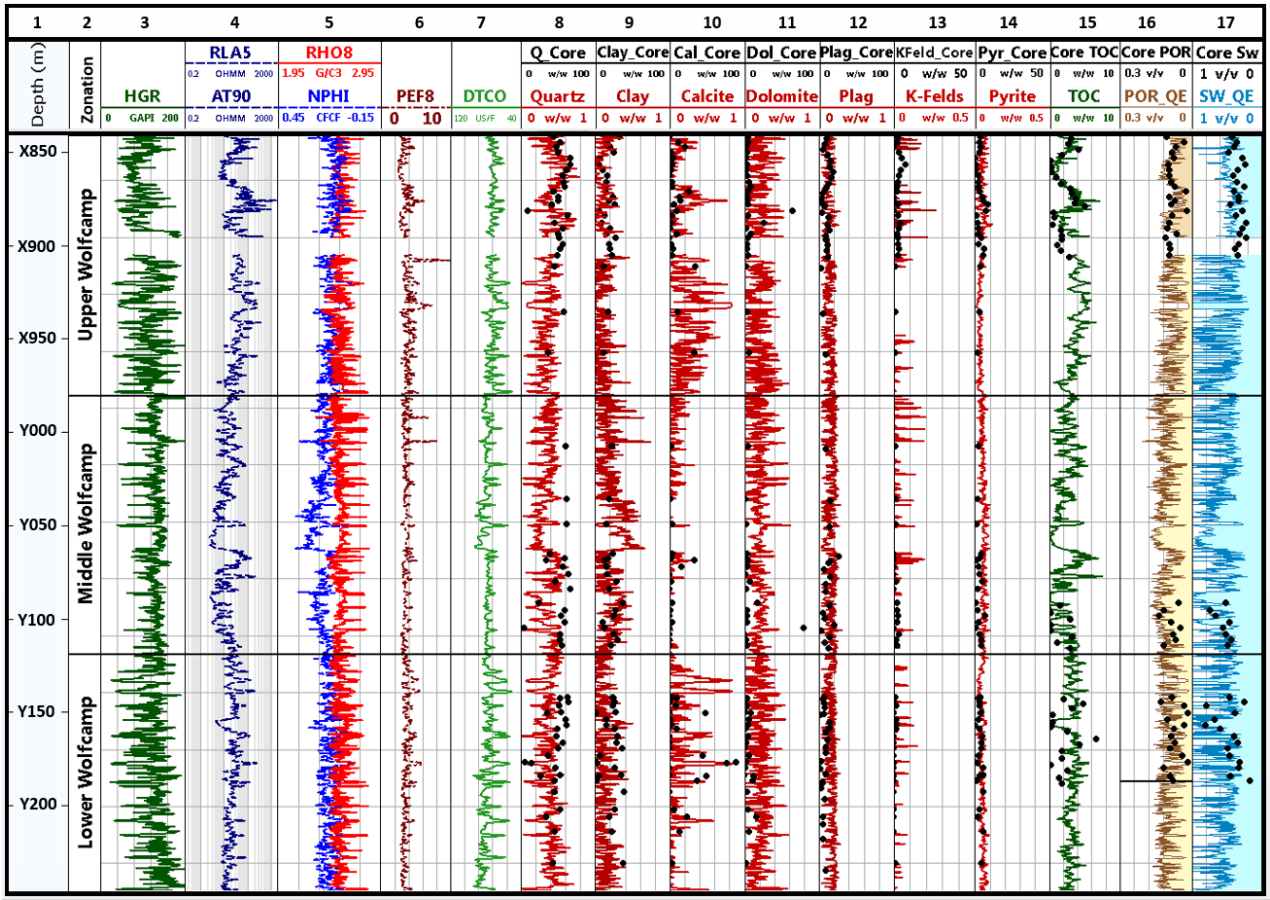

Fig. 2.10—Wolfcamp formation: Conventional well logs and estimates of petrophysical and compositional properties. Tracks from left to right include, Track 1: depth; Track 2: zonation; Tracks 3-7: gamma ray, apparent resistivity logs, neutron porosity /bulk density, PEF, and compressional slowness. Tracks 8-14: estimates of volumetric concentrations of minerals; Tracks 15-17: estimates of TOC, total porosity and water saturation.

Fig. 2.11a compares the dynamic horizontal Poisson's ratio, v_{hor}, to the dynamic vertical Poisson's ratio, v_{ver}, measured from triaxial tests. For the depths of core tested in the Wolfcamp shale intervals, I observed that v_{ver} is greater than or equal to v_{hor}. Since the aforementioned observation is in agreement with the prediction of ANNIE model that $v_{ver} \geq v_{hor}$, then the ANNIE model approximations can be applied in the estimation of the stiffness coefficients (Quirein et al., 2014). I estimated the dynamic stiffness coefficients for the core data for the Wolfcamp shale formation cores from the measured compressional- and shear-wave velocities. I also estimated the dynamic stiffness coefficients C_{11}, C_{12}, and C_{13} using the sequence of equations for the ANNIE (Equations 2.14 and 2.15), and the modified ANNIE model (Equations 2.16 through 2.18) approximation models. **Fig. 2.11b** compares the actual core stiffness coefficient C_{11} to the ANNIE stiffness coefficient C_{11}. The resulting core-calibrated correction parameter k_1 in the modified ANNIE model (Equation 2.16) for the cores for the Wolfcamp shale is 1.1, which is almost similar to the original ANNIE model assumption value of 1. In the analysis by Quirein et al. (2014), a general value of 1.1, was also obtained for k_1 using a combined dataset of cores from the Bakken, Bazhenov, and Niobara shales (Murphy et al. 2015). **Fig. 2.11c** compares the actual core stiffness coefficient C_{13} to the actual core stiffness coefficient C_{12}. The resulting core-calibrated correlation correction parameter k_2 in the modified ANNIE model (Equation 2.18) for the cores for the Wolfcamp shale is 0.96. Similarly, in the analysis by Quirein et al. (2014), a general value of 0.8, was obtained for k_2 using the combined dataset of cores from the Bakken, Bazhenov, and Niobara shales (Murphy et al. 2015).

Fig. 2.11d shows the correlation between the estimated anisotropy parameters ε and γ for the cores for the Wolfcamp shale. The resulting core-calibrated correlation correction parameter k_3 in the further modified ANNIE model (Equation 2.19) for the cores for the Wolfcamp shale is 1.5. Murphy et al. (2015) analyzed additional dataset from Monterey, Northsea, Lockatong (Vernik and Liu, 1997), as well as dataset from Barnett, Eagle Ford, and Haynesville shales (Sone, 2012), and obtained a general value of 0.93 for the parameter k_3. **Fig. 2.11e** shows the relationship between the static and dynamic shear moduli, while **Fig. 2.11f** shows the relationship between the static and dynamic compressional moduli, for the Wolfcamp shale. The empirical correlations derived from these relationships were used to convert the estimated dynamic stiffness coefficients to static stiffness coefficients.

Fig. 2.12 shows the acoustic logs, estimates of volumetric concentrations of minerals, and estimates of the geomechanical properties and estimates of the stress gradient in the upper Wolfcamp shale interval. I assumed a pore pressure gradient of 11.76 MPa/km (Friedrich and Monson, 2013) to estimate the pore pressure in the three Wolfcamp intervals. To assess stress gradient, I assumed uniaxial strain and integrated the density log to estimate the overburden stress. I observed no significant variation between the fast and slow shear waves (Track 4 of Fig. 2.12), and consequently no difference between the dipole shear moduli ($C_{44} = C_{55}$) as shown in Track 6 of Fig. 2.12, in the upper Wolfcamp interval. However, I observed that the horizontal shear modulus is higher than the dipole shear moduli ($C_{66} > C_{44} = C_{55}$) in some depth intervals in the top and lower sections of the upper Wolfcamp. This observation indicates that the formation is exhibiting

VTI anisotropy at these depth intervals. Track 8 of Fig. 2.12 compares the C_{66} estimated using the Stoneley-wave slowness against those estimated using the further modified ANNIE model. The differences in the C_{66} estimates are larger in the depth sections where the effect of anisotropy is more dominant. Track 10 of Fig. 2.12 compares the stress gradient obtained using stiffness coefficients estimated from the ANNIE, modified ANNIE, and the further modified ANNIE models. The ANNIE model provided the smallest values for the minimum horizontal stress gradient compared to the estimates from the modified ANNIE, and the further modified ANNIE models.

Fig. 2.13 shows the acoustic logs, estimates of volumetric concentrations of minerals, and estimates of the geomechanical properties and the stress gradient for the three intervals in the Wolfcamp shale formation. The stiffness coefficients were estimated using modified ANNIE model. I observed that intervals characterized by high gamma ray response and high TOC, exhibit VTI anisotropy ($C_{66} > C_{44} = C_{55}$). I also observed that the anisotropic Biot's parameters were not equal and maintain values of less than one at depth intervals exhibiting VTI anisotropy, in Track 9 of Fig. 2.13. The estimates of the anisotropic horizontal stress gradients shown in Track 10 of Fig. 2.13 quantify the stress contrast at different intervals in the Wolfcamp formation.

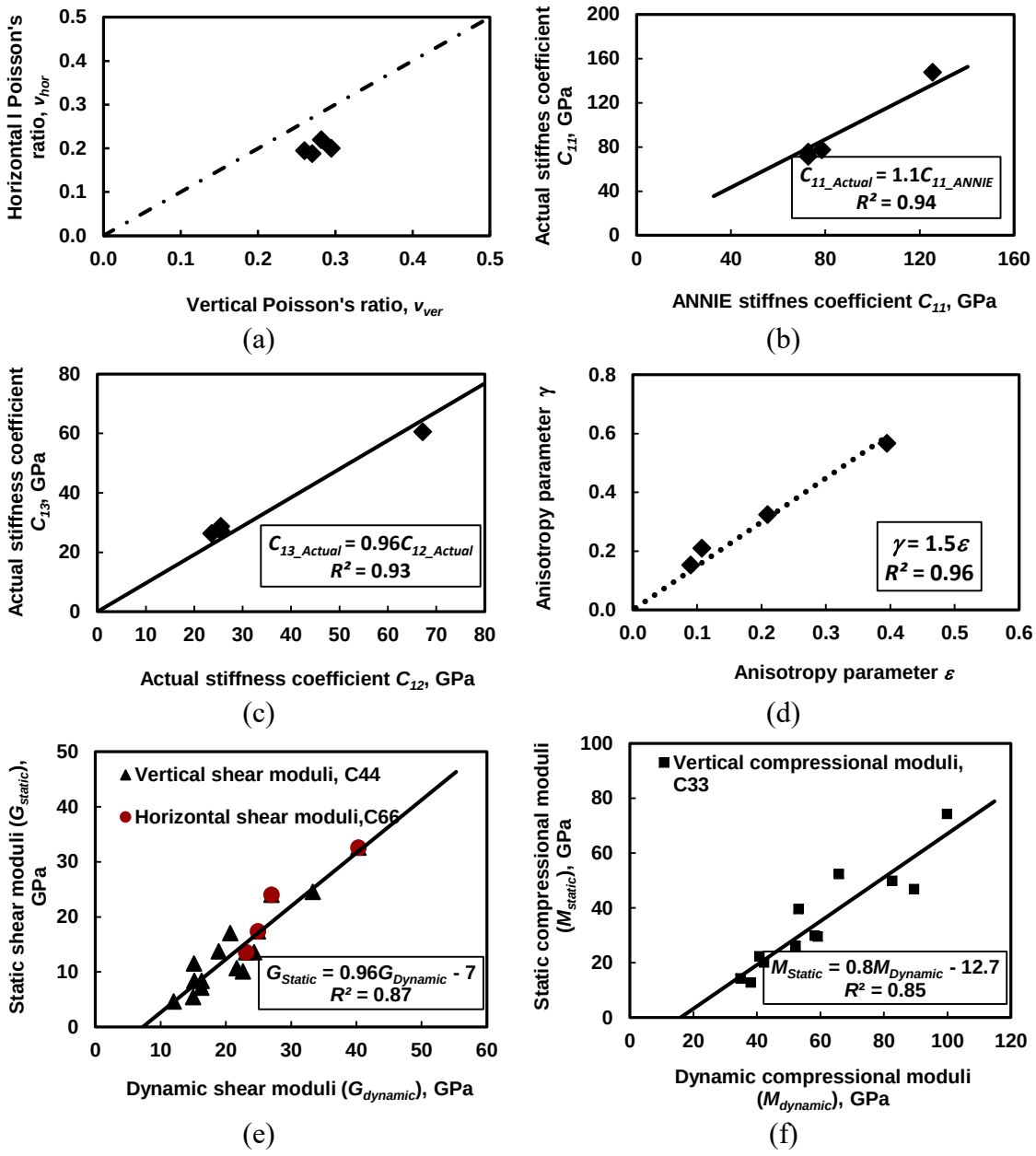

Fig. 2.11—Wolfcamp shale cores- (a) comparison of dynamic measurements of horizontal Poisson's ratio, v_{hor}, to the vertical Poisson's ratio, v_{ver}, (b) comparisons of actual core stiffness coefficient C_{11} to the ANNIE stiffness coefficient C_{11}, (c) comparisons of actual core stiffness coefficient C_{13} to the actual core stiffness coefficient C_{12}, (d) correlation between the estimated anisotropy parameters ε and γ, (e) linear relationship between the static and dynamic shear moduli, and (e) linear relationship between the static and dynamic compressional moduli.

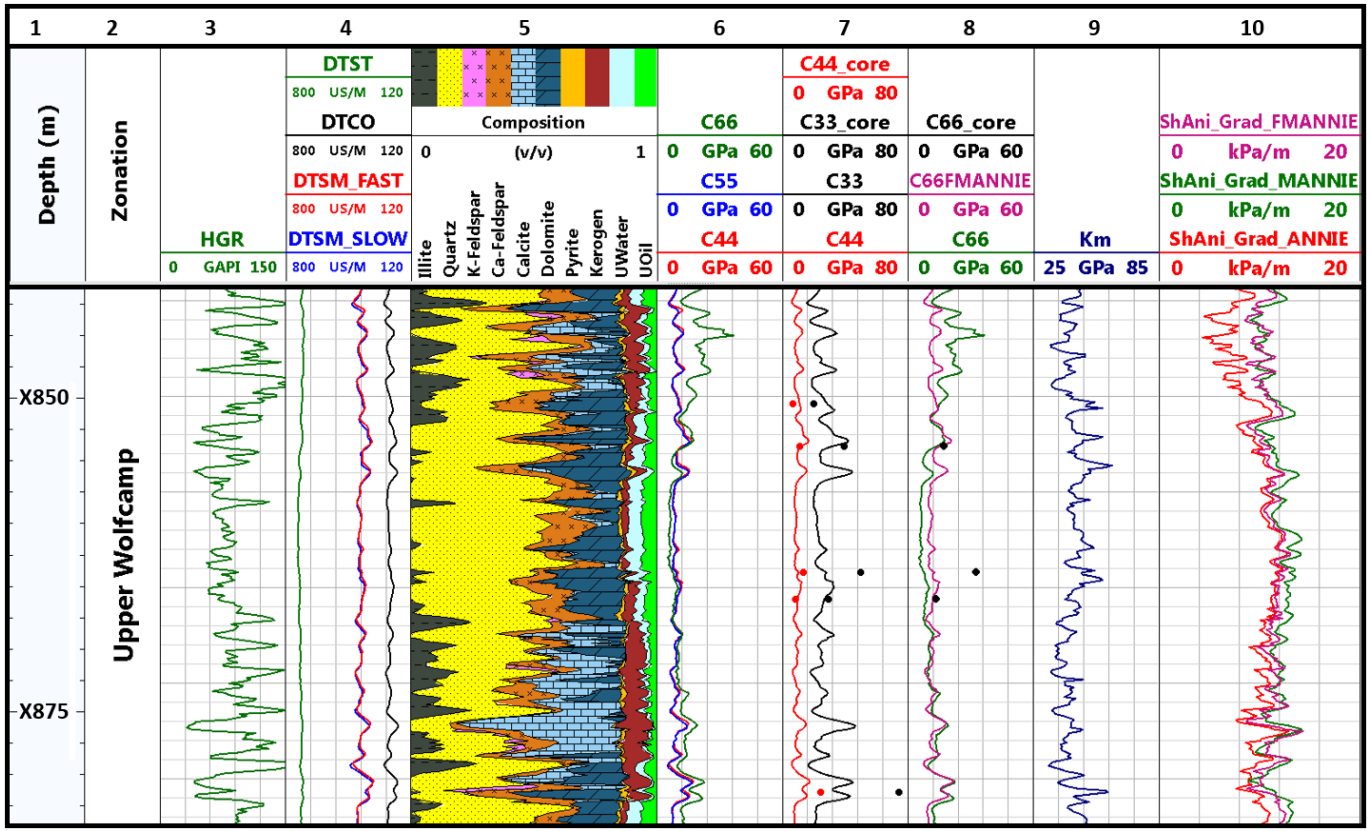

Fig. 2.12—Upper Wolfcamp formation: Well-log-based estimates of geomechanical properties. Tracks from left to right include, Track 1: depth; Track 2: zonation; Track 3-4: gamma ray, slowness (compressional-, shear-, and Stoneley-wave); Track 5: estimates of volumetric concentrations of minerals; Track 6-8: estimates of elastic stiffness coefficients; Track 9: well-log-based estimates of mineral modulus; Track 10: comparison of the of minimum horizontal stress pressure gradient estimated using stiffness coefficients estimated from the ANNIE model (*ShAni_Grad_ANNIE*), modified ANNIE model (*ShAni_Grad_MANNIE*), and further modified ANNIE models (*ShAni_Grad_FMANNIE*).

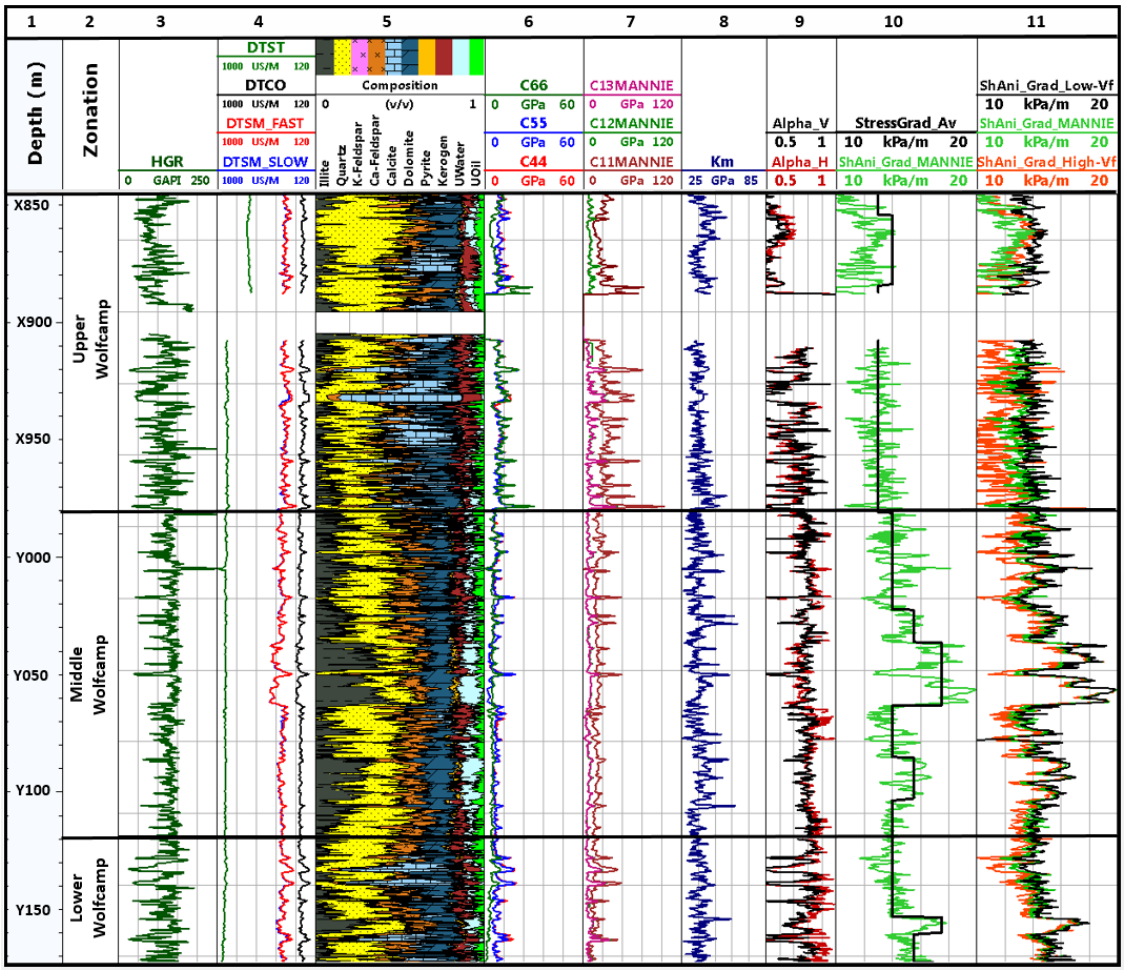

Fig. 2.13—Wolfcamp formation: Well-log-based estimates of geomechanical properties. Tracks from left to right include, Track 1: depth; Track 2: zonation; Track 3-4: gamma ray, slowness (compressional-, shear-, and Stoneley-wave); Track 5: estimates of volumetric concentrations of minerals; Track 6-7: estimates of elastic stiffness coefficients; Track 8: well-log-based estimates of mineral modulus; Track 9: estimates of horizontal and vertical Biot's coefficients; Track 10: estimate of minimum horizontal stress pressure gradient using the modified ANNIE model approximation; Track 11: comparison of anisotropic stress gradient estimated using the modified ANNIE model approximation and assuming 2% increase (ShAni_Grad_High-Vf), and 2% decrease (ShAni_Grad_Low-Vf) in drilling fluid velocity, V_f.

As explained in the method section, uncertainties in the assumed values for V_f could affect C_{66} estimates. **Fig. 2.14a** shows the sensitivity of C_{66} estimates to V_f when C_{66} is estimated using Equation 2.10. I observed that when V_f varies in the range of -2% to +2%, the corresponding change in C_{66} is about -23% to +44%. Track 11 in Fig. 2.13 shows the resulting uncertainty range in estimates of anisotropic stress gradient caused by uncertainty in assumed values of V_f. I observed an average relative change of 9% and 3% in the minimum horizontal stress gradient, when V_f is increased and decreased by 2%, respectively. Although the C_{66} estimates can be significantly affected by V_f assumptions, uncertainty in V_f values do not significantly affect estimates of minimum horizontal stress gradient. Reliable estimates of V_f through in-situ measurements can further improve the minimum horizontal stress gradient evaluation. The uncertainty in Stoneley-wave slowness measurements can also cause uncertainty in estimates of the minimum horizontal stress gradient. A sensitivity analysis showed that a 2% and 5% noise on Stoneley-wave slowness measurements, result in an average relative change of 3% and 5% in the minimum horizontal stress gradient, respectively. **Fig. 2.14b** summarizes the relative change in the minimum horizontal stress gradient with a ±2% variation in drilling fluid velocity, V_f, horizontal shear modulus, C_{66}, Stoneley-, compressional-, fast shear-, and slow shear-wave slowness, respectively.

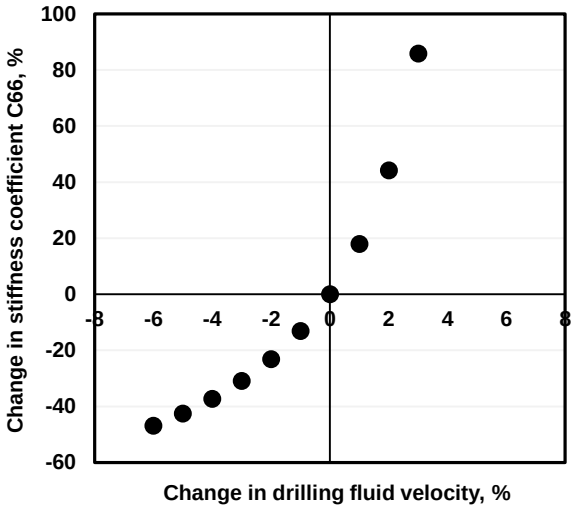

(a)

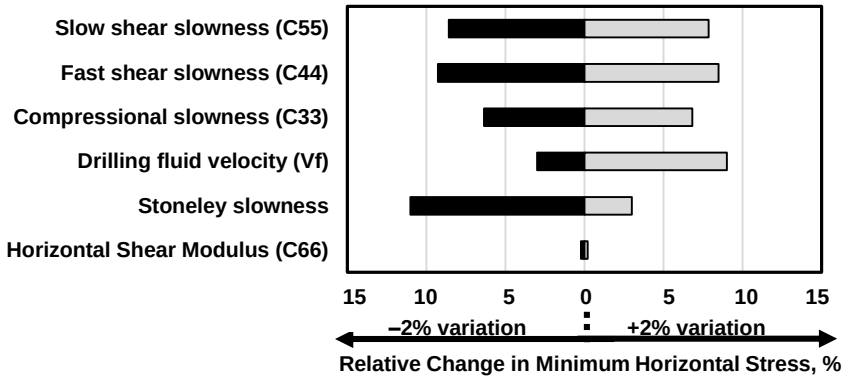

(b)

Fig. 2.14—(a) Sensitivity of stiffness coefficient (C_{66}) estimates to changes in the drilling fluid velocity, V_f, and (b) sensitivity of minimum horizontal stress to ±2% variation in drilling fluid velocity, V_f, horizontal shear modulus, C_{66}, Stoneley–, compressional–, fast shear–, and slow shear–slowness, respectively.

The three main categories of lithology types, identified from detailed core descriptions and thin section petrography, include limestones, mudstones, and siltstones. These general lithology types were further classified into six geologic facies taking into account the geologic attributes in the core descriptions. The six geologic facies include (a) silty mudstones, (b) calcareous mudstones, (c) dolomitic siltstones, (d) argillaceous siltstones, (e) calcareous argillaceous siltstones, and (f) argillaceous limestones. **Fig. 2.15** shows the mineral composition (Track 3) and the comparison of the well-log-based characterization of geologic facies (Track 5) to the core-based characterization of geologic facies (Track 4) in the upper, middle, and lower Wolfcamp intervals. I observed that the well-log-based classification provides similar facies as the core-based classification, despite the high heterogeneity in the formation. **Fig. 2.16** compares the estimates of TOC, water saturation, total porosity, and weight concentrations of calcite, illite and quartz in the identified geologic facies. The highly variable vertical distribution of the petrophysical and compositional properties in each geologic facies is indicative of the significant vertical heterogeneity in the formation.

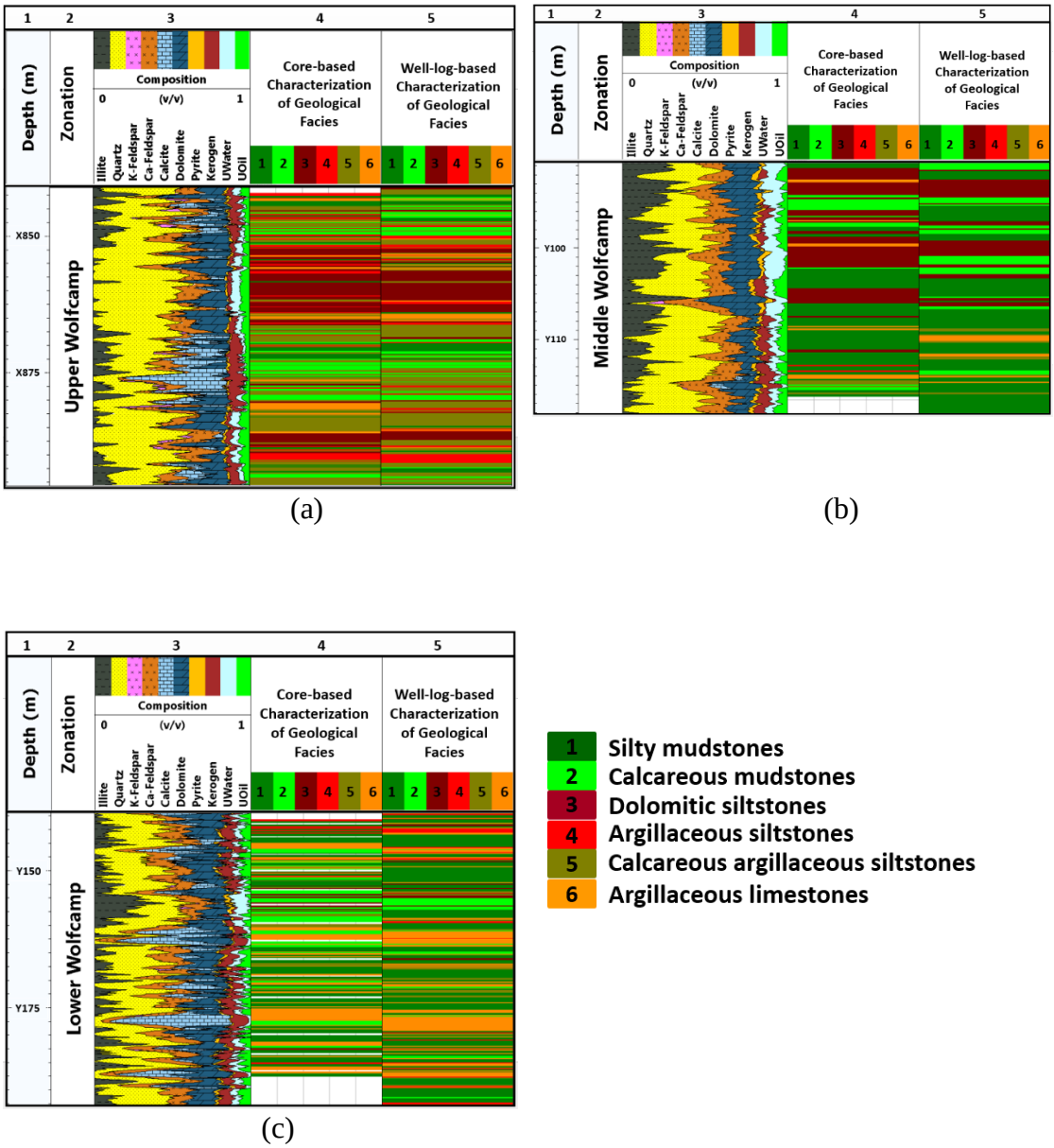

Fig. 2.15—Wolfcamp formation: (a) upper (b) middle, and (c) lower Wolfcamp intervals. Tracks from left to right include, Track 1: depth; Track 2: zonation; Track 3: estimates of volumetric concentrations of minerals; Tracks 4: core-based characterization of geological facies; Track 5: well-log-based characterization of geological facies.

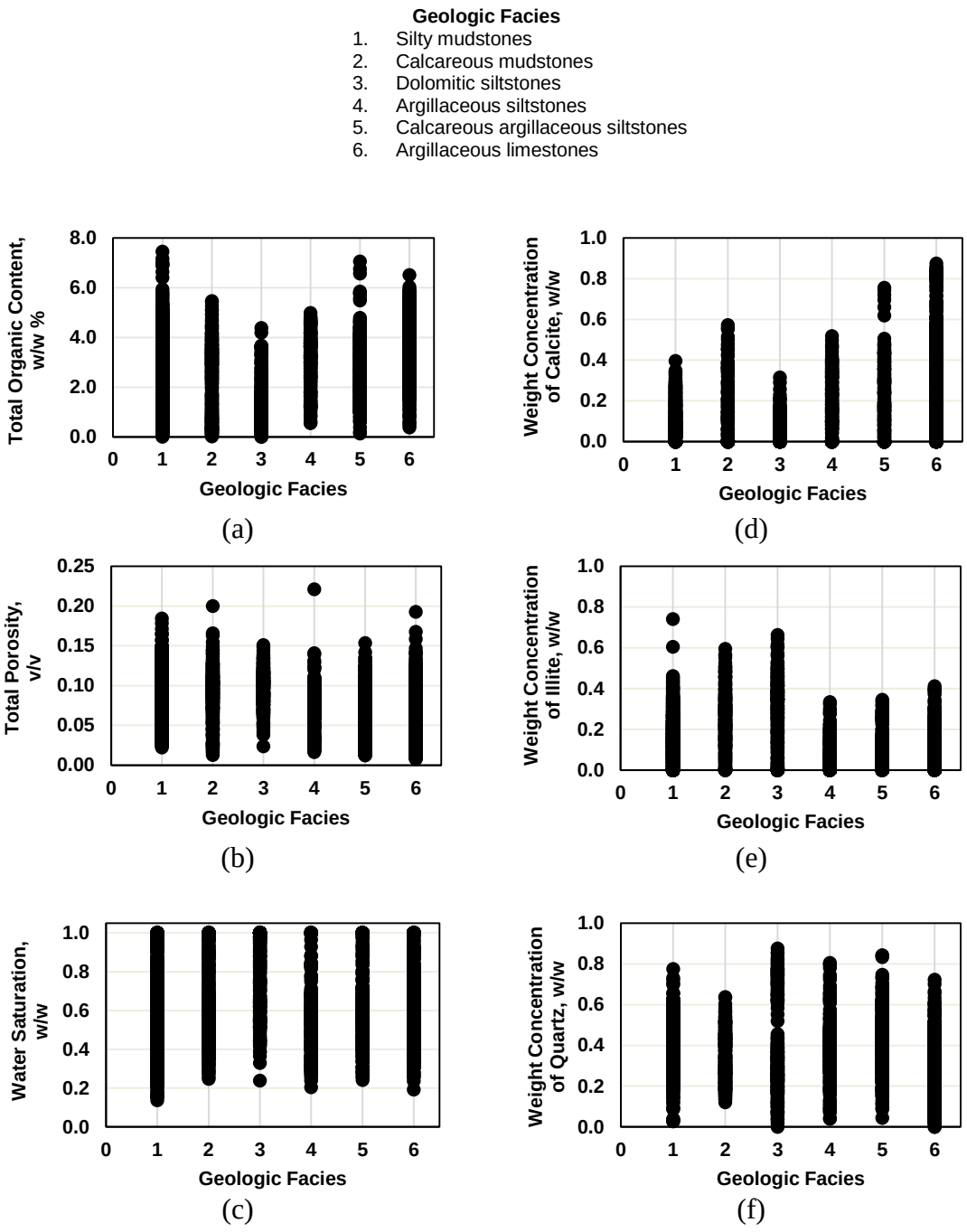

Fig. 2.16—The distribution of estimated petrophysical and compositional properties: (a) TOC (b) total porosity, (c) water saturation, (d) weight concentration of calcite, (e) weight concentration of illite, and (f) weight concentration of quartz in the six geologic facies identified in the Wolfcamp formation.

Fig. 2.17 shows the result of the integrated rock classification in the Wolfcamp formation. Track 7 of Fig. 2.17 the core-based characterization of geologic facies. Track 8 of Fig. 2.17 shows the depth-by-depth well-log-based characterization of the geologic facies. Track 9 of Fig. 2.17 shows the RQ classifications (RQ1, RQ2, RQ3, and RQ4). **Table 2.4** summarizes the petrophysical and compositional properties for each rock class based on RQ. Organic richness is a key factor in successful production from organic-rich mudrocks. The porosity variation was indeed not significant in different rock types and not a strong contributor to rock quality identification. I observed that TOC has a stronger correlation (about 67%) with the rock classes based on RQ, compared to the other input properties (i.e., porosity and water saturation) which have a correlation of about 62% with the rock classes based on RQ. A good agreement was observed between the rock classes based on RQ (Track 9 of Fig. 2.17) and the well-log-based characterization of the geologic facies (Track 8 of Fig. 2.17).

Table 2.4—Petrophysical and formation properties of the four rock classes based on reservoir quality (RQ) in the Wolfcamp formation.

Reservoir (RQ) Rock Class	TOC (wt.%)	Total Porosity (V/V)	Water Saturation
RQ1	3.56±0.48	0.10	0.40±0.01
RQ2	3.43±0.50	0.05	0.69±0.04
RQ3	1.85±0.69	0.09	0.64±0.01
RQ4	0.82±0.07	0.09	0.95±0.01

Track 10 of Fig. 2.17 shows the four SP zones, SP1, SP2, SP3, and SP4, identified in the Wolfcamp formation. **Table 2.5** summarizes the average stress gradients for each rock class, obtained by averaging the estimated minimum horizontal stress gradient within each rock class. Track 10 of Fig. 2.17 illustrates the estimates of the minimum horizontal stress gradient overlain by the average stress gradient. The upper Wolfcamp depth interval have the lower average stress gradients. Some intervals in the middle and the lower Wolfcamp formation experiences higher average stress gradients.

Table 2.5—Average minimum horizontal stress gradient of the four rock classes based on stress profile (SP) in the Wolfcamp formation.

Stress Profile (SP) Rock Class	Average Minimum Horizontal Stress Gradient, MPa/km
SP1	13.0
SP2	14.0
SP3	15.5
SP4	17.5

Track 11 of Fig. 2.17 shows the four CQ classifications (CQ1, CQ2, CQ3, and CQ4). **Table 2.6** summarizes the recommendations for each CQ rock class. The rock class CQ1 is the suggested candidate for fracture initiation because it is characterized by a combination of high RQ, and low stress gradient. The rock class CQ4 is recommended for fracture containment because they are characterized by a combination of high stress gradient, and low RQ. The selection of the rock classes CQ2 and CQ3 for completions will depend on the properties of the zones above and below these rock classes. Other

factors such as production data, where available, and overall cost of the hydraulic fracture treatment designs, are also key contributors to the selection of completions target zones.

Table 2.6—Attributes of the completion quality (CQ) classification.

Completion Quality (CQ) Rock Class	Considerations for completion design
CQ1	Intervals characterized with a combination of high RQ and low average stress gradient. Good candidate for fracture initiation and propagation, with expected productivity.
CQ2	Intervals characterized with low RQ and low average stress gradient. Potential candidate for fracture initiation and propagation, if located close to intervals with high RQ.
CQ3	Intervals characterized with high RQ and high average stress gradient. Potential candidate for fracture containment.
CQ4	Intervals characterized with low RQ and high average stress gradient. Good candidate for fracture containment.

There can be uncertainties in assessment of stress gradient due to the assumption made for the calculations and the inevitable uncertainty in measurements. To investigate the impact of such possible uncertainties in stress gradient estimates on the rock classification results, 5% random Gaussian noise was added to the well-log-based estimates of stress gradient. I then applied SP and CQ rock classification using the data with additional synthetic uncertainty. The implemented 5% noise had no impact on the SP and CQ rock classification results.

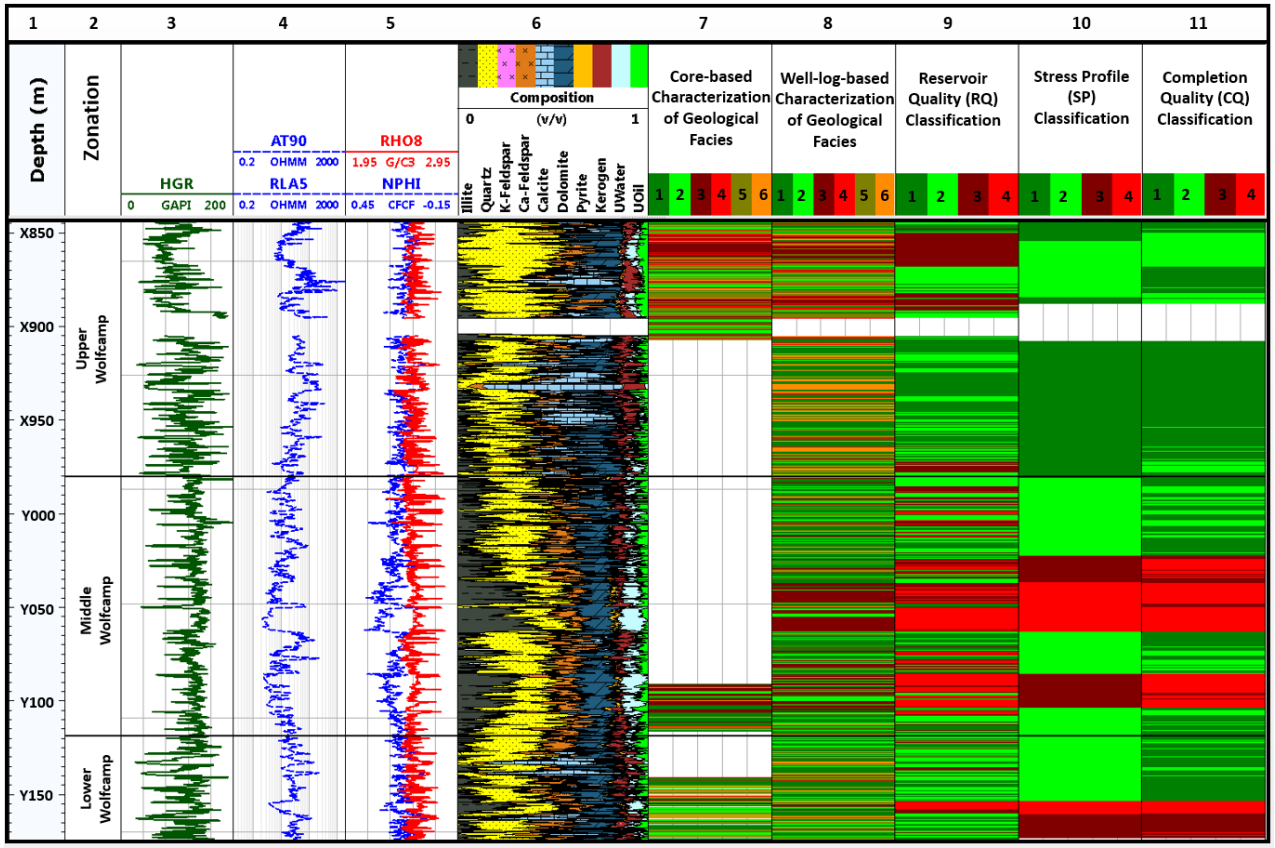

Fig. 2.17—Wolfcamp formation: Rock classification results. Tracks from left to right include, Track 1: depth; Track 2: zonation; Tracks 3-5: gamma ray, apparent resistivity logs, and neutron porosity/bulk density; Track 6: estimates of volumetric concentrations of minerals; Tracks 7: core-based characterization of geologic facies; Track 8: well-log-based characterization of geologic facies; Track 9: reservoir quality (RQ) classes; Track 10: stress profile (SP) represented by the minimum horizontal stress gradients and average stress gradient; Track 11: completion quality (CQ) classes with integrated reservoir quality and stress gradient properties for completions design.

2.4 Conclusions

I introduced an integrated rock classification technique that takes into account SP in the formation as well as RQ for selecting the best zones for completion. The introduced rock classification method is designed based on four classification schemes including (a) geologic facies, (b) RQ, (c) SP, and (d) CQ. I applied the introduced technique to a well from the Wolfcamp formation. The geologic attributes of the formation, petrophysical and geomechanical properties, estimated from well logs, were used in the analysis for the four classification schemes. The results of the geologic facies classification demonstrates the high vertical heterogeneity of the formation, and showed good agreement with the rock classes based on RQ at most depth intervals. I evaluated the influence of the uncertainty associated with drilling fluid velocity, Stoneley slowness, and C_{66}, on the estimation of the minimum horizontal stress. The minimum horizontal stress gradient has a relative change of 9% and 3%, 5% and 11%, and 0.2% and 0.2%, in the presence of 2% variation in drilling fluid velocity, Stoneley slowness, and C_{66}, respectively. The resulting stress gradient indicated stress contrasts which are important for the identification of target zones for fracture initiation and containment.

Based on the quantified SP and RQ, I finally characterized the depth-by-depth CQ of the upper, middle, and lower Wolfcamp. I proposed that the interval in the middle of the upper Wolfcamp, which was characterized by high RQ, low stress gradient, and thickness of about 76 m (250 ft.), was ideal for initiation of fractures that will propagate through most of the upper Wolfcamp interval and the top of the middle Wolfcamp. I also proposed that the intervals in the center of the middle Wolfcamp, and bottom of the lower

Wolfcamp formations are ideal as barriers for fracture containment, because these intervals were characterized by contrasting high stress gradients and low RQ. The resulting recommendations for completions design from the proposed integrated rock classification can be justified using production data, if available. The production data can be further used to quantify the efficiency of the perforations and overall well productivity in the formation.

CHAPTER III

MECHANICAL DAMAGE CHARACTERIZATION IN PROPPANT PACKS USING ACOUSTIC MEASUREMENTS*

The strength and conductivity of proppant packs are key parameters for assessing their performance. Mechanical damage in the propping agents, leading to compaction and crushing, significantly reduces the conductivity of the proppant pack. Mechanical damage of proppants is usually analyzed using crush tests. However, measurements from these tests remain questionable because of discrepancies in procedures and test results. Therefore a need emerges to develop techniques for characterizing the properties and mechanical damage in proppant packs.

In this chapter, I introduced a new technique based on interpretation of acoustic measurements using a granular effective media model, to quantify mechanical damage in propping agents. I performed uniaxial compression tests in the laboratory and measured the compressional- and shear-wave velocities in proppant packs loaded at axial stress ranging from 10 MPa to 110 MPa. After unloading the tests in which maximum axial stress of 28, 55, 69, 97 and 110 MPa were applied, I conducted sieve analysis on the proppant packs. An effective medium theory based on the Hertz-Mindlin granular contact model was applied to approximate the effective elastic properties. I then calibrated the

*Part of this chapter is reprinted with permission from "Mechanical Damage Characterization in Proppant Packs Using Acoustic Measurements" by Aderibigbe A.A, Chen Valdes, C., Heidari, Z., and Fuss, T. Paper IPTC-18092-MS presented at the International Petroleum Technology Conference, Kuala Lumpur, Malaysia, 10–12 December. Copyright 2014 by the Society of Petroleum Engineers.

model using the elastic properties estimated from the experimental measurements to characterize the mechanical damage of the proppant packs.

I observed that the increase in grain-to-grain contact, as the axial stress increases, results in compaction and crushing in the proppant pack. The compaction, elastic and plastic behavior in the stress-strain profile of the proppant pack were in agreement with the analysis of fines generated at different stress levels. The combined effect of compaction and crushing resulted in a reduction of porosity, and consequently decrease in the compressional- and shear-wave velocities of the proppant pack. The Hertz-Mindlin model showed a good approximation of the effective elastic properties estimated from the acoustic-wave velocities when calibrated with the pressure-dependent grain contact and the fraction of non-slipping grains as parameters. I demonstrated that the calibrated parameters can be correlated with the mechanical damage in the proppant pack The characterization of mechanical damage in proppant packs can improve design of the propping agents and quantification of proppant performance. Furthermore, the laboratory procedure can be extended to the use of borehole acoustic measurements in providing a real-time in-situ assessment of proppant performance.

3.1 Introduction

Proppants are used to create conductive pathways for reservoir fluids by keeping the fractures open during hydraulic fracture stimulation treatments. The application of proppants in stimulation treatments is largely influenced by properties such as permeability, conductivity, and resistance to crush. The reduction in fracture conductivity

is usually associated with proppant failure and fines migration. The failure of proppants can occur as a result of geochemical reactions and/or mechanical damage under downhole conditions. Raysoni and Weaver (2012) studied the effect of chemical reactions between proppants and the formation, and showed that geochemical reactions can cause loss of permeability and deterioration of proppant strength.

Mechanical damage of proppants is analyzed using the American Petroleum Institute (API) standardized crush test (API RP-56, 1983). The crush testing procedure was originally established to provide guidelines on procedures and equipment used in testing and evaluating sand used in hydraulic fracturing operations. This procedure was superseded by the API RP-19C procedure which specifically describes the testing procedures for evaluating proppants used in in hydraulic fracturing and gravel-packing operations (API RP-19C, 2008). Several authors documented their studies on the crush test (Raysoni and Weaver, 2012; Stephens et al., 2006). Some of the studies (Palisch et al., 2010; Getty and Bulau, 2014; Liang et al., 2015) addressed the efficiency and shortcomings of these procedures. The arguments and discrepancies highlighted by these studies indicate that there is still room for improving the technology in studying the mechanical damage in proppant packs.

Brannon (2013) in his patent, demonstrated the use of a modified API/ISO proppant crush test to measure the acoustic behavior of various proppant materials during stress application. The test results showed that certain materials, such as glass beads and ceramic proppants, can cause detectable sound emissions with applied stress. Simo (2013) also proposed a new proppant crush test approach to determine the failure stress of

proppants, and quantified the changes in failure stress for varying concentrations of different types of proppants.

Mechanical damage that leads to compaction and crushing is studied for sands by measuring ultrasonic velocities. Biot (1962) reformulated his previously established theory of propagation of elastic waves to unify the relationship between the mechanics of deformation and the propagation of acoustic waves in saturated porous media. Wyllie et al. (1958) also showed that pressure and porosity strongly influence velocity in consolidated sand and unconsolidated aggregates. Fortin et al. (2007) carried out ultrasonic measurements on sandstone samples under hydrostatic loading to measure the variations in compressional- and shear-wave velocities, and how these velocites were affected by cracking and reduction in porosity. Fawad et al. (2011) also studied the changes in porosities and ultrasonic velocities with increasing stress for dry sand aggregates using uniaxial mechanical compaction tests. Their work showed the effect of grain size, shape, sorting and mineralogy on the variations in porosities and velocities of the sand aggregates.

Elastic properties can be estimated from compressional- and shear-wave velocities calculated from acoustic measurements. The elastic properties of unconsolidated sands are usually studied using the effective medium models for granular media (Avseth and Bachrach, 2005; Dutta et al., 2010). Effective medium theory approaches such as Hertz-Mindlin model (Mindlin, 1949) is often used to derive the effective elastic moduli of packings of identical and spherical granular materials. This model combines the Hertzian contact model, which is used to estimate the normal (compressional) stiffness for two

identical spheres, and the Mindlin contact model which is used to estimate the tangential (shear) stiffness of the spheres (Deng et al., 2011; Mavko et al., 2009).

Zimmer (2003) investigated the relationship between the ratio of compressional- to shear-wave velocities and pressure as a result of pre-consolidation and sorting in unconsolidated sands. This work showed that the Hertz-Mindlin model overestimated the shear moduli and underestimated the pressure dependence of the moduli and velocities of the unconsolidated sands, when compared to experimental data from ultrasonic measurements. The discrepancy was attributed to the inability of the model to account for rotation of grains and slip at their boundaries. Zimmer (2003) applied a modified Hertz-Mindlin model which assumes that there is no friction between the grains (hence the tangential stiffness is negligible). The result obtained was a reasonable match between the model and experimental results. A similar study on unconsolidated beach sand carried out by Bachrach et al. (2000) also showed differences of the actual values of velocities and Poisson's ratio estimated from the Hertz-Mindlin model with experimental data from seismic measurements. The differences observed in their study were attributed to the angularity of the sand grains and the assumption of no slip at the grain contacts. These differences were modified by introducing an average angularity parameter and assuming slip at the grain contacts.

Previous publications documented applications of effective medium models for assessment of elastic properties in rocks and unconsolidated sands. However, effective medium models have not been applied in the assessment of elastic properties of proppant packs. Kurz et al. (2013) used stress-strain analysis to determine the elastic properties of

proppant packs. They compared the stiffness exhibited by testing Ottawa sand, resin-coated sand, and lightweight ceramic proppant. In this chapter, I applied Hertz-Mindlin effective medium model to investigate the elastic properties of proppant packs, with the aim of correlating these elastic properties to mechanical damage in the proppants. The conventional standard crush test (API RP19C, 2008) is conducted mainly to obtain the percentage of crush at certain pressures. This test does not allow the investigation of proppant behavior over a wide range of pressure variation. The use of acoustic measurements to characterize proppants under uniaxial compression enables quantification of the effects of proppant behavior such as compaction, crushing, and change in porosity, over a range of pressure. This technique also enables the estimation of mechanical properties such as the elastic moduli of the proppant pack. The assessment of proppant behavior and mechanical properties is pertinent to understanding proppant pack conductivity, and improving the selection of proppants in hydraulic fracturing treatment design.

The objectives of this chapter include (a) to study experimentally the mechanical damage of proppants by conducting uniaxial compression tests, (b) to investigate variation in porosity and the sensitivity of acoustic measurements to both compaction and crushing in proppant pack, (c) to apply the Hertz-Mindlin model to estimate the effective elastic properties of proppant packs, and (d) to quantify mechanical damage in proppant packs using interpretation of the acoustic measurements and the Hertz-Mindlin model. The following sections describe the method, the results from the laboratory experiments and analytical model, and the conclusions.

3.2 Method

The introduced workflow included both experimental and analytical methods. For the experiments, I designed and carried out uniaxial compression tests for proppant packs. After unloading the samples from the compression tests, I carried out sieve analysis to measure the crush percentage in the proppant pack. In the analytical method, the Hertz Mindlin model was used to estimate the effective elastic properties of the proppant pack. I then compared the model to experimental data and introduced pressure-dependent calibration parameters to obtain a good agreement of the model to the experimental data. The proppants used in the experiments were bauxite-based intermediate density proppants, sieved and sized to 20/40 ASTM mesh. Other properties of the proppants are listed in **Table 3.1**.

Table 3.1—Properties of proppants.

	Value	Unit
Roundness / Sphericity	0.90	-
Bulk density	1.88	g/cc
Specific gravity	3.20	-

3.2.1 Experimental method

3.2.1.1 Ultrasonic tests

I carried out uniaxial compression tests to investigate the sensitivity of acoustic measurements to mechanical damage in proppants. The uniaxial compression tests was conducted on different sets of samples of the same type of proppant. I placed a stainless

steel cylindrical sample holder with an internal diameter of 2.54 cm between loading platens which have a built-in pair of ultrasonic transducers. **Fig. 3.1** illustrates the assembly of the ultrasonic transducers and the proppant sample holder. The ultrasonic transducers enabled measurement of compressional- and shear-wave velocities using the pulse transmission technique. For each test, I weighed 15 g of proppant, and placed it in the sample holder. I gently tapped the proppants to obtain a flat surface at the top of the proppant pack. The proppant loading corresponds to an areal concentration of about 3 g/cm^2 (6 lb/ft^2). The same procedure and consistency was applied for sample preparation in all the cases to ensure consistent initial porosity of the proppant pack. I assumed a dense random pack arrangement of proppant grains. The initial porosity was calculated from the difference of proppant volume and the total volume occupied in the container.

A square-wave pulser-receiver was used to excite the acoustic transducer source with a pulse that propagates through the proppant pack to the receiver transducer. I monitored the waveform and amplitudes using a digital oscilloscope, and then exported and recorded them for signal processing to obtain the travel time of the compressional- and shear-waves. **Fig. 3.2** shows the digital oscilloscope and the square-wave pulser-receiver used in the experiments.

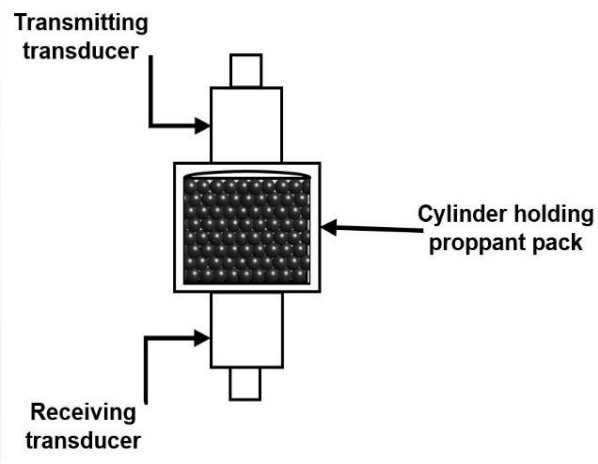

Fig. 3.1—Transmitting and receiving transducers for ultrasonic measurements of the proppant pack during the uniaxial compression tests.

Fig. 3.2— Experimental set-up showing the digital oscilloscope on the left, and the square wave pulser-receiver on the right.

Fig. 3.3 shows the assembly of the ultrasonic transducers and the proppant sample holder placed into a triaxial rock testing system. An incremental axial stress was applied to the proppant pack along the vertical axis at a constant stress rate of 13.8 MPa/min (2000 psi/min) till maximum stress of 28, 55, 69, 97 and 110 MPa was reached for each test. In

the experimental setup, uniaxial strain conditions were assumed since the lateral deformations were constrained by the stainless steel cylinder. I measured the deformation caused by mechanical loading of the proppant pack using two-linear variable differential transformers (LVDT), to quantify the axial strains at different stress levels. The axial strains were then used in estimating the change in porosity of the proppant pack.

I made initial reference measurements of the first wave arrival time by placing the ultrasonic transducer platens in a head-to-head configuration. The reference measurements were subtracted from the first arrival time for each test. I then calculated the compressional- and shear-wave velocities via

$$V_p = \frac{h_{prop}}{\Delta t_p} \tag{3.1}$$

and

$$V_s = \frac{h_{prop}}{\Delta t_s}, \tag{3.2}$$

where V_p and V_s are the compressional- and shear-wave velocities, respectively, h_{prop} is the height of the proppant pack at different stress increments, and Δt_p and Δt_s are the travel times of the compressional- and shear-wave velocities, respectively.

Fig. 3.3—Experimental set-up for the triaxial rock testing system used for the uniaxial compression test, with inset showing ultrasonic sensors and stainless steel cylinder holding the proppants.

For homogenous and elastic materials, the dynamic bulk and shear moduli were estimated from the compressional- and shear-wave velocities as

$$k_d = \rho\left(V_p^{\,2} - \frac{4}{3}V_s^{\,2}\right) \tag{3.3}$$

and

$$\mu_d = \rho V_s^{\,2}, \tag{3.4}$$

where k_d and μ_d are the dynamic bulk and shear moduli, respectively, and ρ is the dry bulk density of the proppant pack. The dry bulk density of the proppant pack was estimated via (Das, 1941)

$$\rho = G_s\left(1-\phi\right), \tag{3.5}$$

where G_s is the specific gravity of proppant grains and ϕ is the porosity of the proppant pack.

3.2.1.2 Sieve analysis

After completing the mechanical tests at different maximum stress (i.e., 28, 55, 69, 97 and 110 MPa), I conducted sieve analysis for each proppant pack. US standard sieves with sieve numbers 16 (1.18 mm), 30 (0.60 mm), 50 (0.30 mm), 100 (0.15 mm), 170 (0.09 mm), and 230 (0.06 mm), were stacked in a mechanical sieve shaker as shown in **Fig. 3.4**. The sieves with the larger openings (i.e., with lower sieve numbers) were placed above the ones having smaller opening sizes (i.e., higher sieve numbers), and the pan was placed at the bottom of the stack. I carefully transferred the content (i.e., proppants) from the cylindrical test cell into the sieve stack. The mechanical sieve shaker was then run for 10 minutes to ensure the separation of the crushed proppants. After the separation, I removed

the sieve stack from the shaker, and weighed all the contents retained on each sieve. The procedure was repeated twice for proppant packs loaded to each maximum stress. I calculated the weight percent of crushed proppants based on the weight of proppant material that is smaller than the specified range of the proppant size (i.e., 40 mesh size).

Fig. 3.4—Mechanical sieve used for sieve analysis of proppant pack after the uniaxial compression test.

3.2.2 Analytical method

3.2.2.1 Theoretical basis for the Hertz-Mindlin effective medium model

Effective medium theory based on the Hertz-Mindlin granular contact model can be applied to predict the average effective elastic properties of a granular pack of spheres. In a two-particle system where two identical spheres are in contact, the force existing between the spheres over the contact area can be decomposed into two force components.

The two force components are the normal contact force, F_n, and the tangential contact force, F_t. **Fig. 3.5** shows a schematic of normal and tangential displacement acting on the contact area of a two-particle system. R is the sphere radius, while δ and τ are the displacements along the unit vectors normal and tangential to the contact area, respectively.

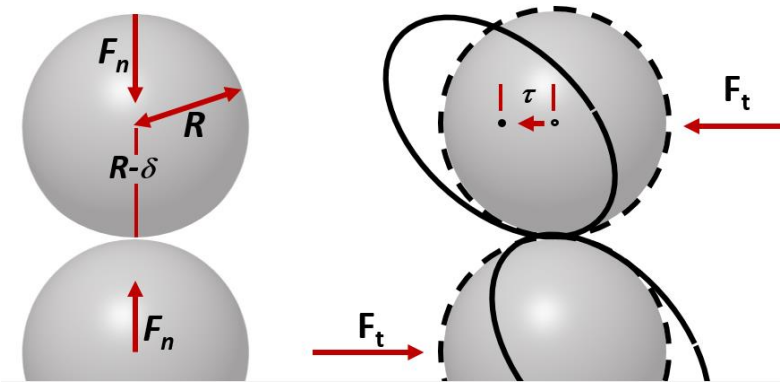

Fig. 3.5—Normal and tangential displacement acting on the contact area of a two-particle system (Modified from Mavko et al., 2009).

The relationship between the force components and the displacements are given as (Norris and Johnson, 1997)

$$\partial F_n = S_n \partial \delta, \tag{3.6}$$

and

$$\partial F_t = S_t \partial \tau, \tag{3.7}$$

where S_n and S_t are the normal and tangential stiffness values, respectively.

The effective bulk moduli, K_{eff}, and shear moduli, μ_{eff}, of a granular pack of spheres can be expressed in terms of the normal and tangential stiffness (Winkler, 1983) via

$$K_{eff} = \frac{C(1-\phi)}{12\pi R} S_n, \tag{3.8}$$

and

$$\mu_{eff} = \frac{C(1-\phi)}{20\pi R}\left(S_n + \frac{3}{2} S_t \right), \tag{3.9}$$

where C is the coordination number (average number of contacts per sphere) and ϕ is the porosity of the spheres pack. The coordination number, C, is often expressed as a function of porosity using empirical correlations such as the Murphy (1982) relation (Zimmer, 2003), given by

$$C = 24\exp(-2.557\phi) - 0.37 . \tag{3.10}$$

In the Hertz contact model, the radius of contact area, a_n, between two identical spheres is given as

$$a_n = \left[\frac{3F_n R}{8\mu}(1-\nu) \right]^{1/3}, \tag{3.11}$$

where μ and ν are the shear modulus and Poisson ratio of the grain material, respectively. If an effective pressure, P, is applied to a granular pack of spheres, the normal confining force between the two spheres is given by

$$F_n = \frac{4\pi R^2 P}{C(1-\phi)}. \tag{3.12}$$

Hence, substituting Equation 3.12 into Equation 3.11, leads to

$$a_n = R\left[\frac{3\pi(1-\nu)}{2C(1-\phi)}P\right]^{1/3}. \tag{3.13}$$

Mindlin (1949) showed that slip may occur at the contact surface if the spheres are first pressed together, and afterwards tangential force is applied. Hence, the contact stiffnesses (i.e., S_n and S_t), which depend on geometric and material properties of the spherical grains were given by

$$S_n = \frac{4a_n\mu}{1-\nu} \tag{3.14}$$

and

$$S_t = \frac{8a_t\mu}{2-\nu}, \tag{3.15}$$

where a_t can be interpreted as the radius of the frictionally locked region of contact (Dutta et al., 2010; Saul et al., 2013).

Therefore, substituting Equations 3.14 and 3.15 into Equations 3.8 and 3.9, for the Hertz-Mindlin (HM) model, the effective bulk modulus, K_{HM}, of a dry, random, identical-sphere packing is given by (Winkler, 1983; Mavko et al., 2009)

$$K_{HM} = \left[\frac{C^2 (1-\phi_o)^2 \mu^2}{18\pi^2 (1-\nu)^2} P \right]^{1/3}, \tag{3.16}$$

while the effective shear modulus, μ_{HM}, of a dry, random, identical-sphere packing is given by

$$\mu_{HM} = \frac{5-4\nu}{5(2-\nu)} \left[\frac{3C^2 (1-\phi_o)^2 \mu^2}{2\pi^2 (1-\nu)^2} P \right]^{1/3}. \tag{3.17}$$

The Hertz-Mindlin model originally assumes that there is friction between the grains, hence no slip occurs. If the spheres are assumed to be frictionless (i.e., slip occurs), tangential stiffness is negligible and the shear modulus is only dependent on the normal stiffness. In this condition, Equation 3.16 remains the same, while Equation 3.17 can be written as (Zimmer, 2003; Mavko et al., 2009)

$$\mu_{HM} = \frac{3K_{HM}}{5}. \tag{3.18}$$

If only a fraction of the grains have perfect adhesion (i.e., no slip occurs) and the remaining fraction is frictionless, then Equation 3.17 can be expressed as (Bachrach and Avseth, 2008; Mavko et al., 2009)

$$\mu_{HM} = \frac{2+3f_t - \nu(1+3f_t)}{5(2-\nu)} \left[\frac{3C^2 (1-\phi)^2 \mu^2}{2\pi^2 (1-\nu)^2} P \right]^{1/3}, \tag{3.19}$$

where f_t is the fraction of grain contacts having no slip because friction occurs (tangential stiffness is not negligible), while the fraction (1-f_t) have no friction at grain contacts (zero tangential stiffness).

I computed the dynamic bulk and shear moduli for the experimental data using Equations 3.3 and 3.4. I then estimated the different values of parameter C in Equation 3.16, by applying the least squares method (Stigler, 1981), to minimize the difference between the bulk moduli from the experimental data and the effective bulk moduli estimated from the Hertz-Mindlin model. I applied a constraint of $C \leq 12$ to the method, because a hexagonal close pack has the highest possible coordination number, C, of 12 (Mavko et al., 2009; Dutta et al., 2010). Similarly, I applied the least squares method to estimate the different values of parameter f_t in Equation 3.19, such that the shear moduli estimated from the Hertz Mindlin model was in good agreement with the experimental data. I then investigated how the parameters C and f_t varies with the effective pressure (i.e., the applied axial stress), porosity, and compressional velocity. I also investigated the correlation between the weight percentage of crushed proppants, W_c, determined from the sieve analysis, the coordination number, C, and the fraction of grain contacts with friction, f_t.

3.2.2.2 Estimation of grain elastic moduli

The shear modulus, μ, and Poisson ratio, ν, of the grain material are input parameters required in the estimation of the effective bulk and shear moduli using the Hertz-Mindlin model. I estimated the elastic moduli (i.e., the shear and bulk moduli) of

the proppant material from the mineral composition of the proppants using the Voigt-Reuss-Hill (VRH) average and the Hashin-Shtrikman-Walpole (HSW) bounds. I then calculated the Poisson's ratio of the proppant material using the shear modulus and bulk modulus, *K*, via

$$\nu = \frac{(3K - 2\mu)}{2(3K + \mu)}, \tag{3.20}$$

The VRH (Hill, 1952) average was used to obtain the initial estimate of the elastic moduli of the proppant material using Equations 2.32 through 2.34.

The HSW bounds (Hashin and Shtrikman, 1963; Walpole, 1966) were used to estimate the upper and lower limit values of the bulk and shear moduli of the proppants. HSW bounds give the narrowest possible range for an isotropic linear elastic composite. For cases where there are only two constituents, the bounds are given as

$$K^{HS\pm} = K_1 + \frac{f_2}{(K_2 - K_1)^{-1} + f_1\left(K_1 + \frac{4}{3}\mu_m\right)^{-1}}, \tag{3.21}$$

$$\mu^{HS\pm} = \mu_1 + \frac{f_2}{(\mu_2 - \mu_1)^{-1} + f_1\left[\mu_1 + \frac{\mu_m}{6}\left(\frac{9K_m + 8\mu_m}{K_m + 2\mu_m}\right)\right]^{-1}}, \tag{3.22}$$

where the properties of the two components are represented by the subscripts 1 and 2, K^{HS+} and K^{HS-} are the upper and lower bounds of the bulk moduli, respectively, μ^{HS+} and μ^{HS-} are the upper and lower bounds of the shear moduli, respectively, K_m and μ_m are the

maximum bulk and shear moduli for the upper bound, and for the lower bound, K_m and μ_m are the minimum bulk and shear moduli. For the case of the proppant material, which is a mixture of more than two components, the general form of the HSW bounds (Berryman, 1995; Mavko et al., 2009) given by was applied

$$K^{HS+} = \Lambda\left(\mu_{\max}\right), \tag{3.23}$$

$$K^{HS-} = \Lambda\left(\mu_{\min}\right), \tag{3.24}$$

$$\mu^{HS+} = \Gamma\left(\zeta\left(K_{\max}, \mu_{\max}\right)\right), \tag{3.25}$$

and

$$\mu^{HS-} = \Gamma\left(\zeta\left(K_{\min}, \mu_{\min}\right)\right), \tag{3.26}$$

where

$$\Lambda(z) = \left\langle \frac{1}{K(r) + \frac{4}{3}z} \right\rangle^{-1} - \frac{4}{3}z, \tag{3.27}$$

$$\Gamma(z) = \left\langle \frac{1}{\mu(r) + z} \right\rangle^{-1} - z, \tag{3.28}$$

and

$$\zeta(K,\mu) = \frac{\mu}{6}\left(\frac{9K+8\mu}{K+2\mu}\right), \tag{3.29}$$

where K_{min} and K_{max} are the minimum and maximum bulk moduli of the individual constituents, respectively, and μ_{min} and μ_{max} are the minimum and maximum bulk moduli of the individual constituents, respectively.

3.3 Results and Discussions

Fig. 3.6 shows the stress-strain relationship of the proppant pack during uniaxial compression where a maximum axial stress of 110 MPa was applied. I observed that as the axial stress increased, compaction occured, which caused an increase in stiffness. At high axial stress levels (i.e., about 70 MPa in this case), the deformation of the proppant pack transitioned from an elastic behavior to a plastic behavior. **Fig. 3.7** shows the weight percentage of crushed proppants estimated from the sieve analysis when maximum axial stresses of 28, 55, 69, 97 and 110 MPa were applied to the proppant pack. I compared the stress-strain behavior of the proppant packs against the results of the sieve analysis. I observed that there was no significant crushing when the axial stress was below 20 MPa. This observation can be explained by the compaction region shown in Fig. 3.6. At axial stress of above 70 MPa, the weight percentage of crushed proppants increased significantly. This observation can also be explained by the transition region where the deformation changed from the elastic to plastic behavior.

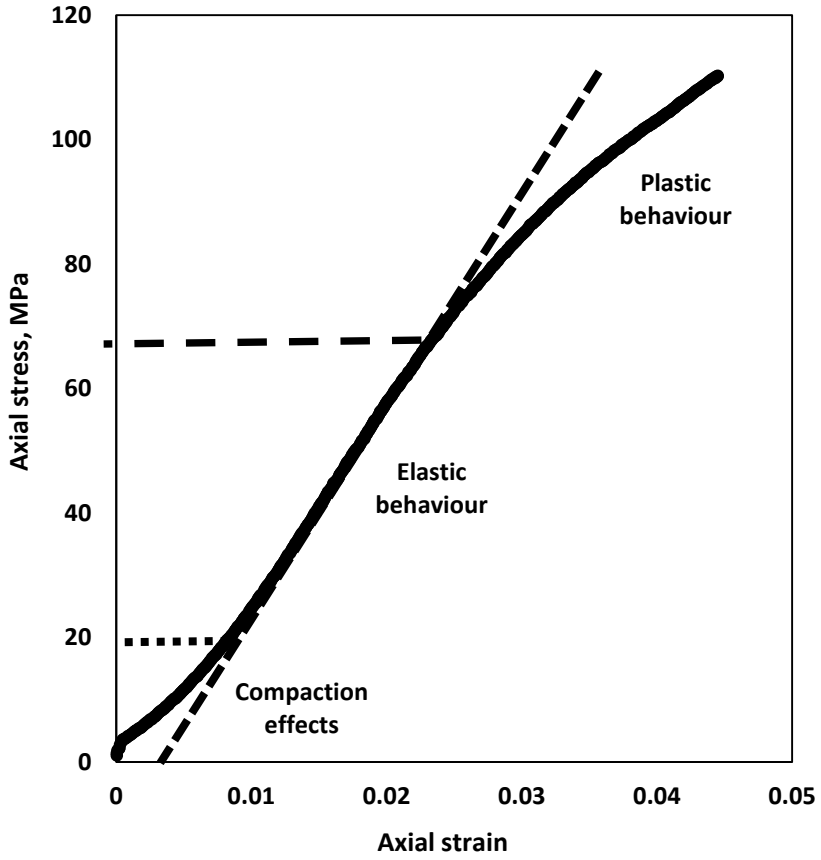

Fig. 3.6—Stress-strain relationship of proppant pack, under maximum axial stress of 110 MPa, and the regions where compaction, elastic and plastic behavior occurs. The black dotted line represents the stress limit below which compaction effect is dominant. The black dashed line represents the stress limit above which plastic behavior is dominant.

Fig. 3.8 shows the distribution of the percentage of fines passing through the selected sieves for each test where the proppants packs were loaded to maximum axial stresses of 28, 55, 69, 97 and 110 MPa. The effect of crush was first observed in the sieve number 30 (0.6 mm), which was the intermediate sieve size for the 20/40 proppants used in the experiment. As the applied axial stress increased, the amount of crushed proppants passing the sieve number 30 increased.

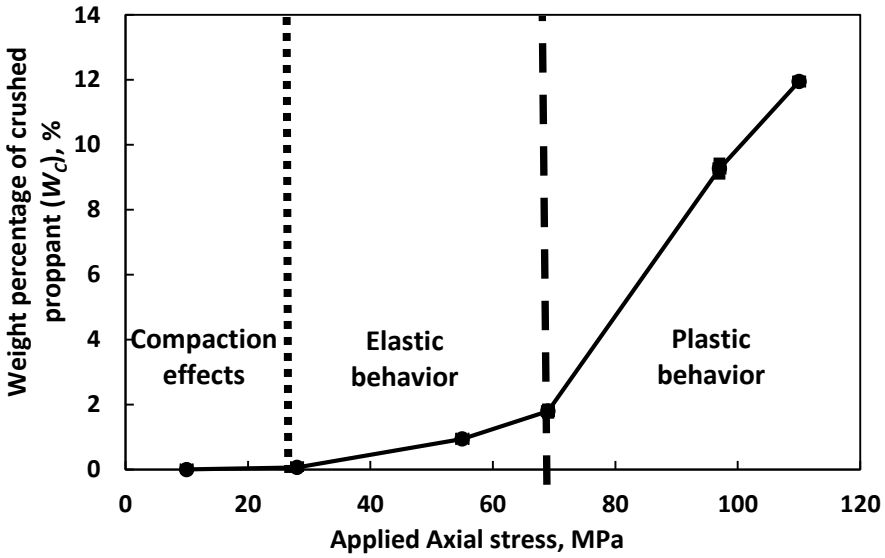

Fig. 3.7—The weight percentage of crushed proppants when maximum axial stresses of 28, 55, 69, 97 and 110 MPa are applied to the proppant packs. The weight percentage of crushed proppants increases significantly when the deformation in the proppant pack changes from the elastic to plastic behavior.

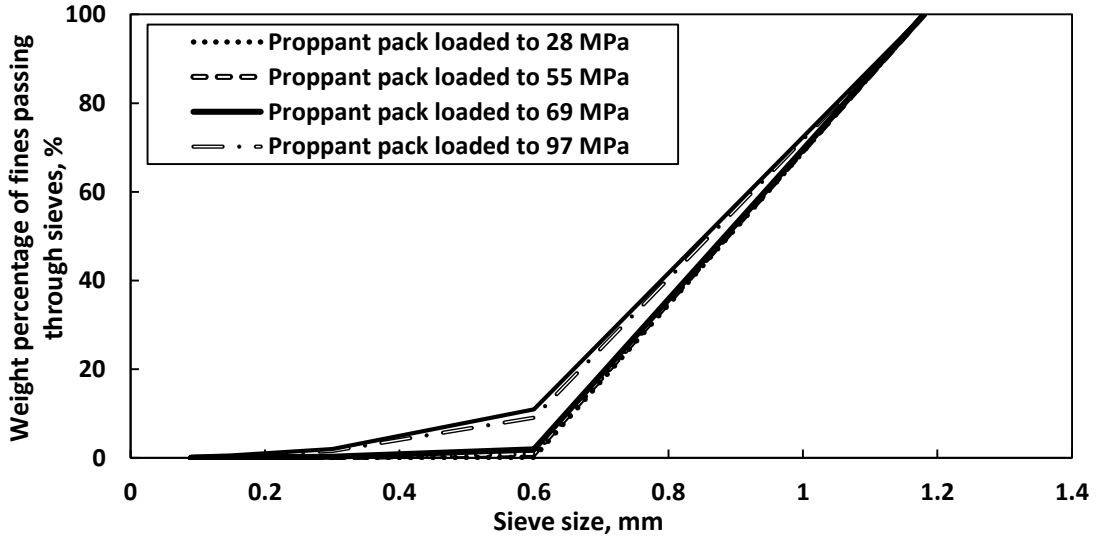

Fig. 3.8—Distribution of the percentage of fines passing through the selected sieves for each test. The increase in crush is first observed in the percentage of fines passing through sieve number 30 (0.6 mm).

Fig. 3.9 shows a comparison of the compressional- and shear-wave velocities in the proppant pack for uniaxial compression tests performed up to an axial stress of 110 MPa. I observed an increase in velocity as the axial stress increased. The initial increase in velocity can be attributed to the increment in the grain-to-grain contact area that occurs as a result of compaction of the proppant pack. As the axial stress further increased, the grain-to-grain contact caused deformation at the grain contacts which led to crushing.

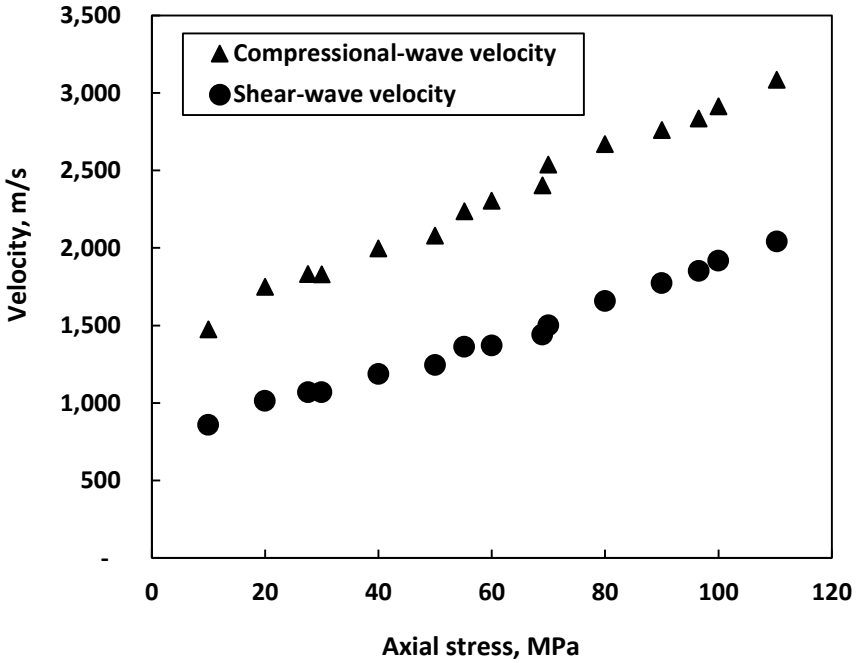

Fig. 3.9—Compressional- and shear-wave velocities of proppant packs during uniaxial compressional tests where maximum axial stress of 110 MPa was applied to the proppant packs. The increase in velocity as the axial stress occurs as a result of compaction and crushing of the proppant pack.

Fig. 3.10 shows the change in porosity as the axial stress increased. The initial porosity of the proppant pack was 37.5%. The porosity decreased from 37.5% to 34.8% due to the

increase in applied stress from 0 to 110 MPa. The combined effects of compaction and crushing in the proppant pack resulted in a reduction in porosity and consequently an increase in compressional- and shear-wave velocities through the proppant pack.

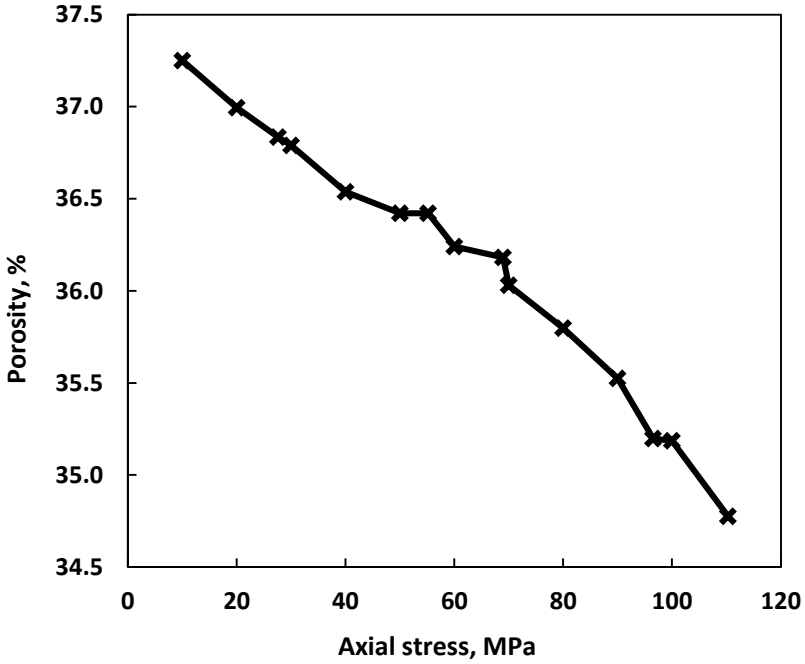

Fig. 3.10—Change in porosity of the proppant pack with increase in the applied axial stress during uniaxial compression test.

Figs. 3.11a, **3.11b** and **3.11c** show relationships between the coordination number, *C*, and the effective pressure, porosity, and compressional velocity respectively. The exponential correlations and the fitting parameters for *C*-effective pressure, *C*-porosity, and *C*-compressional velocity are shown in Equations 3.30 through 3.32.

$$C = x_1 e^{y_1 P}, \tag{3.30}$$

$$C = x_2 e^{y_2 \phi}, \tag{3.31}$$

and

$$C = x_3 e^{y_3 V_p}, \tag{3.32}$$

respectively, where x_1, y_1, x_2, y_2, x_3, and y_3 are fitting parameters. The fitting parameters were estimated using the least square regression analysis. In Fig. 3.11b, the *C*-porosity relation given by Murphy (1982) was also plotted for comparison against the correlation obtained from the fit of the experimental data. I observed that the new *C*-porosity relation correlation given by Equation 3.31 shows a better prediction of the coordination number than the Murphy (1982) correlation. The effective (axial) pressure is the only external force applied to the system. Hence, the effective bulk moduli were estimated assuming the exponential relationship between the coordination number and effective pressure. The correlation between the coordination number and porosity can introduce increased uncertainties because the porosity cannot be measured directly. **Fig. 3.12** shows a comparison of dry bulk moduli from the experimental data against the effective bulk moduli estimated using Hertz-Mindlin model, as a function of the applied axial stress.

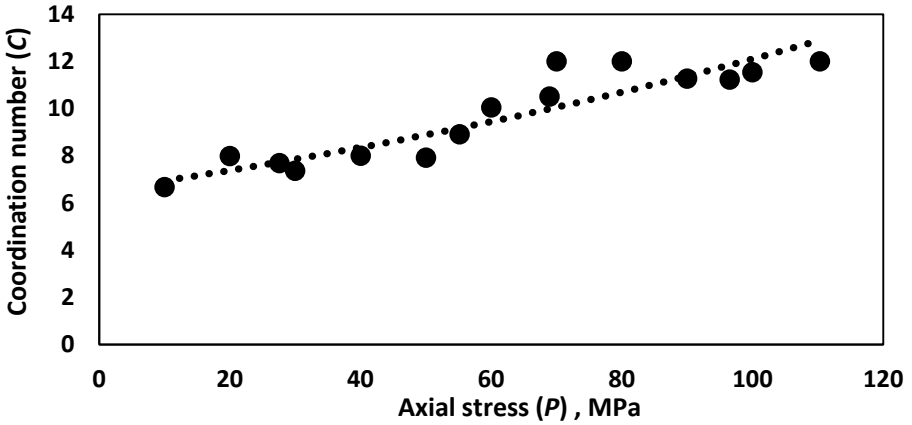

(a)

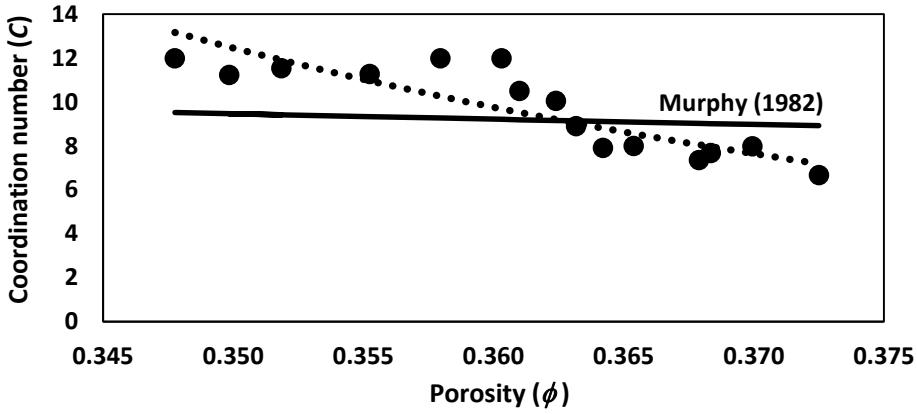

(b)

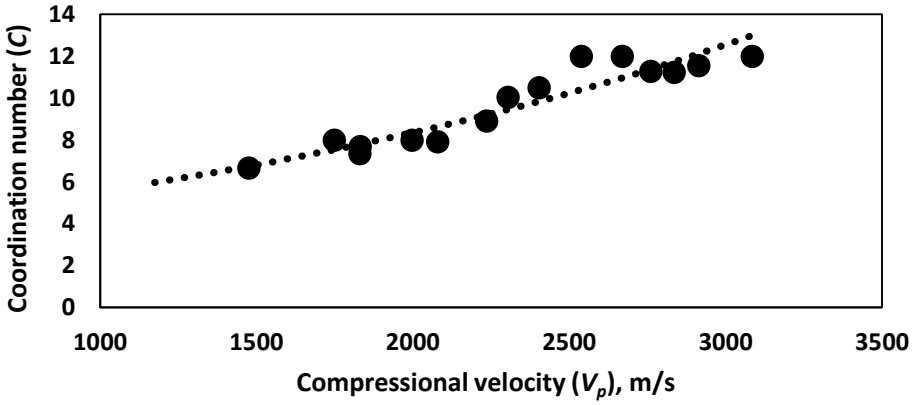

(c)

Fig. 3.11—Correlations between coordination number, *C*, and (a) effective pressure (i.e., the applied axial stress), (b) porosity, the black dotted lines demonstrates the contact numbers predicted by Murphy (1982) for the porosities of the samples, and (c) compressional velocity, of the proppant pack.

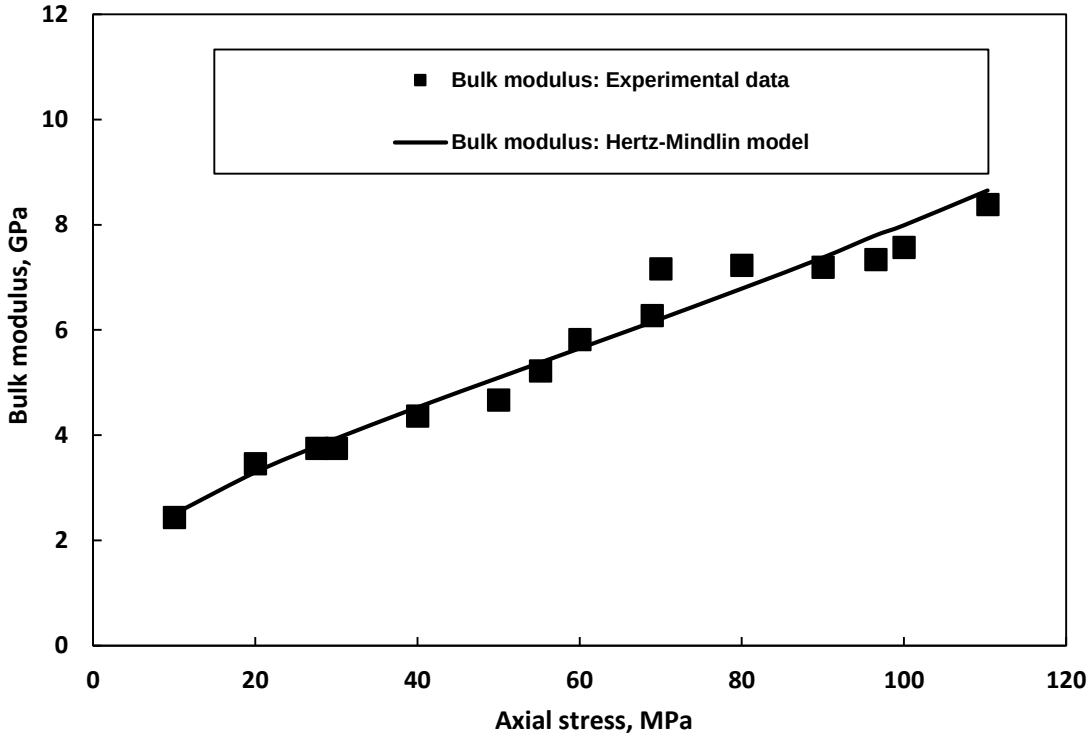

Fig. 3.12—Comparison of experimental and analytical (using Hertz-Mindlin model) estimates of bulk modulus.

The effective shear moduli were estimated using Equation 3.17, and also the coordination numbers calculated from Equation 3.30, at the corresponding applied axial stresses. **Fig. 3.13** shows a comparison of the dry shear moduli from the experimental data against the effective shear moduli estimated using the Hertz-Mindlin model, as a function of the applied axial stress. I observed that the Hertz-Mindlin model (shown by the dotted line in Fig. 3.13) overestimates the shear moduli when compared to the experimental data. This large discrepancy was due to the assumption of no slip (friction) throughout the grains.

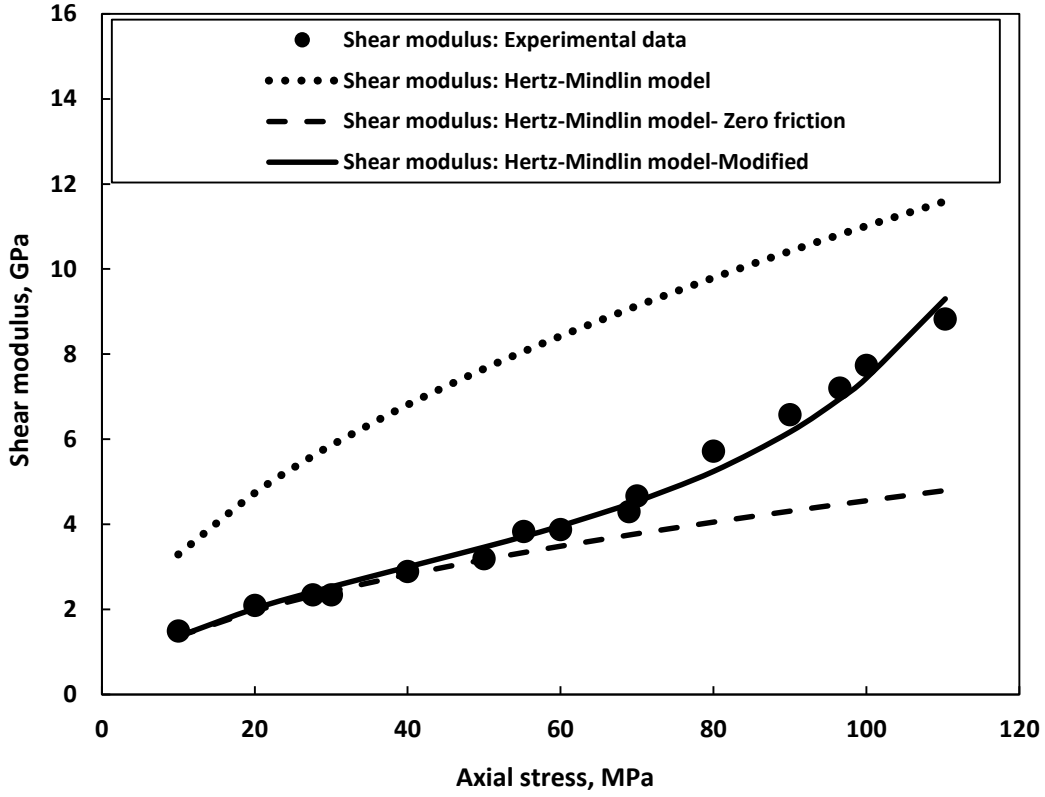

Fig. 3.13—Comparison of experimental and analytical (using Hertz-Mindlin models) estimates of shear modulus. The dotted, dashed, and solid lines represent estimates of shear modulus when no slip, slip, and a fraction of slip are assumed in the Hertz-Mindlin model, respectively.

I applied the Hertz-Mindlin zero friction model (Equation 3.18), in which all the grain contacts were assumed to be frictionless. I observed that the Hertz-Mindlin zero friction model (shown by the dashed line in Fig. 3.13) only shows good agreement with the experimental data at axial stresses below 50 MPa. At higher effective stress, the Hertz-Mindlin zero friction model underestimates the shear moduli. Hence, the assumption that all the grain contacts are frictionless was not valid. Therefore there is a need to account for the fraction of grain contacts with friction, f_t.

I used the shear moduli from the experimental data to fit the effective shear moduli estimated from the modified Hertz-Mindlin model in Equation 3.19, and obtained the different values of f_t at the corresponding axial stress. **Figs. 3.14a**, **3.14b** and **3.14c** show relationships between the fraction of grain contacts with friction, f_t, and the effective pressure, porosity, and compressional velocity respectively. The exponential correlations and the fitting parameters for f_t -effective pressure, f_t -porosity, and f_t -compressional velocity are shown in Equations 3.33 through 3.35.

$$f_t = a_1 e^{b_1 P}, \tag{3.33}$$

$$f_t = a_2 e^{b_2 \phi}, \tag{3.34}$$

and

$$f_t = a_3 e^{b_3 V_p}, \tag{3.35}$$

respectively, where a_1, b_1, a_2, b_2, a_3, and b_3 are fitting parameters. The fitting parameters were estimated using the least square regression analysis. The pressure-dependent parameter, f_t, from Equation 3.33 was used in estimating the effective shear moduli. The resulting modified Hertz-Mindlin model (shown by the solid line in Fig. 3.13) shows a good agreement with the shear moduli calculated from the experimental data.

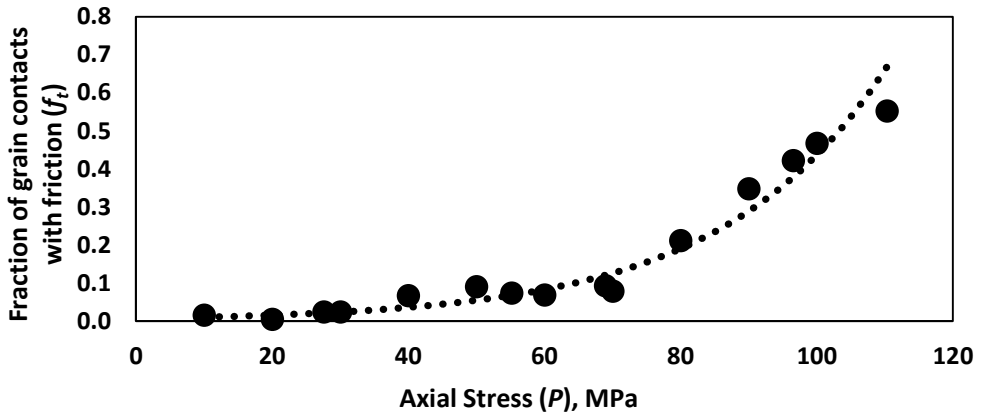

(a)

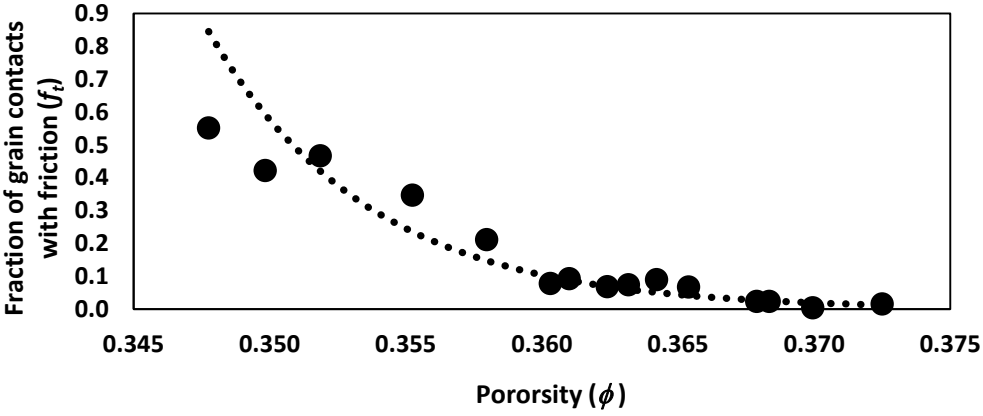

(b)

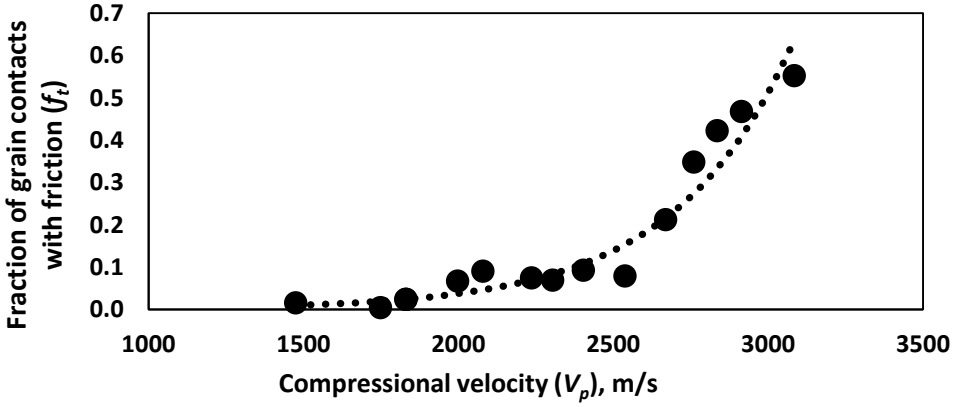

(c)

Fig. 3.14— Correlation between fractions of grain contacts with friction (no slip), f_t, and (a) effective pressure (i.e., the applied axial stress), (b) porosity, and (c) compressional velocity, of the proppant pack.

Fig. 3.15a shows a power-law relationship (Equation 3.36) between the weight percentage of crushed proppants, W_c, and the coordination number, C. The observed increase in the coordination number occured as the axial stress increased. The increase in axial stress resulted in the increase in the average number of contacts per each proppant particle. The resulting increase in grain-to-grain contact caused crushing at the grain contacts.

$$W_c = x_4 C^{y_4} \tag{3.36}$$

Fig. 3.15b shows a power-law relationship (Equation 3.37) between the weight percentage of crushed proppants, W_c, and the fraction of grain contacts with friction, f_t. The increase in the weight percentage of crushed proppant occurred as a result of the increase in the friction between the grains contact, as the axial stress increased. Hence, the weight percentage of crushed proppants can be quantified from the fraction of grain contacts with friction.

$$W_c = a_4 f_t^{b_4} \tag{3.37}$$

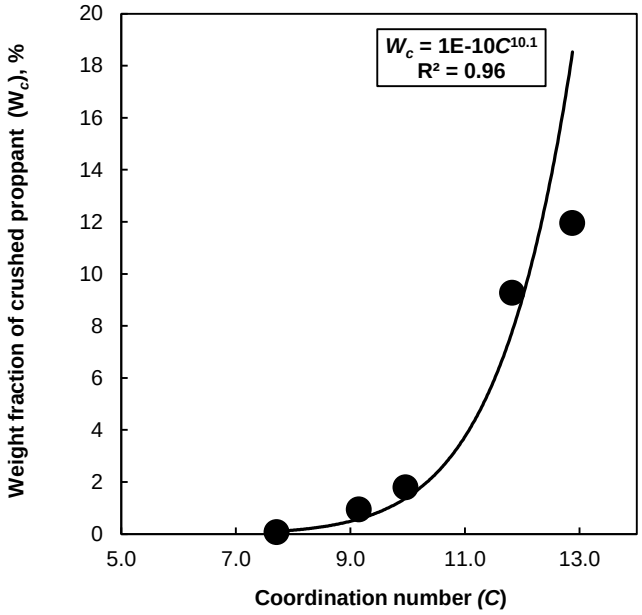

(a)

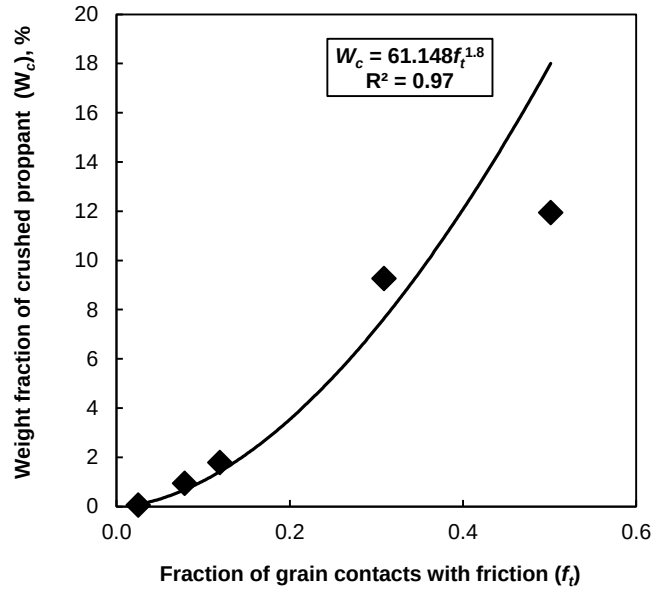

(b)

Fig. 3.15—Correlation between the weight percentage of the crushed proppants and (a) the coordination number, *C*, and (b) the fraction of grain contacts with friction (no slip).

3.4 Conclusions

I conducted uniaxial compression tests to characterize mechanical damage in proppant packs. The test included ultrasonic measurements which enabled the calculation of the dry elastic properties of proppant packs from the compressional- and shear-wave velocities. The stress-strain profile showed the regions of compaction, elastic and plastic behavior, when a maximum stress of 110 MPa was applied to the proppant pack. The stress-strain profile was in agreement with the results from the sieve analysis carried out on the proppant packs at corresponding stress levels. In the compaction region, no significant crushing of the proppant pack occurred. However, the amount of fines generated from crushing increased by about 50% in the region where the stress-strain profile changed from elastic to plastic behavior. The original porosity of the proppant pack was reduced by about 7% for the tests when a maximum axial stress of 110 MPa was applied. Both compressional- and shear-wave velocities of the proppant packs increased by over 100% due to compaction and crushing, when the maximum axial stress applied increased from 10 MPa to 110 MPa.

The dry bulk and shear moduli, estimated from the compressional- and shear-wave velocities of the proppant packs, also increased with the increase in applied axial stress. I used the Hertz- Mindlin effective medium model to estimate the effective bulk and shear moduli of the proppant pack. I calibrated the Hertz-Mindlin model by taking into account the effects of grain contact using the coordination number, C, and the fraction of grain contacts with friction, f_t, parameters. I also investigated porosity-dependent, pressure-dependent, and compressional velocity-dependent correlations for the coordination

number and the fraction of grain contacts with friction parameters. I demonstrated that the pressure-dependent correlations improved the prediction of the effective bulk and shear moduli of the proppant pack when the Hertz-Mindlin model was applied. I also demonstrated that the coordination number and the fraction of grain contacts with friction can be correlated to the weight fraction of crushed proppants. Therefore, the Hertz-Mindlin model can be applied in the interpretation of elastic property measurements of proppant packs, by incorporating the coordination number and the fraction of grain contacts with friction parameters. The correlations based on the coordination number and the fraction of grain contacts with friction, can be used to characterize the mechanical damage in proppant packs. The Hertz-Mindlin model assumes identical, homogeneous, isotropic, and elastic spherical grains. These assumptions may introduce limitations in the application of Equations 3.36 (i.e., correlating weight fraction of crushed proppants to coordination number) and 3.37 (i.e., correlating weight fraction of crushed proppants to fraction of grain contacts with friction), when proppants are crushed into much smaller grains at high axial stress conditions. Furthermore, the introduced method was applied on one type of proppant sieved to size 20/40 and with sphericity of 0.9. The experimentally derived coefficients in Equations 3.30 through 3.35 may vary depending on characteristics such as the type, size, and sphericity of the proppants. Hence, future research will include quantifying the effects of proppant characteristics on the coordination number and the fraction of grain contacts with friction parameters. The characterization of mechanical damage in proppants is of great significance in selection of proppants in completion design, to ensure a satisfactory proppant performance.

CHAPTER IV

APPLICATION OF MAGNETIC NANOPARTICLES MIXED WITH PROPPING AGENTS IN ENHANCING NEAR-WELLBORE FRACTURE DETECTION*

Reliable evaluation of proppant placement in hydraulic fractures is challenging because there are environmental and regulatory concerns about existing techniques which use radioactive tracers. Recent research investigations have shown the potential for the application of nanoparticles as contrast agents for reservoir characterization and advanced reservoir surveillance. This chapter demonstrates a new technique for using nanoparticles as contrast agents mixed with proppants that can enhance borehole geophysical measurements, such as magnetic susceptibility, thereby improving the near-wellbore detection of proppants in hydraulic fractures. The experimental approach used in this chapter consists of (a) synthesizing paramagnetic nanoparticles, and (b) carrying out a series of magnetic susceptibility core logging measurements, in the presence of the superparamagnetic nanoparticles (i.e., with a core/shell structure with size of 60 nm–70 nm) mixed with proppants.

The results of laboratory experiments showed that the relative enhancement of the volume susceptibility of the fractured zones depend on factors such as the type of proppants (e.g., magnetic versus non-magnetic proppants), the concentration of

*Part of this chapter is reprinted with permission from "Application of magnetic nanoparticles mixed with propping agents in enhancing near-wellbore fracture detection" by Aderibigbe A., Cheng, K., Heidari, Z., Killough, J., Fuss, T., and Stephens, W., 2016. *Journal of Petroleum Science and Engineering*, **141**, 133-143, Copyright 2016, with permission from Elsevier.

nanoparticles in the injected solution, and the volume of nanoparticle solution and proppants. The use of magnetic nanoparticles lead to a significant enhancement in the detection of fractures, even with widths as small as 0.3 cm. This detection technique can be applied in the field by using the borehole magnetic susceptibility tools for pre-fracturing and post-fracturing measurements in open-hole wells.

4.1 Introduction

In hydraulic fracturing, proppants are used to create conductive pathways for reservoir fluids by keeping the created fractures propped open. The success of a hydraulic fracturing stimulation process will largely depend on creating fractures that have geometries that are as close as possible to the model design geometry in the target zone. It is therefore necessary to have a good understanding of the location and geometry of the fractures generated by the treatment. This valuable information can be used to calibrate fracture models, design better hydraulic fracturing treatments, plan future workovers and infill drilling, and improve the reservoir characterization used in calculating fracture performance and recovery from the fractured wells.

Radioactive tracers have been used to evaluate the effectiveness of a hydraulic fracturing treatments. In this method, the fracturing fluid and proppants are tagged to give an indication of the propped height. The gamma rays emitted by these radioactive isotopes are detected and measured by gamma ray spectroscopy when the well is logged across the interval of the fracturing job (Gadekea et al., 1991; Gadeken and Smith, 1986). Some of the limitations of this method are the relatively short half-life of the tracers, the depth of

investigation of the gamma ray tools, and, most importantly, environmental and regulatory concerns on the use of radioactive materials. McDaniel et al. (2009) introduced another nuclear technique to address the environmental and safety concerns associated with the use of radioactive tracers. In this technique, resin-coated proppant is incorporated with a taggant that becomes radioactive when irradiated by a neutron source downhole, for a period sufficient for detection by spectrum and natural gamma ray detectors. Some limitations of this technique include its dependence on having uniform and known concentration of taggant, logging speed, tool design (location of source and detectors), and shorter depth of investigation (McDaniel et al., 2009). Saldungaray et al. (2012) proposed another nuclear method and applied it in the field to determine fracture height. The method uses a high thermal neutron capture compound (HTNCC) taggant incorporated in the proppant. The compensated neutron tool (CNT) or pulsed neutron capture (PNC) tool are used to detect the presence of HTNCC by comparison of pre-fracturing and post-fracturing logging runs. In some cases, only the post-fracturing CNT log can be run, and the near to far detector ratios, as well as the detector count rates can be used to determine the presence of the proppants. Some limitations of these techniques could be the effect of borehole environments and borehole conditions, since these methods require uniform conditions of measurement.

In this work, superparamagnetic nanoparticles are used as contrast agents to tag the proppants. The presence of the proppants can therefore be detected by logging tools sensitive to the magnetic properties of the nanoparticle agents. The injection of nanoparticles with proppants or proppants containing magnetic nanoparticles to detect

location of hydraulic fractures has been previously introduced (Barron et al., 2012; Crews et al. 2010; Huh et al. 2014; Potter et al., 2011; Schmidt and Tour, 2012). However, sensitivity of borehole geophysical measurements to the presence of these contrast agents in the fractures has not been quantified yet. Magnetic nanoparticles have been used successfully in medicine and biomedicine for targeted drug delivery and as contrast agents in magnetic resonance imaging (MRI). Research studies in the petroleum industry have been investigating the development of nanoparticles as contrast agents for reservoir characterization and advanced reservoir surveillance. Some of the ongoing research studies are investigating the use of nanoparticles as contrast-enhancing agents to enhance traditional data acquisition methods such as nuclear magnetic resonance (NMR), controlled source electromagnetic (CSEM) surveys. Rahmani et al. (2013) carried out numerical simulations of magnetic permeability measurements and showed the value of using superparamagnetic nanoparticles as magnetic contrast agents in crosswell electromagnetic tomography. Barron (2010) described research efforts by the Advanced Energy Consortium (AEC) to investigate a downhole magnetic susceptibility (MS) tool that can detect proppants tagged with superparamagnetic nanoparticles.

The superparamagnetic nanoparticles have a relatively higher magnetic susceptibility than the natural environment of the formation, hence, when pumped with proppants during hydraulic fracture stimulation treatments, they can act as contrast agents that highlight the fracture and detect the location of the proppants. In field applications, magnetic susceptibility measurements can be made using a borehole magnetic susceptibility tool. The magnetic susceptibility tool can be deployed with stand-alone

telemetry or in combination with a commercial logging toolstring. It is built with both high and low resolution sensors. The high resolution sensor has a 12 cm vertical resolution and a 3 cm depth of investigation, while the low resolution sensor has a 40 cm vertical resolution and a 40 cm depth of investigation (Robinson et al., 2008). Robinson et al., (2008) also documents additional information about the magnetic susceptibility tool's dimensions and operating specifications.

Previous studies showed the potential of magnetic susceptibility measurements for rock characterization and identification of oil-bearing intervals (Ali et al., 2013; Potter, 2007; Potter et al., 2011). Morrow et al. (2015) conducted laboratory experiments and compared the relative magnetic susceptibility of mixtures of magnetic nanoparticles and proppants against the magnetic susceptibility of shale core samples. They estimated the amount of magnetic nanoparticles required per well to achieve detection above the shale samples. However, the effect of fracture width and volume of investigation of the magnetic susceptibility sensors, which is important in the detection of propping agents was not taken into account in Morrow et al.'s publication. In this study, I investigate the possibility of using mixtures of nanoparticles and proppants to characterize fractured rock samples using magnetic susceptibility measurements.

4.2 Principles of Magnetic Susceptibility and Magnetic Properties of Materials

Magnetic susceptibility can be explained simply as the measure of the ability of materials to be magnetized when exposed to a magnetic field. It is defined as the ratio of

the magnetization induced in a sample, M, to the intensity of the applied magnetization field, H, via

$$M = \kappa H, \tag{4.1}$$

Magnetic susceptibility can be expressed either as volume susceptibility, κ, or as a mass normalized susceptibility, χ. The volume susceptibility is a dimensionless quantity in the SI system of units. The mass susceptibility is equal to the volume susceptibility divided by density and has units of cubic meters per kilogram in the SI system of units (Dearing, 1994).

The measure of magnetic susceptibility of most materials varying depending on their magnetic structure. The three basic groups of magnetic materials are diamagnetic, paramagnetic, and ferromagnetic materials (Hrouda et al., 2009). Diamagnetic materials have a weak and negative susceptibility, and are repelled by the applied magnetic field. Common diamagnetic materials include silver, copper and gold. Examples of diamagnetic minerals include quartz, plagioclase, calcite and water. Paramagnetic materials have a low and positive susceptibility, and are weakly attracted by the applied magnetic field. Common paramagnetic materials include magnesium, molybdenum, lithium, and tantalum. Examples of paramagnetic minerals include biotite, chlorite, mica and olivines. Both diamagnetic and paramagnetic materials do not retain the magnetic properties when the magnetic field is removed.

Ferromagnetic materials have a high and positive susceptibility, and are strongly attracted by the applied magnetic field. Unlike the other groups of magnetic material,

ferromagnetic materials retain the magnetic properties when the magnetic field is removed. Common ferromagnetic materials include iron, cobalt, and nickel. Examples of ferromagnetic minerals include magnetite, hematite, ilmenite, pyrrhotite, and maghaemite. The bulk magnetic susceptibility measurements of rocks depend on the mineralogy and geochemical components, and are enhanced by the presence of magnetic materials in the rock (Benz, 2012). Apart from the basic groups of diamagnetism, paramagnetism, and ferromagnetism, superparamagnetism is another form of magnetism. This form of magnetism occurs in small ferromagnetic or ferromagnetic materials such as nanoparticles. Superparamagnetic materials have a much larger magnetic and positive susceptibility than paramagnetic materials. However, like paramagnetic materials, they attracted by the applied magnetic field, and the net magnetization is zero when the magnetic field is removed.

Fig. 4.1 shows the relationship between magnetization and the intensity of the inducing magnetization field for diamagnetic, paramagnetic, and ferromagnetic materials. Ferromagnetic materials generate a magnetic hysteresis loop as shown in Fig. 4.1. The saturation magnetization is the state reached when the magnetization of a material cannot increase further in response to the increase in the applied magnetization field (Hrouda et al., 2009).

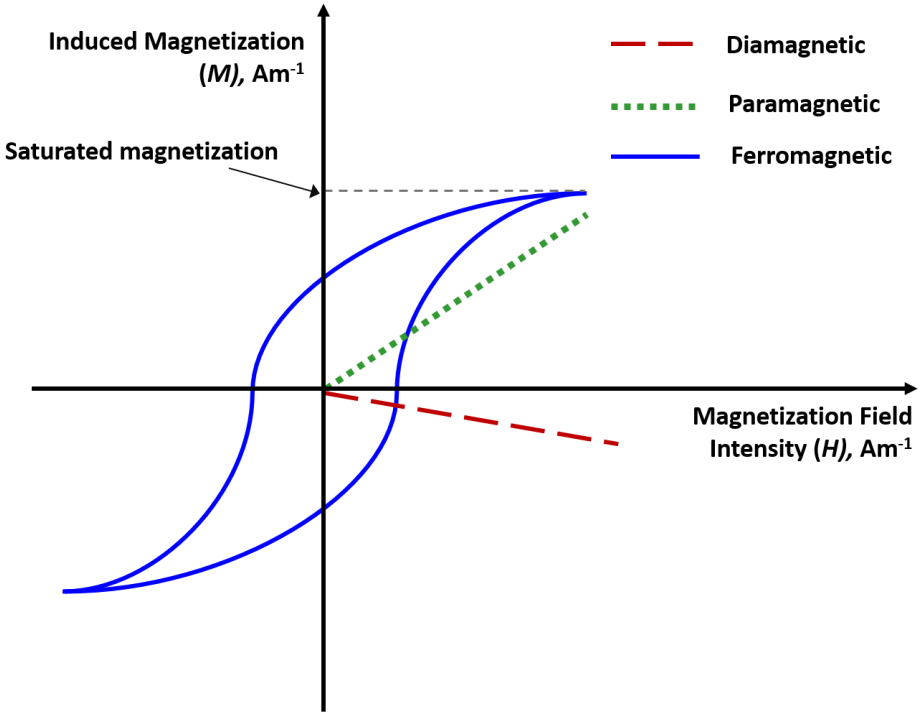

Fig. 4.1—Schematic representation of the relationship between induced magnetization, *M*, and the intensity of the inducing magnetization field, *H*, for diamagnetic, paramagnetic, and ferromagnetic materials.

4.3 Method

Synthesized superparamagnetic nanoparticles are characterized to determine their size, chemical composition, and magnetic properties. The synthesized nanoparticles are then used for magnetic susceptibility core logging laboratory experiments. In this experiments, I investigate the use of superparamagnetic nanoparticles mixed with proppants as magnetic contrast agents in magnetic susceptibility measurements.

4.3.1 Synthesis and characterization of nanoparticles

Carbon-coated magnetic nanoparticles were prepared using the solvothermal chemical approach. The size of the nanoparticles was measured using a transmission electron microscope (TEM), while the structural analysis was obtained using the X-ray diffraction (XRD) method. The saturated magnetization and magnetic hysteresis loop of the nanoparticles was measured using a superconducting quantum interference device (SQUID) magnetometer. More details about the preparation and methods of the characterization of the nanoparticles are discussed in a previous publication by Cheng et al. (2014).

4.3.2 Design of magnetic susceptibility experiments

I conducted laboratory experiments of magnetic susceptibility on outcrop samples from the Austin chalk formation and organic-shale rock samples from the Haynesville formation, which represent rocks with different mineral composition. The samples were cut into cylindrical cores with a diameter of 5.08 cm. I represented fractures by leaving an aperture between the cores while holding the cores in place using a polyolefin heat shrink tubing. The aperture was filled with proppants and fluids being tested. Apart from the shrink tubing, the sides of the samples directly facing the fractures were covered with Teflon tape to minimize leakage of fluids. **Fig. 4.2a** shows a schematic of the core assembly. In the experiments, the magnetic susceptibility of the core assembly was measured at intervals of 0.5 cm using a core loop sensor with a diameter of 8 cm, mounted on a multisensor core logging instrument as shown in **Fig. 4.2b**.

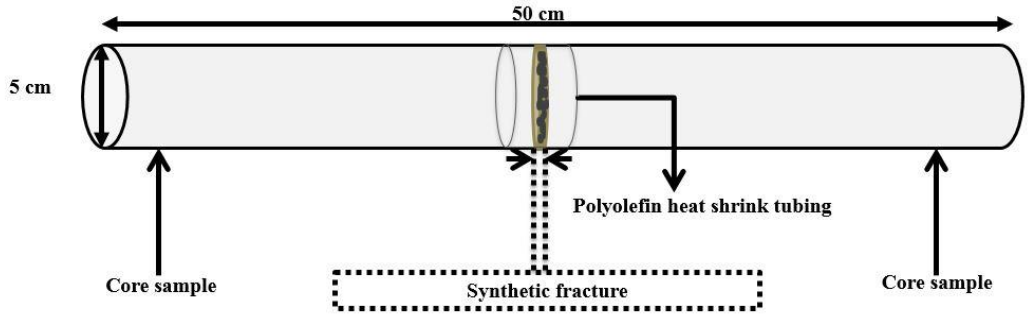

(a)

(b)

Fig. 4.2—(a) The fractured core assembly, and (b) Multisensor core logger with inset showing a core assembly being run through the magnetic susceptibility core loop sensor.

Magnetic field is produced by an oscillator circuit in the core loop sensor. An induced magnetic field is created, and the degree of magnetization of a material in response to this magnetic field is measured. The magnetic susceptibility sensor is designed with a calibration that ensures that the values measured will be the same on different measuring systems. I also calibrate the sensor before each run to eliminate any thermally

induced drift in the sensor. The resulting measurements are expressed as uncorrected volume specific magnetic susceptibilities, κ_{uncor}. This uncorrected volume susceptibility measurements were corrected for the relative effect of the size of core samples and the size of the loop sensor being used, to obtain the volume specific magnetic susceptibilities, κ, via

$$\kappa = \kappa_{uncor} / \kappa_{rel} . \tag{4.2}$$

The relative response, κ_{uncor}, has been determined experimentally by the manufacturer of the sensors and the relationship is given as (Bartington, 2010)

$$\kappa_{rel} = 3.45 \times \left(\frac{d}{D_l + 0.8\,cm} \right)^3 , \tag{4.3}$$

where d is the core diameter and D_l is the loop sensor diameter.

I measured the influence of the presence of nanoparticles mixed with two types of intermediate proppants (IP) in fractures created in the rock samples. For the balance of this chapter, the proppant samples will be referred to as IP-1 and IP-2. Both types of proppants are bauxite-based ceramic proppants. Both proppants are non-radioactive and environmentally friendly. For both cores from the Austin chalk formation and organic-shale rock samples from the Haynesville formation, I investigated the sensitivity of magnetic susceptibility measurements to (a) type of proppants (e.g., magnetic versus non-magnetic proppants), (b) the concentration of nanoparticles, (c) width of the induced fracture that is controlled by volume of proppants and nanoparticle solution.

4.4 Results and Discussions

4.4.1 Superparamagnetic nanoparticles

The synthesized superparamagnetic nanoparticles have a size ranging from 60 nm to 70 nm, and a core-shell structure which consists of carbon on the shell and iron oxide in the core. The nanoparticles have a saturated magnetization of 33.3 emu/g and 31.8 emu/g, when measurements are carried out at room (300 K) and subsurface temperatures (360 K) respectively. The minor change in saturated magnetization of about 1.47 emu/g, demonstrates that there is no significant loss of magnetization of the nanoparticles when exposed to high temperature reservoirs; hence the nanoparticles are suitable for subsurface applications. A previous publication by Cheng et al. (2014) includes more details about the results of the characterization of the nanoparticles.

4.4.2 Magnetic susceptibility analysis

4.4.2.1 Measurements on bulk nanoparticle solutions

Nanoparticle solutions with concentrations ranging from 5 kppm to 312.5 ppm were placed into cylindrical sample tubes with dimensions of 1.35 cm diameter and 8 cm length. Each sample tube was passed through magnetic susceptibility sensors for volume susceptibility measurements. **Fig. 4.3** shows the volume susceptibility of the superparamagnetic nanoparticle fluids detected for the observed length of sample, and how this varies with different concentrations of the nanoparticles. The peak values of the magnetic susceptibility measurements are plotted as a function of the concentration of the nanoparticles in **Fig. 4.4**.

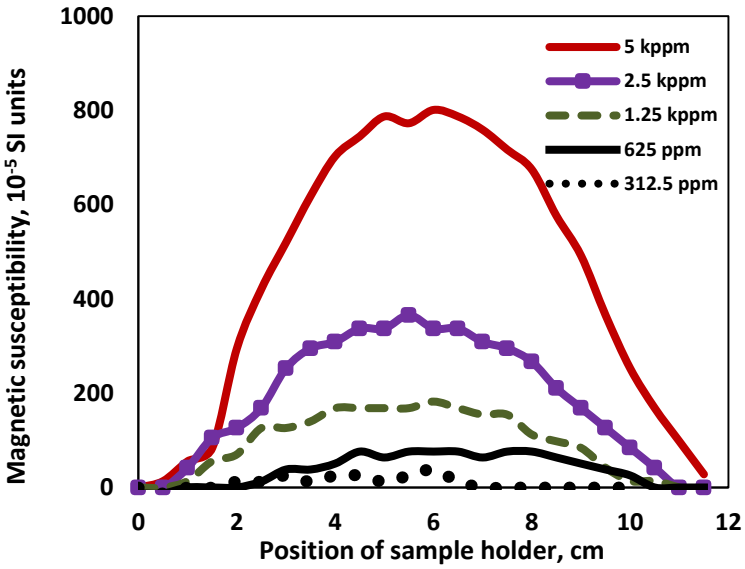

Fig. 4.3—Magnetic susceptibility measurements of different concentrations of bulk superparamagnetic nanoparticle solution.

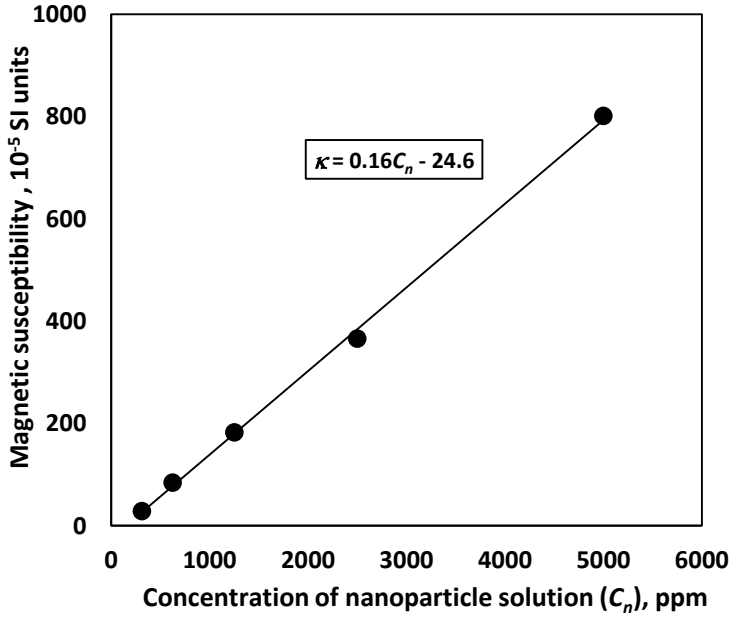

Fig. 4.4—Peak magnetic susceptibility measurements vary linearly with different concentrations of bulk superparamagnetic nanoparticle solution.

I observe a linear correlation between volume susceptibility (κ) and concentration of nanoparticles, C_n given by

$$\kappa = 0.16C_n - 24.6. \tag{4.4}$$

4.4.2.2 Sensitivity of magnetic susceptibility measurements to type of proppants

Fig. 4.5 compares the magnetic susceptibility measurements of the two types of proppants (IP-1 and IP-2) placed in the fracture of outcrop samples from the Austin chalk formation. The outcrop samples were cut into cylindrical cores with a total length of 50 cm. The cylindrical cores were then arranged to leave an aperture to represent a hydraulic fracture at a depth of about 20 cm as shown in Fig. 4.5. The fracture was filled with 6 g of proppant (IP-1 and IP-2) and deionized water. The outcrop samples from the Austin chalk formation consist mainly of calcite. Minerals such as calcite are classified as diamagnetic materials, hence they have negative magnetic susceptibilities. When I filled the fracture with IP-1 proppants, the measured volume susceptibility of the sample was -1.5×10^{-5} SI units with no indication of any change in the location of the fracture, because the proppants do not contain any magnetic component. After I filled the fracture with IP-2 proppants, the volume susceptibilities of the rock increase to 20×10^{-5} SI units in the location of the fracture. The result confirms the presence of magnetic components in IP-2 proppants, and also demonstrates the measurable sensitivity of the magnetic susceptibility measurements to the presence of the magnetic IP-2 proppants.

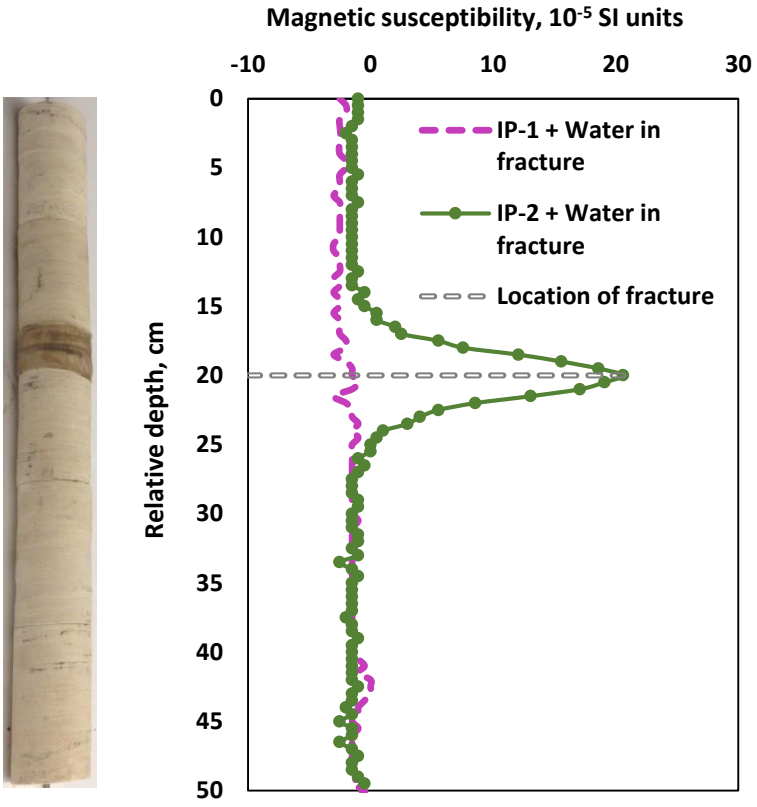

Fig. 4.5—Sensitivity of magnetic susceptibility measurements to type of proppants: Magnetic susceptibility measurements of a fracture filled with a mixture of IP-1 proppants and water compared to a fracture filled with a mixture of IP-2 proppants and water. The mixture of proppants and water are placed in the fracture of the calcite-rich rock sample as shown in the figure.

4.4.2.3 Sensitivity of magnetic susceptibility measurements to concentration of nanoparticles in fractures

I repeated the aforementioned procedure for magnetic susceptibility measurements with the fracture filled with 6 g of proppant and 2 cm^3 of different concentrations of nanoparticle in solution (i.e., 5 kppm and 1.25 kppm). **Figs. 4.6a** and **4.6b** show the measured magnetic susceptibility of the fractured calcite-rich cores in the

presence of nanoparticles mixed with IP-1 and IP-2 proppants in the fracture, respectively. The volume susceptibility at the center of the fracture of the fractured rock increases from approximately -1.5×10^{-5} SI units to 6×10^{-5} SI units when the fracture is filled with a mixture of IP-1 proppants and 5 kppm nanoparticle solution. After diluting the nanoparticle solution from 5 kppm to 1.25 kppm, the volume susceptibility increases from approximately -1.5×10^{-5} SI units to 3.5×10^{-5} SI units. When the fracture is filled with a mixture of magnetic proppants (IP-2) and nanoparticle solution, the presence of the 1.25 kppm and 5 kppm solutions further increases the volume susceptibilities in the fracture location from 20×10^{-5} SI units to 22×10^{-5} SI units and 28×10^{-5} SI units, respectively.

Figs. 4.7a and **4.7b** show the measured magnetic susceptibility of the fractured organic-shale rock sample in the presence of nanoparticles mixed with IP-1 and IP-2 proppants in the fracture, respectively. The length of the shale sample is 50 cm, and the proppants are placed in the fracture at the relative depth of 25 cm (i.e., center of the cylindrical core sample) as shown in Figs. 4.6a and 4.6b. I observe a high initial magnetic susceptibility in the organic-shale rock sample, because of the naturally high magnetic susceptibility of organic shale rocks. Organic shales can contain pyrite and clay minerals such as illite and chlorite. These minerals fall into the group that exhibit paramagnetism, which contribute to the overall magnetic property of the samples (Dearing, 1994).

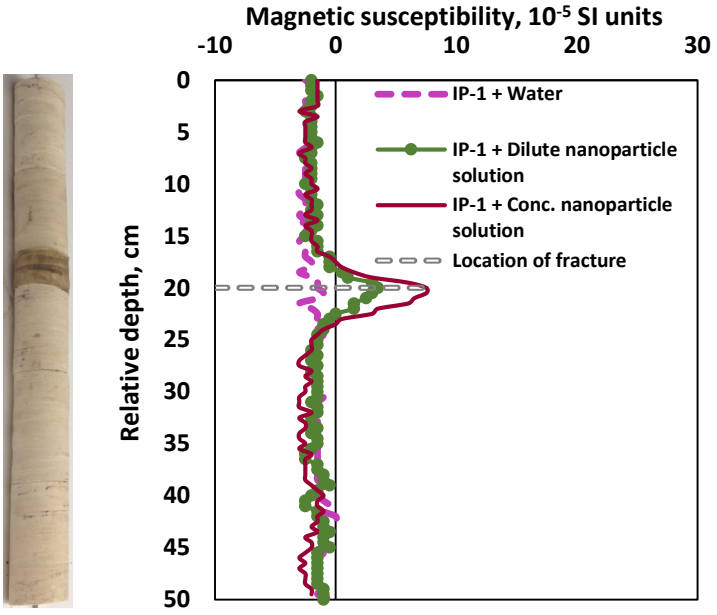

(a)

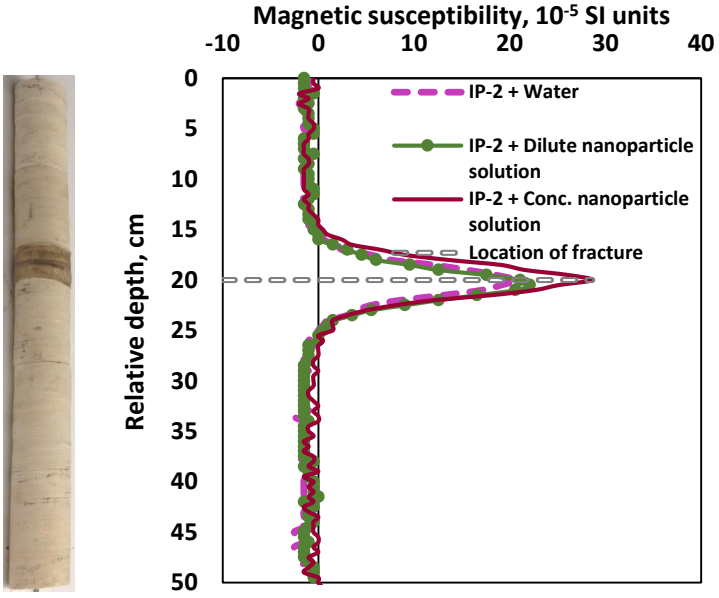

(b)

Fig. 4.6—Sensitivity of magnetic susceptibility measurements to the concentration of nanoparticles in the fracture, calcite-rich rock sample: The figure shows magnetic susceptibility measurements before and after mixing (a) IP-1 proppants and (b) IP-2 proppants with diluted and concentrated nanoparticle solution in the fracture, respectively. The mixture of proppants and nanoparticle solutions are placed in the fracture of the calcite-rich rock as shown in the figure.

There is a relatively high magnetic susceptibility in the first 5 cm section of the shale samples compared to the rest of the shale sections. I observe concentration of pyrite, which contributes to the increase in magnetic susceptibility in this section as shown in Fig. 4.7. When IP-1 proppants are mixed with a 5 kppm nanoparticle solution, the presence of the nanoparticles causes the volume susceptibility of the fractured rock to increase from 19×10^{-5} SI units to 27×10^{-5} SI units. After diluting the nanoparticle solution from 5 kppm to 1.25 kppm, the volume susceptibility in the fractured rock only increases from 19×10^{-5} SI units to 21×10^{-5} SI units. When the magnetic proppants (IP-2) are mixed with a 5 kppm nanoparticle solution, the presence of the nanoparticles further increases the volume susceptibilities of the fractured rock from 37×10^{-5} SI units to 43×10^{-5} SI units. After diluting the nanoparticle solution from 5 kppm to 1.25 kppm, the volume susceptibility in the fractured rock only increased from 37×10^{-5} SI units to 39×10^{-5} SI units.

Tables 4.1 and **4.2** summarize the results of the sensistivity of the volume susceptibility measurements to the concentration of nanoparticles in solution.

Table 4.1—Summary of the assumed experimental parameters and the results for laboratory experiments on mixture of IP-1 proppants and nanoparticle solution.

Concentration of nanoparticle solution, kppm	Volume susceptibility of fractured calcite-rich sample, 10^{-5} SI units	Volume susceptibility of fractured organic-shale sample, 10^{-5} SI units
0	-1.5	19
1.25	3.5	21
5.0	6	27

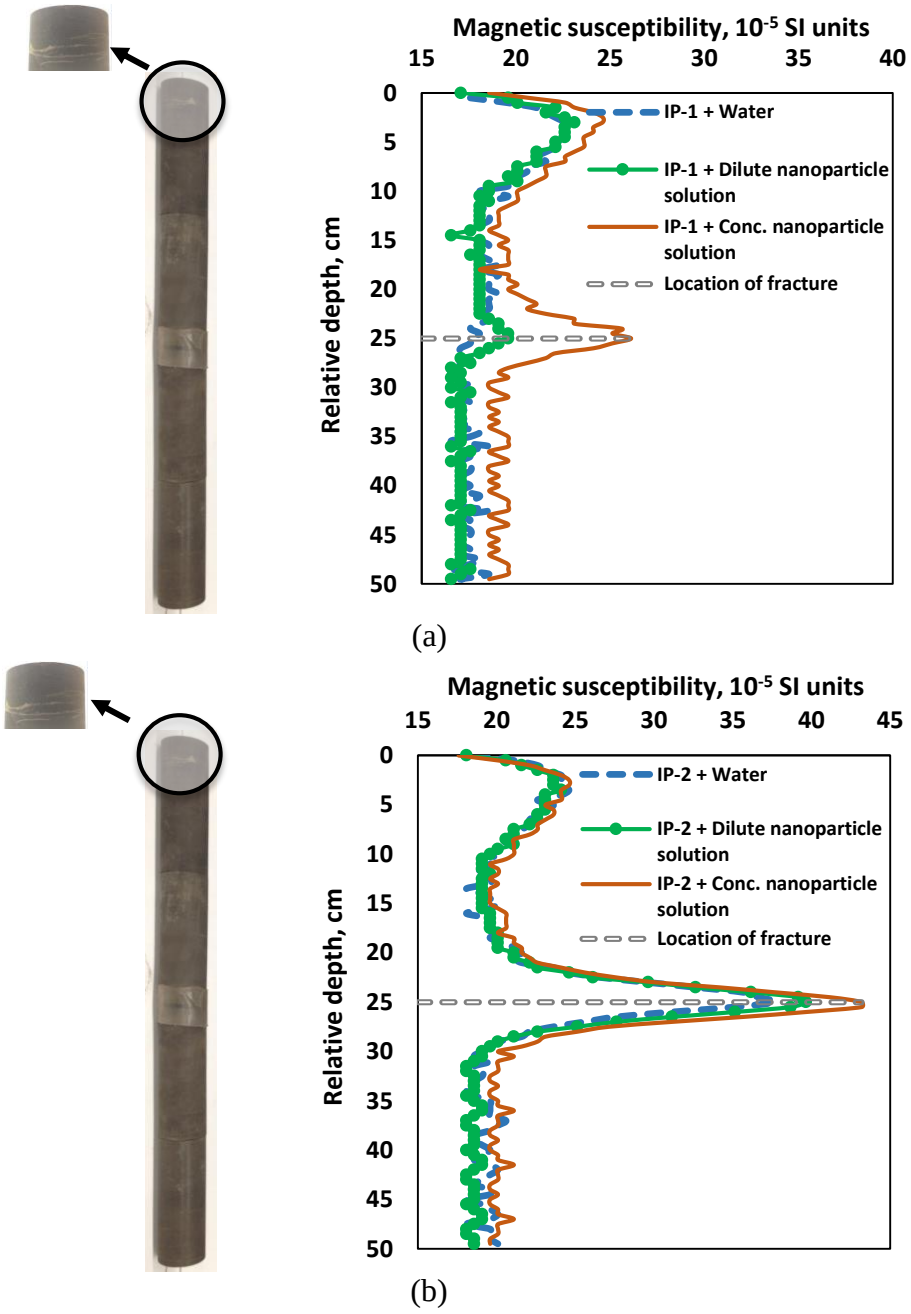

Fig. 4.7—Sensitivity of magnetic susceptibility measurements to the concentration of nanoparticles in the fracture, organic-shale rock sample: The magnetic susceptibility measurements before and after mixing (a) IP-1 proppants and (b) IP-2 proppants with diluted and concentrated nanoparticle solution in the fracture, respectively. The mixture of proppants and nanoparticle solutions are placed in the fracture of the organic-shale rock sample as shown in the figure.

Table 4.2— Summary of the assumed experimental parameters and the results for laboratory experiments on mixture of IP-2 proppants and nanoparticle solution.

Concentration of nanoparticle solution, kppm	Volume susceptibility of fractured calcite-rich sample, 10^{-5} SI units	Volume susceptibility of fractured organic-shale sample, 10^{-5} SI units
0	20	37
1.25	22	39
5.0	29	43

The magnitude of volume susceptibility at the middle of the fracture in the core samples were increased by an average of 4×10^{-5} SI units when I added 1.25 kppm nanoparticle solution to the IP-1proppants. The increase in magnetic susceptibility was doubled to an average of 8×10^{-5} SI units after I added 5 kppm nanoparticle solution to the IP-1 proppants. The magnitude of volume susceptibilities of the rock samples only increased by an average of 2×10^{-5} SI units with the addition of 1.25 kppm nanoparticle solution to IP-2 proppants. The magnitude of volume susceptibilities also increased by an average of 8×10^{-5} SI units when 5 kppm nanoparticle solution was added to the IP-2 proppants.

4.4.2.4 Sensitivity of magnetic susceptibility measurements to fracture width

Figs. 4.8a and **4.8b** show the measured magnetic susceptibility of the fractured calcite-rich and organic-shale rock samples, respectively, when the fractures are filled with different amounts of the IP-2 proppant and water. The mass of proppants, estimated fracture widths and the volume susceptibility measurements at the middle of the fracture in Figs. 4.8a and 4.8b are summarized in **Table 4.3**.

Table 4.3—Summary of the assumed experimental parameters and the results for analysis with varying mass of IP-2 proppants. The different mass of proppant corresponds to different fracture widths, hence different volumes of proppant.

Mass of IP-2 proppant, g	Estimated fracture width, cm	Volume susceptibility of fractured calcite-rich sample, (10^{-5} SI unit)	Volume susceptibility of fractured organic-shale sample, (10^{-5} SI unit)
-	-	-1.5	19
2	0.08	6	26
6	0.24	20	37
12	0.48	38	57

Fig. 4.9 depicts the linear correlation between the change in magnetic susceptibility at center of the fracture and the mass of IP-2 proppants. I observed that with every addition of 2 g of IP-2 proppants, the magnitude of the volume susceptibility increased by an average of 6.5×10^{-5} SI units in the fractured core samples. **Fig. 4.10** shows the change in magnetic susceptibility at the center of the fracture measured at different fracture widths. The linear correlation illustrated in Fig. 4.10 can be used to estimate the expected change in volume susceptibility at different average hydraulic fracture widths. I estimated the average propped fracture width using an approximation of 3 to 7 proppant diameters (King, 2010) for different sizes of proppants, and estimated the change in magnetic susceptibility.

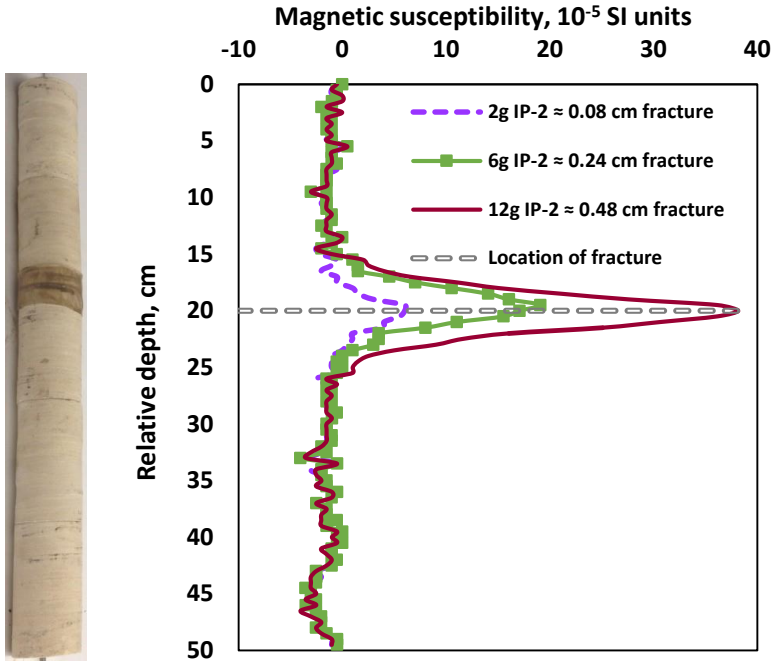

(a)

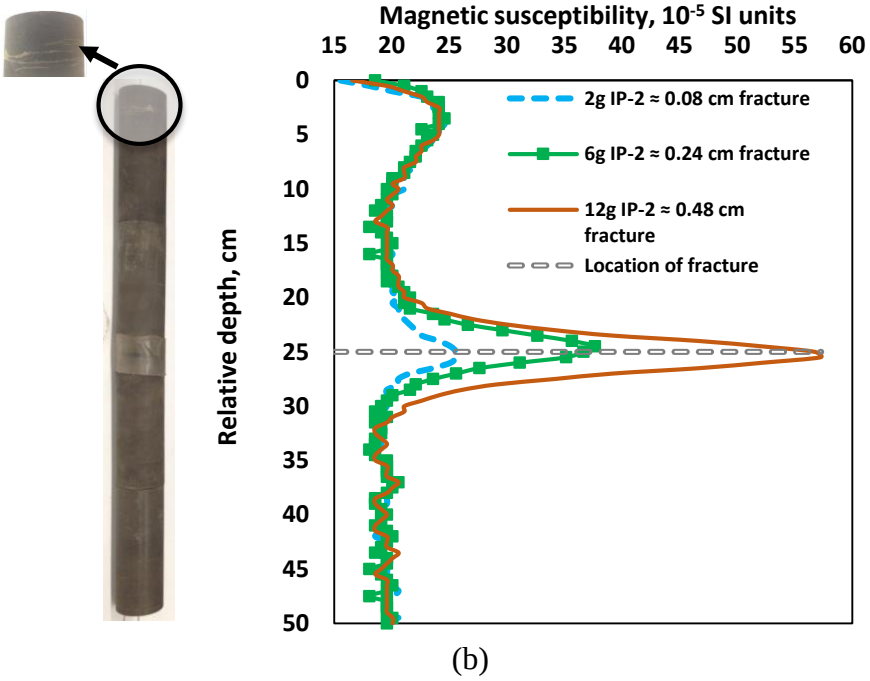

(b)

Fig. 4.8—Sensitivity of magnetic susceptibility measurements to fracture width: Magnetic susceptibility measurements in a fracture filled with varying mass of magnetic proppants (IP-2), generating varying fracture width in (a) calcite-rich rock sample and (b) organic-shale rock sample.

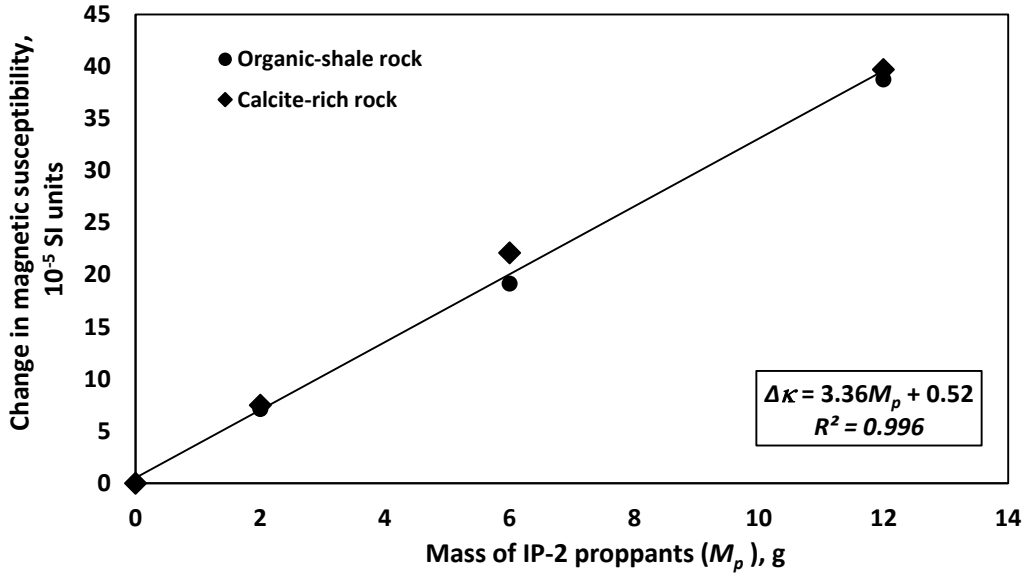

Fig. 4.9—Change in magnetic susceptibility measurements at the center of the fracture vary linearly with the mass of IP-2 proppants in the fractured rock samples.

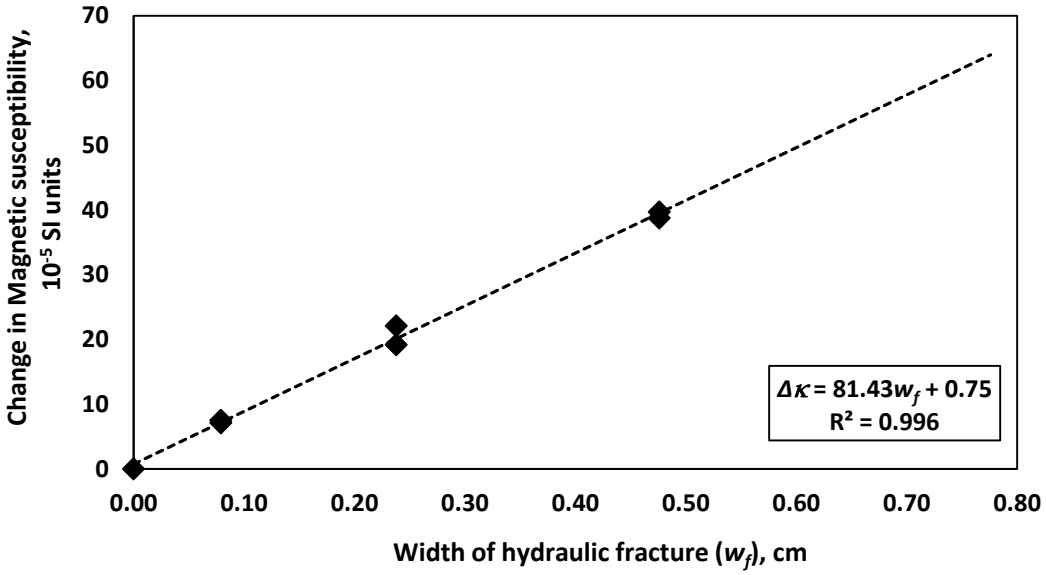

Fig. 4.10—Change in magnetic susceptibility measurements at the center of the fracture vary linearly with fracture width.

The results, listed in **Table 4.4**, demonstrate the effectiveness of the magnetic susceptibility measurement in detecting propped hydraulic fracture width as small as 0.3 cm.

Table 4.4—Estimated change in magnetic susceptibility values at different fracture widths, in the presence of magnetic proppants.

Size of proppant	ISO mean diameter, cm	Range of average fracture width, cm (3× proppant diameter to 7× proppant diameter)	Range of change in volume susceptibility, 10^{-5} SI units
12 / 18	0.138	0.41 - 0.97	35 - 80
16 / 30	0.098	0.29 - 0.69	25 - 57
20 /40	0.073	0.22 - 0.51	19 - 43
30 / 50	0.048	0.14 - 0.34	13 - 28

4.5 Conclusions

In this chapter, I demonstrated the successful application of synthesized magnetic nanoparticles as contrast agents to enhance detection of hydraulic fractures when injected with proppants into the fractures. I conducted a series of magnetic susceptibility experiments on rocks with different mineral compositions including fractured calcite-rich and organic-shale samples.

The results of the laboratory experiments demonstrated that the presence of magnetic nanoparticles in the fractures provide high sensitivity to the presence of fractures when used as contrast agents in magnetic susceptibility measurements. The IP-2 proppants showed a higher magnetic susceptibility than the IP-1 proppants. The sensitivity analyses

showed that the change in magnitude of the volume susceptibility is linearly proportional to the concentration of nanoparticle in solution, and to the mass and volume of magnetic proppants (IP-2 proppants).

The volume susceptibility increased by 6.5×10^{-5} SI units per 2 g increase in IP-2 proppants. The analysis also shows that the volume susceptibility increased by about 24×10^{-5} SI units for fracture width as small as 0.3 cm (0.1 in). The volume susceptibility changes due to the presence of magnetic nanoparticles and proppants, as demonstrated in the laboratory measurements, can also be expected when borehole magnetic susceptibility logging tool is used. Expedition 340T Scientists (2012) documents datasets showing agreements between laboratory core magnetic susceptibility and borehole magnetic susceptibility log measurements. Due to the limitation of the depth of investigation of the borehole magnetic susceptibility tool, this technique is best suited for near-wellbore detection of proppant location and possible indication of the fracture height. Furthermore, the proposed technique is mainly applicable in open-hole wells because of the interference of the magnetic susceptibility measurements by steel casing in cased-hole wells.

In summary, I have shown that the synthesized superparamagnetic nanoparticles can be used as contrast agents mixed with proppants to highlight the fractures and detect the location of proppants by magnetic susceptibility measurements. Further developments on this technique will lead to improvements in the determination of the hydraulic-fracture geometry, which is of great value in designing hydraulic fracturing treatments.

CHAPTER V

SUMMARY, CONCLUSIONS AND RECOMMENDATIONS

This chapter documents the summary of the main contributions of the research on the application of petrophysical and geophysical analysis in improvement of completions design in organic-rich mudrocks. The conclusions from the results in the research are reported, and recommendations for future research are documented.

5.1 Summary

In addressing the concern of the selection of zones for completion in pre-completions design, I introduced an integrated rock classification technique that takes into account stress gradient, reservoir quality and geologic attributes of the formation. The workflow for the integrated rock classification method is based on four classification schemes including (a) geologic facies, (b) reservoir quality, (c) stress profile, and (d) completion quality. I obtained the geologic facies classification using core description, thin-section analysis and well-log measurements. The reservoir quality classification was obtained from petrophysical and compositional analysis. The stress profile classification was obtained from geomechanical analysis using appropriate model that captures the anisotropy in organic-rich mudrocks, and also takes into account anisotropic poroelastic coefficients. I applied the introduced technique to a well located in the Wolfcamp formation of the Delaware basin, and made recommendations for fracture initiation and fracture zones in the upper, middle and lower intervals of the Wolfcamp formations.

I developed a new technique for the characterization of mechanical damage in proppant packs by geophysical analysis of acoustic measurements, to address the challenge in selection of proppants in pre-completions design. I conducted uniaxial compression tests to characterize mechanical damage in proppant packs. The test included ultrasonic measurements which enabled the calculation of the elastic properties of proppant packs. Furthermore, I predicted the elastic properties of proppant packs by applying the Hertz-Mindlin effective medium theory for granular media. The interpretation of the predicted and laboratory elastic properties was used to obtain calibration parameters which were correlated to mechanical damage in the proppant packs. The characterization of mechanical damage in proppant packs can improve design of the propping agents and quantification of proppant performance.

Finally, I investigated the application of magnetic nanoparticles as contrast agents to enhance detection of hydraulic fractures when injected with proppants into the fractures. This investigation addresses the post-completions challenge of detecting the location of hydraulic fractures after the stimulation treatment. I conducted a series of magnetic susceptibility experiments on rocks with different mineral compositions including fractured calcite-rich and organic-shale rock samples, proppants with different compositions, and different concentrations of nanoparticle solution.

5.2 Conclusions

5.2.1 Integrated rock classification in the Wolfcamp Shale Formation based on geological evaluation, reservoir quality, and anisotropic stress profile estimated from well logs

i. The introduced integrated rock classification technique provided a reliable workflow for selecting the best zones for completion in organic-rich mudrocks.

ii. The rock classification technique represented a holistic assimilation of geologic attributes, geomechanical, petrophysical and compositional properties of the formation.

iii. The developed workflow demonstrated the direct application of well logs for the determination of depth-by-depth characterization of geologic facies of the formation. The workflow also demonstrated the application of well-log based estimates for the determination of depth-by-depth reservoir quality classification in the formation.

iv. Compared to previous conventional techniques, the geomechanical analysis workflow in this study accounted for anisotropy in organic-rich mudrocks, and also the effect of anisotropic Biot's poroelastic parameters.

v. The integrated rock classification was applied to a well in the Wolfcamp Shale formation. I recommended the interval in the middle of the upper Wolfcamp as a zone for initiation of fractures, which can propagate through most of the upper Wolfcamp interval and the top of the middle Wolfcamp. I also recommended that

the intervals in the center of the middle Wolfcamp, and bottom of the lower Wolfcamp formations were ideal as barriers for fracture containment.

5.2.2 Mechanical damage characterization in proppant packs using acoustic measurements

i. The new characterization technique demonstrated that acoustic measurements were sensitive to the presence of crush in proppant packs, hence can be used to quantify mechanical damage.

ii. The stress-strain profile, obtained from the uniaxial compression test, was used to identify the regions of compaction, elastic, and plastic behavior in the proppant packs.

iii. The Hertz-Mindlin effective medium approximation can be applied for the prediction of elastic properties of proppant packs. The results of the application demonstrated that the agreement between the model predictions and laboratory measurements from ultrasonic tests on proppant packs.

iv. The calibration parameters of the Hertz-Mindlin model- coordination number and the fraction of grain contacts with friction, can be correlated to the weight percentage of crushed proppants. The correlations can be applied in the quantification of mechanical damage in proppants.

5.2.3 Application of magnetic nanoparticles mixed with propping agents in enhancing near-wellbore fracture detection

i. The laboratory procedures developed in this study can be used to measure the sensitivity of magnetic susceptibility measurements to the presence of magnetic nanoparticles in the fractures. The design of experiments proved to be effective in investigating the effects of type of proppants, the concentration of nanoparticles in the injected solution, and the width of fractures, on magnetic susceptibility measurements.

ii. IP-2 proppants showed a higher magnetic susceptibility than the IP-1 proppants. The type of formations (i.e., whether characterized by diamagnetic or paramagnetic minerals) does not affect the magnitude of change in magnetic susceptibility caused by the presence of nanoparticles in the fractures of the formation. However, the change in magnitude of the magnetic susceptibility is linearly proportional to the concentration of nanoparticle in solution, and to the mass and volume of magnetic proppants (IP-2 proppants). The volume susceptibility increased by 6.5×10^{-5} SI units per 2 g increase in IP-2 proppants.

iii. The linear correlations can be used to predict the estimated change in magnetic susceptibility for different sizes of proppants.

iv. The results of the study demonstrated that the proposed detection technique can be applied for near-wellbore detection of proppant location and possible indication of the fracture height.

5.3 Limitations and Recommendations

The research in this dissertation has proposed and applied new techniques, measurements, and workflows for improvement of completions design in organic-rich mudrocks. The following section highlights some limitations of these techniques and workflow, and also provides possible directions to advance the technical contributions of the research initiated in this dissertation.

5.3.1 Recommendations for the developed integrated rock classification in the Wolfcamp Shale Formation based on geological evaluation, reservoir quality, and anisotropic stress profile estimated from well logs

i. In the geomechanical analysis, the availability of more core measurements can improve the application of the modified ANNIE and further modified ANNIE anisotropic model approximations.

ii. Actual field tests such as minifracture and injection tests are very important for validating the in-situ stress predictions. These actual measurements can be used to measure the tectonic stresses. The prediction of depth-by-depth pore pressure can also reduce uncertainties associated with the assumption of constant pore pressure gradient in the stress profile analysis.

iii. Since hydraulic fractures propagate perpendicular to the least principal stress, it is very important to take into consideration the tectonic regime which defines the relationship between the vertical stress and the horizontal stresses. The stress

profile assessment should therefore depend on the type of faulting (i.e., normal, strike–slip or reverse) present in the region of interest.

iv. The overall completion quality rock classification proposed for the selection of candidate zones can be validated by analyzing production data.

5.3.2 Recommendations for the developed technique for mechanical damage characterization in proppant packs using acoustic measurements

i. Proppant diagenesis is a mechanism where under temperature and stress conditions, geochemical reactions occur between proppant pack and formation surface, which can accelerate mechanical damage in proppants. All the uniaxial experiments were conducted at room temperature, hence the effect of formation temperature conditions needs to be investigated in future studies.

ii. All the uniaxial experiments were also conducted on dry proppant packs. Future experiments should include the addition of water, or fracture fluids, to simulate geochemical interactions between proppants and the fluid. The experiments should also investigate the influence of the proppant-fluid interaction on the sensitivity acoustic measurements. These additional conditions simulate downhole conditions.

iii. The Hertz-Mindlin effective medium approximation applied in this study assumes identical, homogeneous, isotropic, and elastic spherical grains. Future experiments should include the use of proppants with varying characteristics such as the type, size, and sphericity of the proppants. This will enable the assessment of the effects

of these proppant characteristics on the coordination number and the fraction of grain contacts with friction parameters.

iv. The Hertz-Mindlin model also assumes homogenous strain. Granular dynamic numerical simulations of uniaxial compression of spherical packs can be carried out in future studies to investigate the homogenous strain assumption, and study the influence of stress relaxation in the contact area. The calibration parameters used in the numerical model can be cross-validated with the experimental data.

v. Proppant concentrations can also influence fracture conductivity. The tests designed in this study were carried out for only proppant concentration of 3 g/cm^2 (6 lb/ft^2). Hence, further studies can include sensitivity analysis on the proppant concentrations.

vi. The availability of more experimental data can be used to test the model proposed in this study. The additional data can also be used in generating a sensitivity chart with theoretical curves, which correlate the weight percentage of crushed proppants to the coordination and fraction of grain contacts with friction calibration parameters, in a single and more robust analytical model.

5.3.3 Recommendations for the study on the application of magnetic nanoparticles mixed with propping agents in enhancing near-wellbore fracture detection

i. The results of the experimental study can be cross validated through numerical simulation that models the propagation of superparamagnetic nanoparticles in a

hydraulic fracture, and the response of the propagation to a magnetic susceptibility system.

ii. The results of numerical simulation can be further used to obtain required volumes of nanoparticles, and the volumes used to predict the total cost for manufacture and application of nanoparticles as contrast agents for hydraulic fracture detection.

iii. The presence of steel casing, gravel-pack screens can result in interference of the magnetic susceptibility measurements, hence, this detection technique is currently recommended for open-hole completions. Future studies can investigate methods to correct for this interference, hence provide a wider application for the proposed detection technique.

REFERENCES

Anderson, D., and G. McNeil, 1992, Artificial neural networks technology: The data and analysis center for software technical report.

Agnew, B.G. 1966. Evaluation of Fracture Treatments with Temperature Surveys. *Journal of Petroleum Technology* **18** (7): 892-898.

Ali, H., Reed, S., Atekwana, E. and Atekwana, E. 2013. Magnetic Susceptibility is Associated with Oil-Bearing Intervals in an Oil Field, North Central Kansas. Society of Exploration Geophysicists.

Aranibar, A., Saneifar, M. and Heidari, Z. 2013. Petrophysical Rock Typing in Organic-Rich Source Rocks Using Well Logs. Paper SPE 168913 presented at the SPE Unconventional Resources Technology Conference, Denver, Colorado, USA, 12–14 August.

Avseth, P. and Bachrach, R. 2005. Seismic Properties of Unconsolidated Sands Tangential Stiffness, Vp/Vs Ratios and Diagenesis. Presented at the SEG Annual Meeting, Houston, Texas, 6–11 November.

Azike, O., Ajisafe, F., Pope, T., Burkhardt, C., Helmreich, A., and Phelps, M. 2014. 3D Structural Modeling and Property Characterization for Optimized Completion Design in the Wolfcamp Formation, Delaware Basin. Paper SPE 168990 presented at the SPE Unconventional Resources Conference, The Woodlands, Texas, USA, 1–3 April.

API RP 19C. 2008. Recommended Practices for Measurement of Properties of Proppants Used in Hydraulic Fracturing and Gravel-Packing Operations, Washington, DC: American Petroleum Institute.

API RP 56. 1983. Recommended Practices for Testing Sand Used in Hydraulic Fracturing Operations, Washington, DC: American Petroleum Institute.

Bachrach, R., Dvorkin, J., and Nur A.M. 2000. Seismic Velocities and Poisson's Ratio of Shallow Unconsolidated Sands. *Geophysics* **65** (2): 559-564.

Bachrach, R. and Avseth, P. 2008. Rock Physics Modeling of Unconsolidated Sands: Accounting for Nonuniform Contacts and Heterogeneous Stress Fields in the Effective Media Approximation with Applications to Hydrocarbon Exploration. *Geophysics* **73** (6): E197-E209.

Barron, A.R., Tour, J.M., Busnaina, A.A., Jung, Y.J., Somu, S., Kanj, M.Y., Potter, D., Resasco, D., and Ullo, J. 2010. Big Things in Small Packages. *Oilfield review*, vol. **22** (3): 38-49.

Barron, A.R., Skala, R.D., Coker, C.E., Chatterjee, D.K., and Xie, Y. 2012. Method of Manufacture and the Use of a Functional Proppant for Determination of Subterranean Fracture Geometries. US Patent US8168570 B2.

Bartington Instruments Ltd. 2010. Operation Manual for MS2 Magnetic Susceptibility System (OMO408 Issue 48). *Bartington Instruments Ltd*., http://www.bartington.com/Literaturepdf/Operation%20Manuals/om0408%20MS2.pdf (accessed 16 May 2014).

Bellarby, J. 2009. Developments in Petroleum Science, Volume 56 - Well Completion Design: Elsevier.

Berryman, J.G. 1995. Mixture Theories for Rock Properties. *AGU Reference Shelf* **3**: 205-228.

Biot, M.A. 1962. Mechanics of Deformation and Acoustic Propagation in Porous Media. *Journal of Applied Physics* **33** (4): 1482-1498.

Benz, M. 2012. Superparamagnetism: Theory and Applications- Discussion of Two Papers on Magnetic Nanoparticles.

Brannon, H.D. 2013. Apparatus and Methods for Providing Information About One or More Subterranean Variables. US Patent No. 8,797,037.

Cadwallader, S., Wampler, J., Sun, T., Sebastian, H., Graff, M., Gil, I., Patel, H., Merletti, G., Spain, D., Lowrey, T., Miller, R., Hadden, J., and Swanson, J. 2015. An Integrated Dataset Centered Around Distributed Fiber Optic Monitoring - Key to the Successful Implementation of a Geo-Engineered Completion Optimization Program in the Eagle Ford Shale. Paper SPE 178667 presented at the SPE Unconventional Resources Technology Conference, San Antonio, Texas, USA. 20–22 July.

Cheng, A. 1997. Material Coefficients of Anisotropic Poroelasticity. *International Journal of Rock Mechanics and Mining Sciences* **34:** 199-205.

Cheng, K., Aderibigbe, A., Alfi, M., Heidari, Z., and Killough, J. 2014. Quantifying the Impact of Petrophysical Properties on Spatial Distribution of Contrasting Nanoparticle Agents in the Near-Wellbore Region. *Petrophysics* **55** (5): 447-460.

Chi, S., Tang, X., and Zhu, Z. 2006. Inversion of Shear Wave Anisotropic Parameters in Strongly Anisotropic Formations. Massachusetts Institute of Technology. Earth Resources Laboratory.

Clavier, C., Coates, G., and Dumanoir, J. 1977. The Theoretical and Experimental Bases for the Dual Water Model for the Interpretation of Shaly Sands. Paper SPE 6859 presented at the SPE Annual Technical Conference and Exhibition, Denver, Colorado, USA, 9–12 October.

Crews, J.B., Huang, T., and Monteiro, O. 2010. Dual-Function Nano-Sized Particles. US Patent US20100314108 A1.

Dearing, J.A. 1994. Environmental Magnetic Susceptibility. Using the Bartington MS2 system. Kenilworth, Chi Publishers.

Deng, J.X., Han, D.H., and Wang, S.X. 2011. A Study of the Influence of Stress Relaxation on the Elastic Properties of Granular Materials and the Calibration of Effective Media Model. *Chinese Journal of Geophysics-Chinese Ed.* **54** (4): 1079-1089.

Dutta, T., Mavko, G., and Mukerji, T. 2010. Improved Granular Medium Model for Unconsolidated Sands Using Coordination Number, Porosity, and Pressure Relations. *Geophysics* **75** (2): E91-E99.

Eaton, B.A. 1969. Fracture Gradient Prediction and its Application to Oilfield Operations. *J. Petrol. Tech.,* October 1969, 1353-1360.

Expedition 340T Scientists. 2012. Atlantis Massif Oceanic Core Complex: Velocity, Porosity, and Impedance Contrasts within the Domal Core of Atlantis Massif: Faults and Hydration of Lithosphere during Core Complex Evolution. IODP Prel. Rept., 340T.

Fawad, M., Mondol, N.H., Jahren, J., and Bjorlykke, K. 2011. Mechanical Compaction and Ultrasonic Velocity of Sands with Different Texture and Mineralogical Composition. *Geophysical Prospecting* **59** (4): 697-720.

Fortin, J., Guéguen, Y., and Schubnel, A. 2007. Effects of Pore Collapse and Grain Crushing on Ultrasonic Velocities and Vp/Vs. *Journal of Geophysical Research* **112** (B8): B08207.

Friedrich, M. and Monson, G. 2013. Two Practical Methods to Determine Pore Pressure Regimes in the Spraberry and Wolfcamp Formations in the Midland Basin. Paper SPE 168834 presented at the SPE Unconventional Resources Technology Conference, Denver, Colorado, USA, 12–14 August.

Frydman, M., 2010. Determinations of the Dynamic Elastic Constants of a Transverse Isotropic Rock Based on Borehole Dipole Sonic Anisotopy in Deviated Wells. Rio Oil and Gas Expo and Conference, IBP2304_10.

Gadekea, L.L., Gartner, M.L., Sharbak, D.E., Sharbak, D.E., and Wyatt, D.F. 1991. The Interpretation of Radioactive-Tracer Logs Using Gamma-Ray Spectroscopy Measurements. *The Log Analyst* **32** (1): 24-34.

Gadeken, L.L. and Smith, H.D. 1986. Tracerscan- A Spectroscopy Technique for Determining the Distribution of Multiple Radioactive Tracers in Downhole Operations. Paper SPWLA-1986-ZZ presented at the 27th Annual SPWLA Logging Symposium, Houston, Texas, 9–13 June.

Gassmann, F., 1951, U¨ber die Elastizita¨t poro ¨ser Medien.Vier. der Natur. Gesellschaft Zu¨rich, **96**: 1-23.

Getty, J. and Bulau, C.R. 2014. Are the Laboratory Measurements of Proppant Crush Resistance Unrealistically Low? Paper SPE 68975 presented at the SPE Unconventional Resources Conference, The Woodlands, Texas, 1–3 April.

Golestanian, R., Liverpool, T. B., and Ajdari, A. 2007. Designing Phoretic Micro- and Nano-Swimmers. *New Journal of Physics* **9** (126): 2-8.

Gupta, N., Rai, C.S., and Sondergeld, C.H. 2012. Integrated Petrophysical Characterization of the Woodford Shale In Oklahoma. Paper SPWLA-2012-250 presented at the 53rd Annual SPWLA Logging Symposium, Cartagena, Colombia, 16–20 June.

Hallenburg, J.K. 1998. Non-Hydrocarbon Methods of Geophysical Formation Evaluation. Boca Raton, Fla: Lewis Publishers.

Hashin, Z. and Shtrikman, S. 1963. A Variational Approach to the Theory of the Elastic Behavior of Multiphase Materials. *J. Mech. Phys. Solids* **11**: 127-140.

Higgins, S.M., Goodwin, S.A., Donald, A., Bratton, T.R., and Tracy, G.W. 2008. Anisotropic Stress Models Improve Completion Design in The Baxter Shale. Paper SPE 115736 presented at the SPE Annual Technical Conference and Exhibition, Denver, Colorado, USA, 21–24 September.

Hill, R. 1952. The Elastic Behavior of Crystalline Aggregate. *Proceedings of the Physical Society* **65** (5): 349-354.

Hill, J.M. 1984. Sedimentation, Tectonism, and Hydrocarbon Generation in Delaware Basin, West Texas and Southeastern New Mexico. *AAPG Bulletin* **68**: 250-267.

Hood, A., Gutjahr, C., and Heacock, R. 1975. Organic Metamorphism and the Generation of Petroleum. *AAPG Bulletin* **59**: 989-996.

Horne, S., Primiero, P., Donald, A., Knight, E., Sayers, C., Koster, K., and Keir, D. 2010. Dipole Sonic Log Calibration Using Walkaway VSP data. SEG Technical Program Expanded Abstracts, 4334-4338.

Hrouda, F., Chlupaeova, M., Chadima, M. 2009. The Use of Magnetic Suscpetibility of Rocks in Geological Exploration (Case Histories Study).

Huh, C., Nizamidin, N., Pope, G.A., Milner, T.E., and Wang, B. 2014. Hydrophobic Paramagnetic Nanoparticles as Intelligent Crude Oil Tracers. US Patent WO2014123672 A1.

Jochen, V.A., Malpani, R., Moncada, K., Indriati, S., Altman, R.M., Luo, F., Xu, J. 2011. Production Data Analysis: Unraveling Reservoir Quality and Completion Quality. Paper SPE 147535 presented at the Canadian Unconventional Resources Conference, Calgary, Alberta, Canada, 15–17 November.

Kale, S., Rai, C.S., and Sondergeld, C.H. 2010. Rock Typing in Gas Shales. Paper SPE 134539 presented at the SPE Annual Technical Conference and Exhibition, Florence, Italy, 19–22 September.

King, G.E. 2010. Thirty Years of Gas Shale Fracturing: What Have We Learned? Paper SPE 133456 presented at the SPE Annual Technical Conference and Exhibition, Florence, Italy, 19–22 September.

Kurz, B.A., Schmidt, D.D., and Cortese, P.E. 2013. Investigation of Improved Conductivity and Proppant Applications in the Bakken Formation. Paper SPE 163849 presented at the SPE Hydraulic Fracturing Technology Conference, The Woodlands, Texas, 4–7 February.

Liang, F., Sayed, M., Al-Muntasheri, G. and Chang, F.F. 2015. Overview of Existing Proppant Technologies and Challenges. Paper SPE 172763 presented at the SPE Middle East Oil and Gas Show and Conference, Manama, Bahrain, 8–11 March.

MacQueen, J.B. 1967. Some Methods for Classification and Analysis of Multivariate Observations. Proceedings of the 5th Berkeley Symposium on Mathematical Statistics and Probability, Volume 1, 281-297.

Malik, M., Schmidt, C., Stockhausen, E.J., Vrubel, N.K., and Schwartz, K. 2013. Integrated Petrophysical Evaluation of Unconventional Reservoirs in the Delaware Basin. Paper SPE 166264 presented at the SPE Annual Technical Conference and Exhibition, New Orleans, Louisiana, USA, 30 September–2 October.

Mavko, G. and Bandyopadhyay, K. 2008. Approximate Fluid Substitution for Vertical Velocities in Weakly Anisotropic VTI Rocks. *Geophysics* **74**: D1-D6.

Mavko, G, Mukerji, T., and Dvorkin, J. 2009. The Rock Physics Handbook Tools for Seismic Analysis in Porous Media. New York: Cambridge University Press, p. 245-264.

McDaniel, R.R., Holmes, D.V., Borges, J., Bajoie, B.J., Peeples, C., and Gardner, R. 2009. Determining Propped Fracture Width from a New Tracer Technology. Paper SPE 119545 presented at the SPE Hydraulic Fracturing Technology Conference, The Woodlands, Texas, USA, 19–21 January.

Mindlin, R.D. 1949. Compliance of Elastic Bodies in Contact. *Journal of Applied Mechanics* **16**: 259-268.

Morrow, L., Potter, D.K., and Barron, A.R. 2015. Detection of Magnetic Nanoparticles against Proppant and Shale Reservoir Rocks. *Journal of Experimental Nanoscience* **10** (13): 1028-1041.

Montaut, A., Sayar, P., and Torres-Verdín, C. 2013. Detection and Quantification of Rock Physics Properties for Improved Hydraulic Fracturing in Hydrocarbon-Bearing Shale. Paper SPWLA-2013-KK presented at the 54th Annual SPWLA Logging Symposium, New Orleans, Louisiana, 22–26 June.

Murphy, W.F. 1982. Effects of Microstructure and Pore Fluids on the Acoustic Properties of Granular Sedimentary Materials: Ph.D. Dissertation, Stanford University, USA (June 1982).

Murphy, E., Barraza, S. R., Gu, M., Gokaraju, D., Far, M. E., and Quirein, J. 2015. New Models for Acoustic Anisotropic Interpretation in Shale. Paper SPWLA-2015-WWWW presented at the 56th Annual SPWLA Logging Symposium, Long Beach, California, USA, 18–22 July.

Norris, A.N., and Johnson, D.L. 1997. Non-linear Elasticity of Granular Media. *Journal of Applied Mechanics* **64**: 39-49.

Nye, J.F. 1985. Physical Properties of Crystals: Oxford Univ. Press, New York. p. 322.

Palisch, T.T., Duenckel, R., Chapman, M.A. 2010. How to Use and Misuse Proppant Crush Tests: Exposing the Top 10 Myths. Paper SPE 119242 presented at the SPE Hydraulic Fracturing Technology Conference, The Woodlands, Texas, 19–21 January.

Passey, Q.R., Creaney, S., Kulla, J.B., Moretti, F.J., and Stroud, J.D. 1990. A Practical Model for Organic Richness from Porosity and Resistivity Logs. *AAPG Bulletin* **74** (12): 1777-1794.

Passey, Q.R., Bohacs, K., Esch, W. L., Klimentidis, R., and Sinha, S. 2010. From Oil-Prone Source Rock to Gas-Producing Shale Reservoir- Geologic and Petrophysical Characterization of Unconventional Shale Gas Reservoirs. Paper SPE 131350 presented at the SPE International Oil and Gas Conference and Exhibition, Beijing, China, 8–10 June.

Pistre, V., Kinoshita, T., Endo, T., Schilling, K., and Pabon, J. 2005. A Modular Wireline Sonic Tool for Measurements of 3D (Azimuthal, Radial, and Axial Formation Acoustic) Properties. Paper SPWLA-2005-P presented at the 46th Annual SPWLA Logging Symposium, New Orleans, Louisiana, 26–29 June.

Podio, A.L., Gregory, A.R., and Gray, K.E. 1968. Dynamic Properties of Dry and Water Saturated Green River Shale Under Stress: *Soc. Pet. Eng. J.* **8**: pp. 389-404.

Popielski, A.C., Heidari, Z., and Torres-Verdin, C. 2012. Rock Classification from Conventional Well Logs in Hydrocarbon-Bearing Shale. Paper SPE 159255 presented at the SPE Annual Technical Conference and Exhibition, San Antonio, Texas, USA, 8–10 October.

Potter, D.K. 2007. Magnetic Susceptibility as a Rapid, Nondestructive Technique for Improved Petrophysical Parameter Prediction. *Petrophysics* **43** (3): 191-201.

Potter, D.K., Al-Ghamdi, T.M., and Ivakhnenko, O.P. 2011. Sensitive Carbonate Reservoir Rock Characterization from Magnetic Hysteresis Curves and Correlation with Petrophysical Properties. *Petrophysics* **52** (1): 50-57.

Potter, D.K., Barron, A.R., Maguire-Boyle, S.J., Orbaek, A.W., Ali, A., Harrison, L. 2011. Magnetic Particles for Determining Reservoir Parameters. US Patent WO2011153339 A1.

Quirein, J., Witkowsky, J, Truax, J.A., Galford, J. E., Spain, D. R., and Odumosu, T. 2010. Integrating Core Data and Wireline Geochemical Data for Formation Evaluation and Characterization of Shale Gas Reservoirs. Paper SPE 134559 presented at the SPE Annual Technical Conference and Exhibition, Florence, Italy, 19–22 September.

Quirein, J., Eid, M., and Cheng, A. 2014. Predicting the Stiffness Tensor of a Transversely Isotropic Medium When the Vertical Poisson's Ratio is Less Than the Horrizontal Poisson's Ratio. Paper SPWLA-2014-OOOO presented at the 56th Annual SPWLA Logging Symposium, Abu Dhabi, United Arab Emirates, 18–22 May.

Rae, P., and Di Lullo, G. 1996. Fracturing Fluids and Breaker Systems- A Review of the State-of-the-Art. Paper SPE 37359 presented at the SPE Eastern Regional Meeting, Columbus, Ohio, 23–25 October.

Rafatian, N. and Caspan, J. 2015. Petrophysical Characterization of the Pore Space in Permian Wolfcamp Rocks. *Petrophysics* **56** (1): 45-57.

Rahmani, A.R., Bryant, S., Huh, C., Athey, A., Ahmadian, M., Chen, J., and Wilt, M. 2013. Crosswell Magnetic Sensing of Superparamagnetic Nanoparticles for Subsurface Applications. Paper SPE 166140 presented at the SPE Annual Technical Conference and Exhibition, New Orleans, Louisiana, USA, 30 September–2 October.

Raysoni, N. and Weaver, J.D. 2012. Long-Term Hydrothermal Proppant Performance. Paper SPE 150669 presented at the SPE International Symposium and Exhibition on Formation Damage Control, Lafayette, Louisiana, 15–17 February.

Rebelle, M. and Lalanne, B. 2014. Rock Typing in Carbonates: A Critcal Review of Clustering Methods. Paper SPE 171759 presented at the Abu Dhabi International Petroleum Exhibition and Conference, Abu Dhabi, UAE, 10–13 November.

Robinson, S., Mrozewski, S., Hussein, T., Masterson, W., Meissner, E., Williams, T., Keogh, W., Myers, G., Bartington, G., and Goldberg, D. 2008. A New Borehole Magnetic Susceptibility Tool for High Resolution Formation Evaluation. Paper SPWLA-2008-JJJ presented at the 49th Annual SPWLA Logging Symposium, Edinburgh, Scotland, 25–28 May.

Saldungaray, P.M., Palisch, T.T., and Duenckel, R. 2012. Novel Traceable Proppant Enables Propped Frac Height Measurement While Reducing the Environmental Impact. Paper SPE 151696 presented at the SPE/EAGE European Unconventional Resources Conference and Exhibition, Vienna, Austria, 20–22 March.

Saneifar, M., Aranibar, A., and Heidari, Z. 2014. Rock Classification in the Haynesville Shale Based on Petrophysical and Elastic Properties Estimated from Well Logs. *Interpretation* **3**: SA65-SA75.

Saul, M., Lumley, D., and Shragge, J. 2013. Modeling the Pressure Sensitivity of Uncemented Sediments using a Modified Grain Contact Theory: Incorporating Grain Relaxation and Porosity Effects. *Geophysics* **78** (5): D327-D338.

Savage, W.Z., Swolfs, H.S. and Amadei, B. 1992. On the State of Stress in the Near-Surface of the Earth's Crust. *Pure and Applied Geophysics* **138**: 207-228.

Sayers, C.M. 1994. The Elastic Anisotropy of Shales. *Journal of Geophysical Research* **99** (B1): 767-774.

Sayers, C.M. 2005. Seismic Anisotropy of Shales. *Geophysical Prospecting* **53**: 667-676.

Sayers, C.M. 2013. The Effect of Kerogen on the Elastic Anisotropy of Organic-rich Shales. *Geophysics* **78**: D65-D74.

Schoenberg, M., Muir, F., and Sayers, C. 1996. Introducing ANNIE: A Simple Three Parameter Anisotropic Velocity Model for Shales. *Journal of Seismic Exploration* **5**: 35-49.

Schmidt, H.K. and Tour, J.M. 2012. Methods for Magnetic Imaging of Geological Structures. US Patent US8269501 B2.

Sebastian, H., Gil, I., Graff, M., Wampler, J., Merletti, G., Sun, T., Cadwallader, S., Patel, H., Spain, D., Cawiezel, K., Smith, P. and Keck, R. 2015. 3-D Hydraulic Fracturing and Reservoir Flow Modeling - Key to the Successful Implementation of a Geo-Engineered Completion Optimization Program in the Eagle Ford Shale. Paper SPE 178512 presented at the Unconventional Resources Technology Conference, San Antonio, Texas, USA, 20–22 July.

Simo, H., Pournik, M., and Sondergeld, C. 2013. Proppant Crush Test: A New Approach. Paper SPE 164506 presented at the SPE Production and Operations Symposium, Oklahoma, Texas, 26–23 March.

Slocombe, R., Acock, A., Chadwick, C., Wigger, E., Viswanathan, A., Fisher, K., and Reischman, R. 2013. Eagle Ford Completion Optimization Using Horizontal Logging Data. Paper SPE 168693 presented at the SPE Unconventional Resources Technology Conference, Denver, Colorado, USA, 12–14 August.

Sone, H. 2012. Mechanical Properties of Shale Gas and Its Relation to the In-Situ Stress Variation Observed in Shale Gas Reservoirs. Ph.D. Thesis, Stanford University, USA (March 2012).

Stephens, W.T., Schubarth, S.K., Rivera, D.I., Snyder, E.M., and Herndon, D.C. 2006. Statistical Study of the Crush Resistance Measurement for Ceramic Proppants. Paper SPE 102645 presented at the SPE Annual Technical Conference and Exhibition, San Antonio, Texas, 24–27 September.

Stigler, S.M. 1981. Gauss and the Invention of Least Squares. *The Annals of Statistics* **9** (3): 465-474.

Suarez-Rivera, R. and Bratton, T. 2009. Estimating Horizontal Stress from Three-Dimensional Anisotropy. US Patent application number 20090210160.

Sun, T., Merletti, G., Patel, H., Cadwallader, S., Graff, M., Wampler, J., Gil, I., Sebastian, H., and Spain, D. 2015. Advanced Petrophysical, Geological, Geophysical and Geomechanical Reservoir Characterization – Key to the Successful Implementation of a Geo-Engineered Completion Optimization Program in the Eagle Ford Shale. Paper SPE 178524 presented at the SPE Unconventional Resources Technology Conference, San Antonio, Texas, USA, 20–22 July.

Tang, X.M., Reiter, E.C., and Burns, D.R. 1995. A Dispersive-Wave Processing Technique for Estimating Formation Shear Velocity from Dipole Stoneley Waveforms. *Geophysics* **60** (1): 19-28.

Tissot, B.P. and Welte, D.H. 1978. Petroleum Formation and Occurrence: Springer-Verlag. Berlin. p. 538.

Thiercelin, M. J. and Plumb, R.A. 1994. Core-Based Prediction of Lithologic Stress Contrasts in East Texas Formations. *SPE Formation Evaluation* **9**: 251-258.

Thomsen, L., 1986, Weak Elastic Anisotropy. *Geophysics* **51**, 1954-1966.

Tsvankin, I. 2005. Seismic Signatures and Analysis of Reflection Data in Anisotropic Media, Second edition: Elsevier science.

Vernik, L. and Liu, X. 1997. Velocity Anisotropy in Shales. A Petrophysical Study. *Geophysics* **62**: 521-532.

Wahajuddin and Arora S. 2012. Superparamagnetic Iron Oxide Nanoparticles: Magnetic Nanoplatforms as Drug Carriers. *International Journal of Nanomedicine* **7**: 3445-3471.

Walsh, J., Sinha, B., and Donald, A. 2006. Formation Anisotropy Parameters Using Borehole Sonic Data. Paper SPWLA-2006-TT presented at the 47th Annual SPWLA Logging Symposium, Veracruz, Mexico, 4–7 June.

Walpole, L.J. 1966. On Bounds for the Overall Elastic Moduli of Inhomogeneous Systems —I. *Journal of the Mechanics and Physics of Solids* **14** (3): 151-162.

Ward, J.H. 1963. Hierarchical Grouping to Optimize an Objective Function. *Journal of the American Statistical Association* **58** (301): 236-244.

Warpinski, N.R. and Smith, M.B. 1989. Rock Mechanics and Fracture Geometry, *in* Gidley, J.L., Holditch, S.A., Nierode, D.E., and Veatch, R.W. Jr., (eds.), Recent Advances in Hydraulic Fracturing: *SPE Monograph* **12**: 57–80.

Wigger, E., Viswanathan, A., Fisher, K., Slocombe, R.W., Kaufman, P., and Chadwick, C. 2014. Logging Solutions for Completion Optimization in Unconventional Resource Plays. Paper SPE 167726 presented at the SPE/EAGE European Unconventional Resources Conference and Exhibition, Vienna, Austria, 25–27 February.

Winkler, K.W. 1983. Contact Stiffness in Granular Porous Materials: Comparison between Theory and Experiment. *Geophysical Research Letters* **10** (11): 1073-1076.

Wood, A.W. 1955. A Textbook of Sound: Being an Account of the Physics of Vibrations with Special Reference to Recent Theoretical and Technical Developments: London: Bell, pp. 360.

Wright, C.A., Davis, E.J., Weijers, L., Golich, G.M., Ward, J.F., Demetrius, S.L., and Minner, W.A. 1998. Downhole Tiltmeter Fracture Mapping: A New Tool for Directly Measuring Hydraulic Fracture Dimensions. Paper SPE 49193 presented at the SPE Annual Technical Conference and Exhibition, New Orleans, Louisiana, USA, 27–30 September.

Wyllie, M.R.J., Gregory, A.R., and Gardner, G.H.F., 1958, An Experimental Investigation of Factors Affecting Elastic Wave Velocities in Porous Media. *Geophysics* **23** (2):459-493.

Yu, H., Kotsmar, C., Yoon, K.Y., Ingram, D.R., Johnston, K.P., Bryant, S.L., and Huh, C. 2010. Transport and Retention of Aqueous Dispersions of Paramagnetic Nanoparticles in Reservoir Rocks. Paper SPE 129887 presented at the SPE Improved Oil Recovery Symposium, Tulsa, Oklahoma, USA, 24–28 April.

Yu, J., Berlin, J.M., Lu, W., Zhang, L., Kan, A.T., Zhang, P., Wash, E.E., Work, S., Chen, W. Tour, J, Wong, M., and Tomson, M.B. 2010. Transport Study of Nanoparticles for Oilfield Application. Paper SPE 131158 presented at the SPE International Conference on Oilfield Scale, Aberdeen, United Kingdom, 26–27 May.

Zimmer, M.A. 2003. Seismic Velocities in Unconsolidated Sands: Measurements of Pressure, Sorting, and Compaction Effects. Ph.D. Dissertation, Stanford University, USA (November 2003).

APPENDIX A

LIST OF PUBLICATIONS

The following sections documents the conference and journal papers that the researched described in this dissertation have been published or submitted for peer review.

A.1 Refereed Journal Publications

Aderibigbe A., Cheng, K., Heidari, Z., Killough, J., Fuss, T., and Stephens, W. 2016. Application of magnetic nanoparticles mixed with propping agents in enhancing near-wellbore fracture detection. *Journal of Petroleum Science and Engineering* **141**, 133-143.

Aderibigbe, A. A., Valdes, C. C., and Heidari, Z. 2016. Integrated Rock Classification in the Wolfcamp Formation based on Reservoir Quality and Anisotropic Stress Profile Estimated from Well Logs. Accepted for publication in *SEG Interpretation Journal* **4** (2).

Aderibigbe, A. A., Valdes, C. C., Heidari, Z., and Fuss, T. 2014. Mechanical Damage Characterization in Proppant Packs Using Acoustic Measurements. Paper IPTC-18092-MS submitted for review in *SPE Productions and Operations Journal*.

Cheng, K., Aderibigbe, A., Alfi, M., Heidari, Z., and Killough, J. 2014. Quantifying the Impact of Petrophysical Properties on Spatial Distribution of Contrasting Nanoparticle Agents in the Near-Wellbore Region, *Petrophysics*, vol. **55** (5), 447-460.

Valdes, C. C., Aderibigbe, A. A., and Heidari, Z. 2015. Impact of Anisotropic Elastic and Petrophysical Properties on Stress Prediction in Organic-rich Mudrocks. Paper 2015-FFF submitted for review in *SEG Interpretation Journal*.

A.2 Refereed Conference Proceedings

Aderibigbe, A., Amin, S., Wehner, M., Conte, R., Zeng, Z., Xu, G., Maulana, I., Heidari, Z., Tice, M. and Laya, J. C. 2015. Rock Classification in the Eagle Ford Shale Formation Using Well Logs and Geological Evaluation. Presented at the AAPG/SEG International Conference and Exhibition, Melbourne, Australia, 13–16 September.

Valdes, C. C., Aderibigbe, A. A., and Heidari, Z. 2015. Impact of Anisotropic Elastic and Petrophysical Properties on Stress Prediction in Organic-rich Mudrocks. Paper prepared for presentation at the SPWLA 56th Annual Logging Symposium, Long Beach, California, USA, 18–22 July.

Aderibigbe, A. A., Valdes, C. C., Heidari, Z., and Fuss, T. 2014. Mechanical Damage Characterization in Proppant Packs Using Acoustic Measurements. Paper IPTC 18092 presented at the International Petroleum Technology Conference, Kuala Lumpur, Malaysia, 10–12 December.

Aderibigbe, A., Cheng, K., Heidari, Z., Killough, J., Fuss, T., and Stephens, W. 2014. Detection of Propping Agents in Fractures using Magnetic Susceptibility Measurements Enhanced by Magnetic Nanoparticles. Paper SPE 170818 presented at the SPE Annual Technical Conference and Exhibition, Amsterdam, The Netherlands, 27–29 October.

Cheng, K., Aderibigbe, A., Alfi, M., Heidari, Z., and Killough, J. 2014. Quantifying the Impact of Petrophysical Properties on Spatial Distribution of Contrasting Nanoparticle Agents in the Near-Wellbore Region. Paper B presented at the SPWLA 55th Annual Symposium, Abu Dhabi, UAE, 18–22 May. (Best Poster Award).